# OBSERVATIONS OF STOCHASTIC ION HEATING

# BY LOW FREQUENCY DRIFT WAVES

Thesis by

Jon Mearns McChesney

In Partial Fulfillment of the Requirements

for the Degree of

Doctor of Philosophy

California Institute of Technology

1989

(Submitted September 27, 1988)

## ACKNOWLEDGEMENTS

# ABSTRACT

Several laser induced fluorescence (LIF) experiments were performed on the Encore tokamak device. These experiments represent the first application of this technique to the majority ions of a tokamak. The main laser system selected consisted of a copper vapor laser (CVL), which pumped a narrowband, tunable dye laser. This system allowed the Doppler-broadened, ion distribution function to be scanned with high resolution, giving accurate ion temperature measurements. As a preliminary test, the diagnostic was used to observe ion heating in the presence of lower hybrid RF power. Ion temperatures were found to increase dramatically with increasing RF power.

By using a second dye laser, actual ion trajectories were determined using the technique of "optical tagging." Tagging involves the use of a so-called "pump" laser to alter the fraction of ions in a particular quantum state. As a preliminary test, this technique was used to demonstrate ion gyro-motion in Encore.

Using the ion distribution functions determined by means of LIF, it was possible to make detailed measurements of ion heating during an ohmically heated tokamak discharge. It was found that the observed rate of ion heating was nearly two orders of magnitude faster than expected from collisional energy exchange with the hot electrons. The high ion temperatures inferred from the LIF measurements were later verified by measuring the Landau damping of ion acoustic waves. The observed damping lengths were roughly in accord with those calculated using measured values of $T_e$ and $T_i$.

This enhanced ion heating was correlated with the presence of large amplitude, low frequency ($\omega < \omega_{ci}$), drift-Alfvén waves. Using numerical calculations, it was

shown that in the presence of electrostatic modes (such as drift waves) of sufficient amplitude, ion motion becomes stochastic or chaotic. In physical terms, stochasticity occurs when the ion displacement that is due to the polarization drift becomes comparable to the perpendicular wavelength, i.e., when $\alpha = m_i k_\perp^2 \phi_0 / q B_0^2 \sim 1$. A combination of numerical calculations and experiments was used to demonstrate that stochasticity was indeed responsible for the observed rapid heating.

Finally, we concluded by speculating that stochastic heating may also be the cause of the anomalously high ion temperatures observed in reversed field pinches (RFP's) and in field reversed configurations (FRC's). Intrinsic stochasticity is also important in the field of auxiliary plasma heating. As is now well known, a large amplitude RF electric field can heat particles despite a large mismatch between the wave frequency and the gyrofrequency.

v

# TABLE OF CONTENTS

# FIGURES

# TABLES

# CHAPTER ONE

# INTRODUCTION

This thesis describes the first application of laser induced fluorescence (LIF) techniques to the majority ions of a tokamak. The application of LIF or resonance fluorescence to plasma ions was first proposed by Measures (1968) and Dimock et al. (1969). The technique was first successfully applied to plasmas by Stern and Johnson (1975) and Stern et al. (1976). These workers used LIF to obtain ion velocity distribution functions in argon plasmas. The technique has previously been applied to tokamak plasmas; however, in those experiments the majority hydrogen or deuterium ions were fully stripped and only hydrogen neutrals (e.g., Burakov et al., 1977) or impurity ions (e.g., Muller and Burrell, 1981) could be studied. The present series of experiments were performed in the Encore high repetition tokamak, which produced hydrogen or noble gas plasmas. Spectroscopic studies revealed that the argon plasmas produced in Encore were chiefly singly ionized (Ar II). This was fortunate since several convenient LIF schemes are possible in Ar II plasmas. Using a tunable narrowband laser, we used LIF to trace out the ion velocity distributions in Ar II plasmas. These measurements showed that ion heating in Encore was anomalously fast, i.e., much faster than expected classically through collisional energy exchange with the hot electrons. This anomalous heating was correlated with the presence of low frequency, coherent, electrostatic modes. The present work describes theoretically and verifies experimentally that in the presence of these modes, ion motion becomes stochastic or chaotic, resulting in bulk ion heating.

The apparatus is discussed in Chap. 2. All our experiments were performed in the Encore high repetition rate tokamak (Fredrickson and Bellan, 1985). A new chamber section was designed to permit the fullest possible access to the plasma. Two different laser systems were used. The principal laser system consisted of a narrow-band dye laser pumped by a copper vapor laser (CVL). The second laser was a high power, flashlamp-pumped, dye laser. The first laser was used primarily for scanning Doppler-broadened, ion distribution functions, while the second laser was used in conjunction with the first to perform optical tagging (OT) experiments. OT is a relatively new technique that allows direct measurements of ion transport by altering the fraction of ions in a particular quantum state.

The application of LIF to plasmas is discussed in Chap. 3. A survey of the possible line-broadening mechanisms is presented, and it is shown that Doppler broadening is the dominant line-broadening mechanism occurring in Encore. All other broadening mechanisms are either negligible or can be easily corrected for. By scanning the Doppler-broadened line shape, it was possible to obtain the ion velocity distribution function and hence the ion temperature. Various fluorescence schemes are possible in singly-ionized argon, and several of these are presented. The technique is demonstrated by showing that strong ion heating takes place when lower hybrid RF power is applied. The LIF technique of optical tagging is then discussed. The use of optical tagging is demonstrated by a simple experiment, in which the direction of gyro-rotation was reversed when the toroidal magnetic field was reversed. Finally, data showing anomalously fast ion heating are presented. Using the LIF technique it was possible to study ion heating during an ohmically heated tokamak discharge. In particular, it was possible to observe heating during

the first few hundred microseconds of the discharge. These initial experiments showed rates of ion heating nearly two orders of magnitude faster than expected from the classical heating mechanism (collisional exchange of energy with the hot electrons).

The anomalous ion heating in Encore was found to be due to stochastic ion heating in the presence of large amplitude, low frequency ($\omega < \omega_{ci}$) drift-Alfvén waves. A brief description of these modes is given in Chap. 4. A derivation of the drift-Alfvén dispersion relation is left to Appendix B. Using a slab model of the drift modes, the conditions necessary for stochastic ion behavior were determined numerically. It was shown that stochastic heating is possible when the drift wave amplitude exceeds a threshold value given by $\phi_0 = qB_0^2/m_i k_\perp^2$. This condition corresponds to the breakdown of the guiding center approximation and occurs when the ion displacement that is due to the polarization drift becomes comparable to the wavelength of the mode. When the ion motion becomes stochastic, energy may be exchanged irreversibly with the wave and true heating takes place. It is noted that since ion motion is non-adiabatic for stochastically heated ions, they can attain kinetic energies far in excess of their maximum potential energies in the drift wave potential trough. Finally, it was shown that stochastic heating by low frequency modes ($\omega < \omega_{ci}$) can be described physically in terms of a trapping/detrapping process.

In Chap. 5, experimental data confirming the results of Chap. 4 are presented. Firstly it was shown that the highest ion heating rate occurs in the region of the plasma where the drift mode amplitude was highest, namely at the plasma edge. Next, it was demonstrated that the peak ion temperature during a discharge dis-

played a threshold with increasing mode amplitude. It was possible to control the mode amplitude by gradually increasing the plasma current since the drift-Alfvén modes were current-driven. As is well known, ion acoustic waves are strongly Landau damped when $T_e/T_i < 10$. This fact suggested measuring damping lengths as a function of wave amplitude. As the wave amplitude increased, $T_i$ would rise rapidly and cause strong wave damping. A heterodyne detection system was set up to trace out the damped waveforms. When the ion heating was strong, the acoustic waves were indeed strongly damped, and damping lengths were in rough accord with those calculated from measured values of $T_i$ and $T_e$. Langmuir probe and fluorescence techniques were used to demonstrate that irreversible exchanges of energy occurred between ions and the mode. Finally, a simple numerical calculation of the ion heating was performed and the results were compared with actual experimental heating results. The model used in the numerical calculations was based on experimentally measured values of the mode amplitude, mode structure and magnetic field, and gave good agreement with the experimentally observed heating rates and final ion temperatures. The model calculations traced the trajectories of large numbers of ions and gave the ion distribution function. From these orbit calculations, the quantitative differences between stochastic and non-stochastic motion were apparent.

The results of the present work are summarized, and several conclusions and speculations are presented in the final chapter. One particularly interesting speculation was that a similar mechanism seems to apply to ion heating in reversed field pinches (RFP's) and field reversed configuration devices (FRC's). These devices provide a promising alternative to tokamaks because they use a much smaller toroidal magnetic field. The small toroidal field allows them to operate at much

higher values of $\beta$ (the ratio of plasma pressure to magnetic pressure) than tokamaks. Spectroscopic and charge exchange analyses of RFP's have shown ion temperatures in excess of the electron temperature and rates of ion heating far exceeding those predicted by ohmic heating (Howell and Nagayama, 1985). It is shown in this chapter that plasma conditions in RFP's are similar to those in Encore. In particular, several important dimensionless ratios are identical, leading us to predict that drift waves of some type are present in RFP's and that they are responsible for the fast rates of heating observed in these devices.

Appendix A describes the construction of unstable resonator optics necessary for the efficient pumping of the dye laser by the copper vapor laser. Appendix B contains a derivation of the drift-Alfvén dispersion relation. Appendix C describes the heterodyne detection system used to study the Landau damping of ion acoustic waves.

# CHAPTER TWO

# APPARATUS

## 2.1 ENCORE TOKAMAK

The laser induced measurements made in the present work were performed on the Caltech Encore tokamak device. The principles of tokamak operation have been described in detail elsewhere and will not be discussed here. Artsimovich (1972) gives a straightforward, physical description of tokamak fundamentals. Another more recent review is given by Furth (1981). Several features make Encore attractive for fluorescence work. In particular, it is typically operated using noble gas discharges, allowing fluorescence experiments to be performed on noble gas ions. In addition, Encore is a high repetition rate device (typically 15 shots per second) allowing signal averaging techniques to be employed. This high repetition rate is obtained by using a DC toroidal field and a high power, audio-frequency amplifier to drive the ohmic heating transformer. This high repetition rate is achieved at the expense of the plasma parameters. In Table 2.1, Encore's parameters are compared with those of the TEXT machine (University of Texas at Austin) and TFTR (Princeton Plasma Physics Laboratory). The TEXT device is a medium sized tokamak, while TFTR is a fusion test reactor. The plasma densities and temperatures found in these two machines clearly exceed those in Encore by several orders of magnitude, but the same basic magnetic field configuration and principles of operation apply to all three devices. Figure 2.1 is a photograph of Encore showing the special ports used in the LIF work. Figure 2.2 shows typical loop voltage and plasma current traces. Because of the large spacing between the toroidal field

| DEVICE | R(cm) | a(cm) | $B_t$(kG) | I(kA) | $n$(cm$^{-3}$) | $T_i$(eV) | $T_e$(eV) | DURATION(ms) |
|--------|-------|-------|-----------|-------|----------------|-----------|-----------|--------------|
| TFTR   | 2500  | 85    | 52        | 2500  | $10^{14}$      | $10^4$    | $10^4$    | 1000         |
| TEXT   | 100   | 27    | 10        | 100   | $10^{13}$      | 600       | 600       | 500          |
| ENCORE | 38.1  | 12.6  | 1         | 5     | $10^{12}$      | 5         | 15        | 3            |

TABLE 2.1  Comparison of device parameters for three different tokamaks.
R is the major radius, a the minor radius and $B_t$ the toroidal magnetic
field strength.
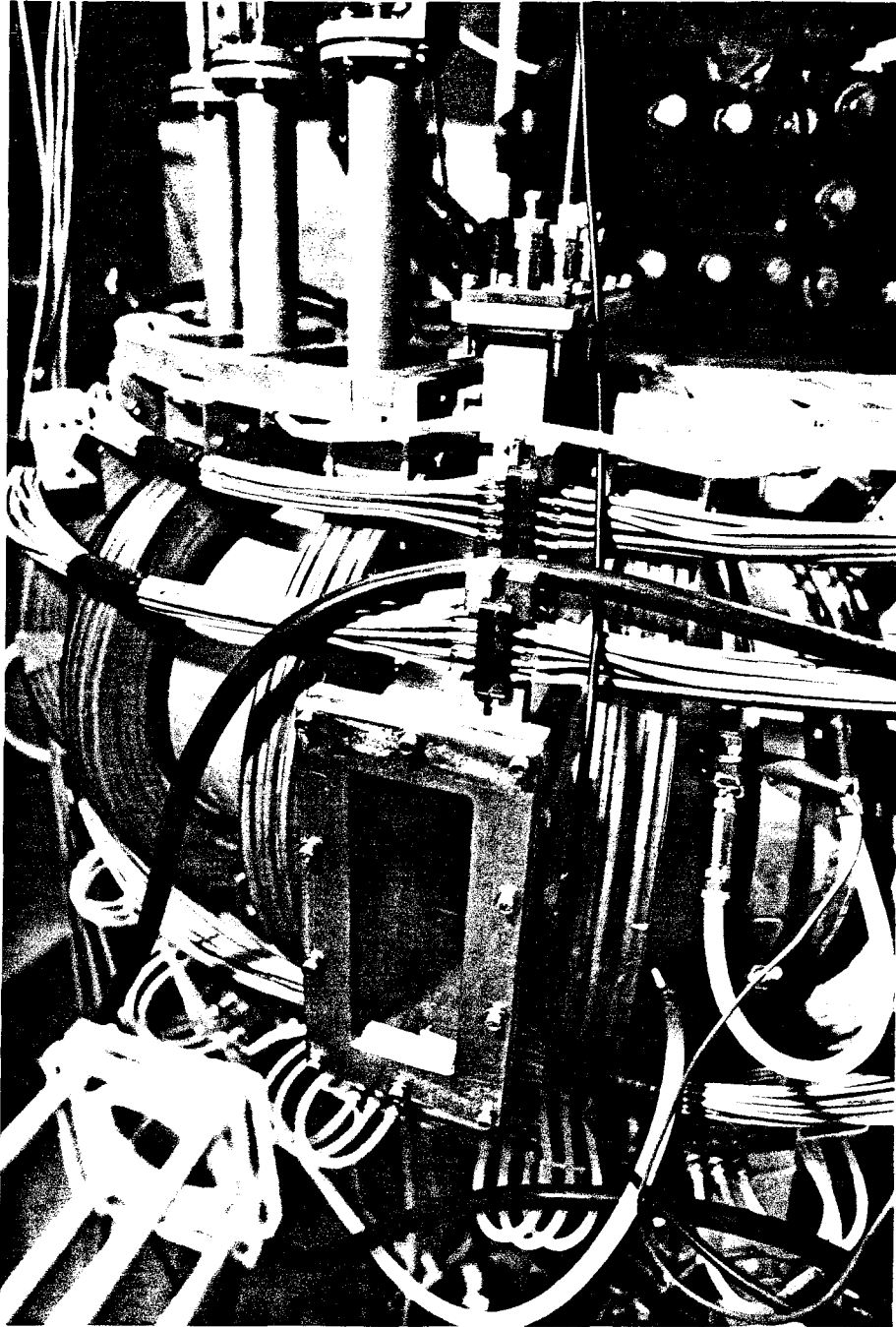
FIG. 2.1  Encore tokamak showing the ports designed for the LIF experiments.

Channel 1
.5 ms  .5 V

Channel 2
.5 ms  1 V
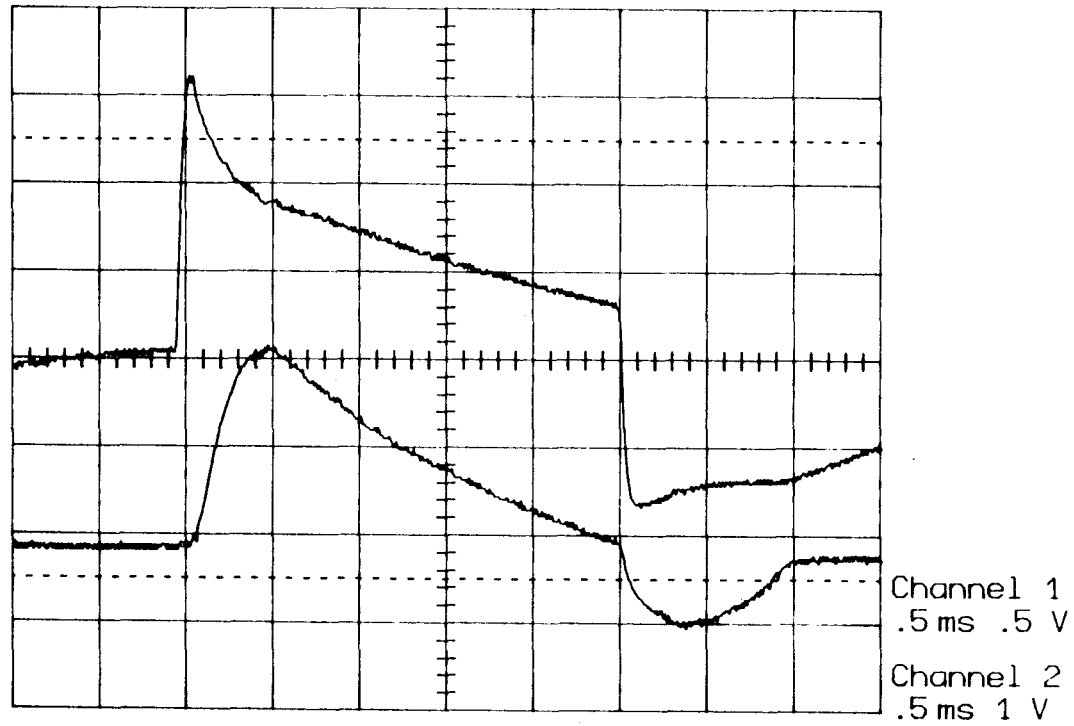
FIG. 2.2  Oscilloscope traces of loop voltage (top) and plasma current (bottom). The horizontal scale is 0.5ms/div. The vertical scales are 5V/div for the loop voltage and 1kA/div for the plasma current.

coils (see Fig. 2.1), there was excellent access to the plasma. Depending on the exact configuration of the torus, there were up to 33 small (4cm diameter) and 15 large (8×22cm) ports. In addition, a specially constructed chamber section permitted virtually the entire poloidal cross section to be interrogated. See Fig. 2.3 for details. The plasma minor radius is 12.6cm and the major radius is 38.1cm, resulting in an aspect ratio of about three. The 1.27cm thick aluminum chamber walls provided some lateral stabilization of the plasma. Additional stabilization was provided by a vertical field, which made up for the flux lost in the resistive decay of the wall currents. The vertical field could be either DC or pulsed, the pulsed field being preferred when large field strengths were required.

The principal cause of energy loss in Encore is probably line radiation from neutral or partially ionized particles. Assuming a plasma current of 1kA and a loop voltage of 10V, the input ohmic heating power is 10kW. For such a discharge; $T_e \sim 12eV$, $T_i \sim 2eV$ and $n \sim 10^{12}cm^{-3}$. Summers and McWhirter (1979), give tables of radiation power-loss coefficients for several elements, including argon. In Chap. 3 it will be shown that the dominant charge state in Encore is ArII (singly ionized). According to Summers and McWhirter (1979) the power-loss coefficient for ArII is $7.3 \times 10^{-26} Wcm^3$. If the plasma is assumed to be in coronal equilibrium, then the total power-loss coefficient from all the ionization states is $3.9 \times 10^{-26} Wcm^3$. Assuming a plasma volume of $1.2 \times 10^5 cm^{-3}$ these two coefficients give power losses of 8.8kW and 4.7kW respectively. Energy loss because of poor particle confinement is evidently also important. If a low particle confinement time of $100\mu s$ is assumed, then the resulting energy loss rate is 2.3kW. Another and equally important loss mechanism involves the energy expended in ionizing neutral argon. The first ion-
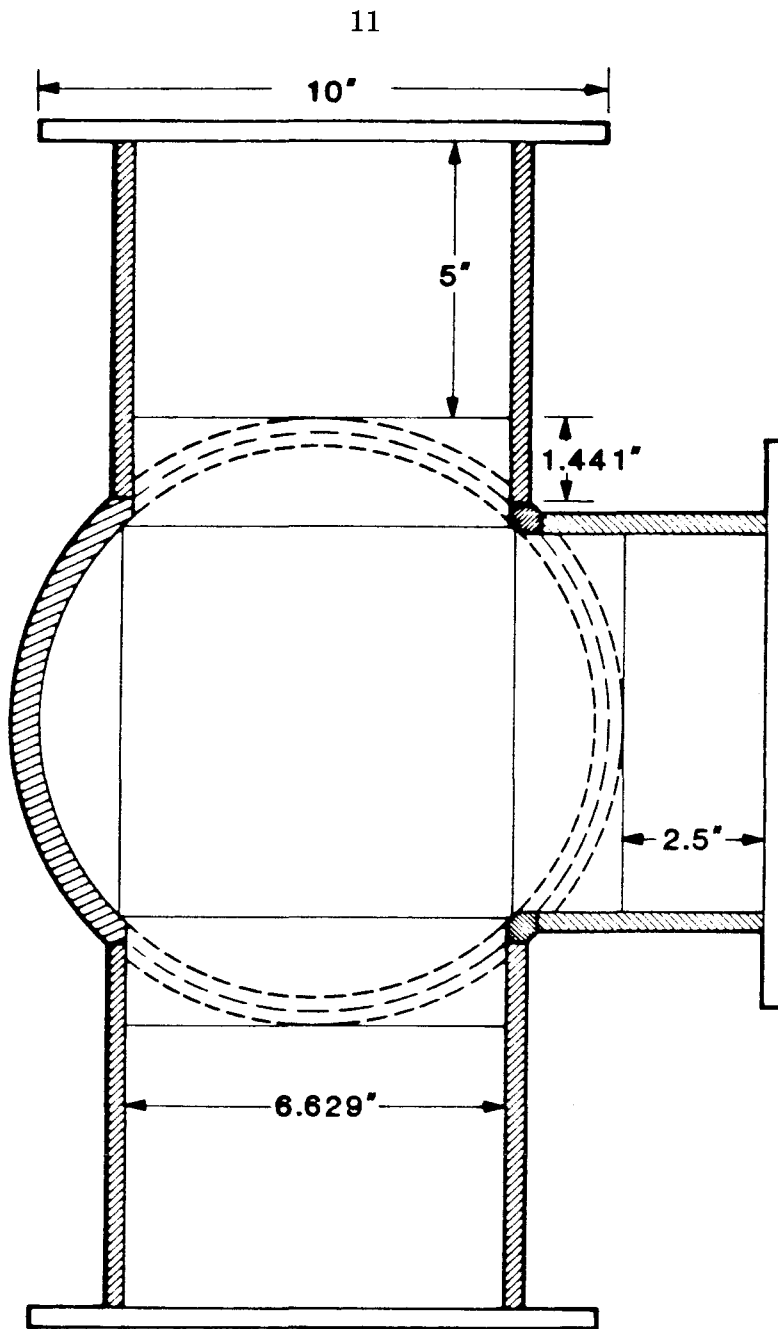
FIG. 2.3  Detail of the special chamber section used for the LIF experiments. The available viewing area was 6.63 x 6.63 sq. in.

ization energy of argon is 15.8eV, therefore each time an ion-electron pair is lost, 15.8eV must be expended by the ohmic heating source to replace this pair. The results in a further power loss of 2.5kW.

Encore could be operated using noble gases or hydrogen. Hydrogen discharges tended to have poor shot to shot reproducibility. Being more easily ionized than hydrogen, argon gave more reproducible discharges and also produced several convenient and highly populated metastable states on which LIF experiments could be performed. In addition, argon plasmas did not have the high levels of x-ray emission associated with hydrogen discharges.

## 2.2 CVL PUMPED DYE LASER SYSTEM

A full description of the laser induced fluorescence (LIF) technique will be deferred until the next chapter. At this point, suffice it to say that we desired to use LIF to scan the Doppler-broadened, ion velocity distribution function. In order to do this, a tunable narrow band source of laser radiation was required. The laser system selected for the present work was a narrow-band, tunable dye laser (Lambda Physik model FL 2001) pumped by a copper vapor laser (Plasma Kinetics model 451). See Fig. 2.4. Coarse tuning of the dye laser was performed using a prism beam expander and a grating with a resolution of $0.2\text{cm}^{-1}$. The linewidth of the dye laser was narrowed by means of an intracavity Fabry-Perot etalon. The free spectral range of the etalon was $1\text{cm}^{-1}$ and the finesse was 38, giving a resolution of $0.035\text{cm}^{-1}$. In order to ensure single- mode operation when using the Fabry-Perot etalon, it was necessary that the grating bandpass coincide with one of the transmission maxima of the etalon (refer to Fig. 2.5). This could be done by viewing

(a)
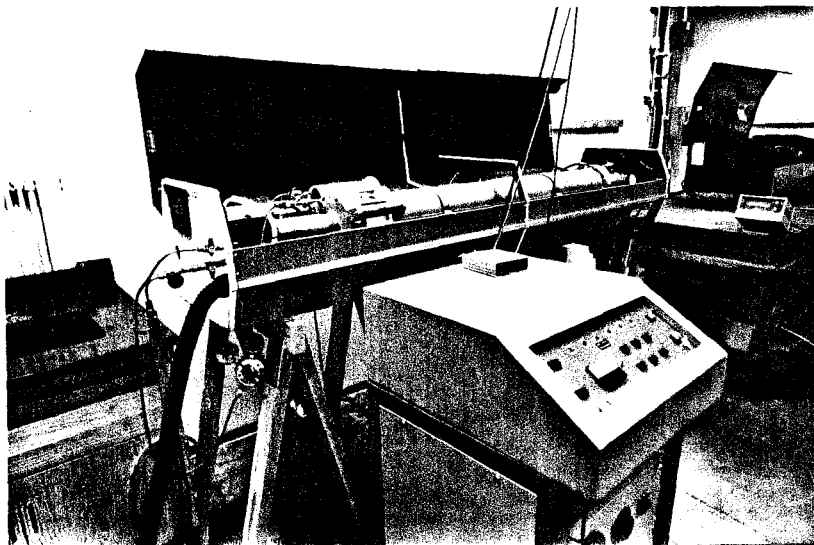
(b)
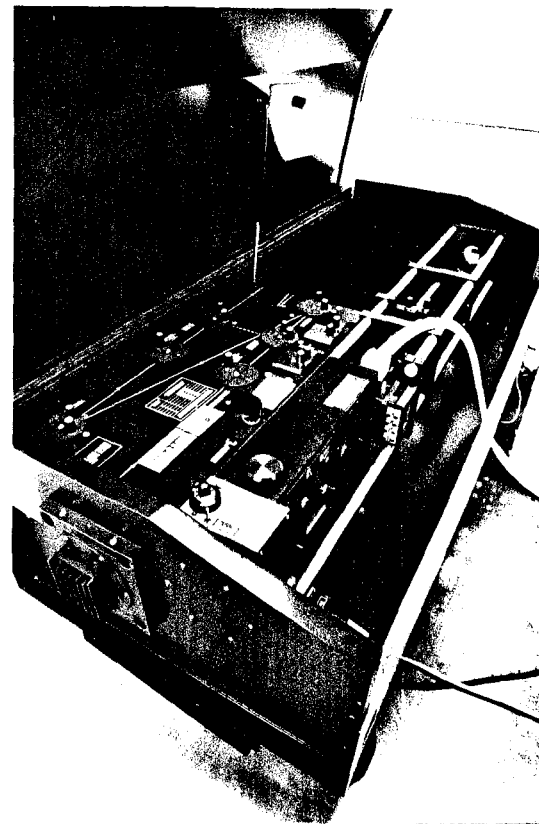
FIG. 2.4  The CVL pumped dye laser system. (a) Plasma Kinetics model 451 CVL.

(b) Lambda Physik FL2001 dye laser.

the laser output with an external Fabry-Perot possessing a higher resolution than that of the dye laser. As shown in Fig. 2.5, single-mode operation occurs when the monitor etalon shows sharp fringes.

When scanning the laser, it is necessary that the grating bandpass and the etalon transmission maximum continue to track each other. Both the grating and the intracavity etalon were moved by means of computer-controlled stepper motors. According to the Lambda Physik FL2001 instruction manual, the wavelength changes for the grating and the etalon are given by the following relations. For the grating,

$$d\lambda = 0.0084\text{nm steps/grating order}, \qquad (2.1)$$

whilst for the etalon,

$$d\lambda = -\lambda_0 \ \alpha \ d\alpha, \qquad (2.2)$$

where $\lambda_0$ is the central wavelength and $\alpha$ is the tuning angle. These relations were used in a Fortran computer program named SCAN to synchronize the grating and etalon positions.

The dye laser output was calibrated by means of an external Fabry-Perot interferometer (Spectra Physics model 410-G2). The free spectral range of this etalon is known to be 29.5GHz, allowing the bandwidth of the laser and the linearity of the scanning program to be determined. Figure 2.6(a) shows the output of the Fabry-Perot etalon measured using a photodiode and a boxcar averager. The distance between the two peaks corresponds to the free spectral range of the external etalon. From this plot, the linewidth of the laser line was found to be 1.3GHz. This value

Grating
0.2 cm$^{-1}$

Etalon
0.04 cm$^{-1}$

$\tilde{\nu}_{FSR}$ of intercavity etalon

LASER EMISSION

Single mode
Sharp monitor fringes

Double mode
diffuse monitor fringes
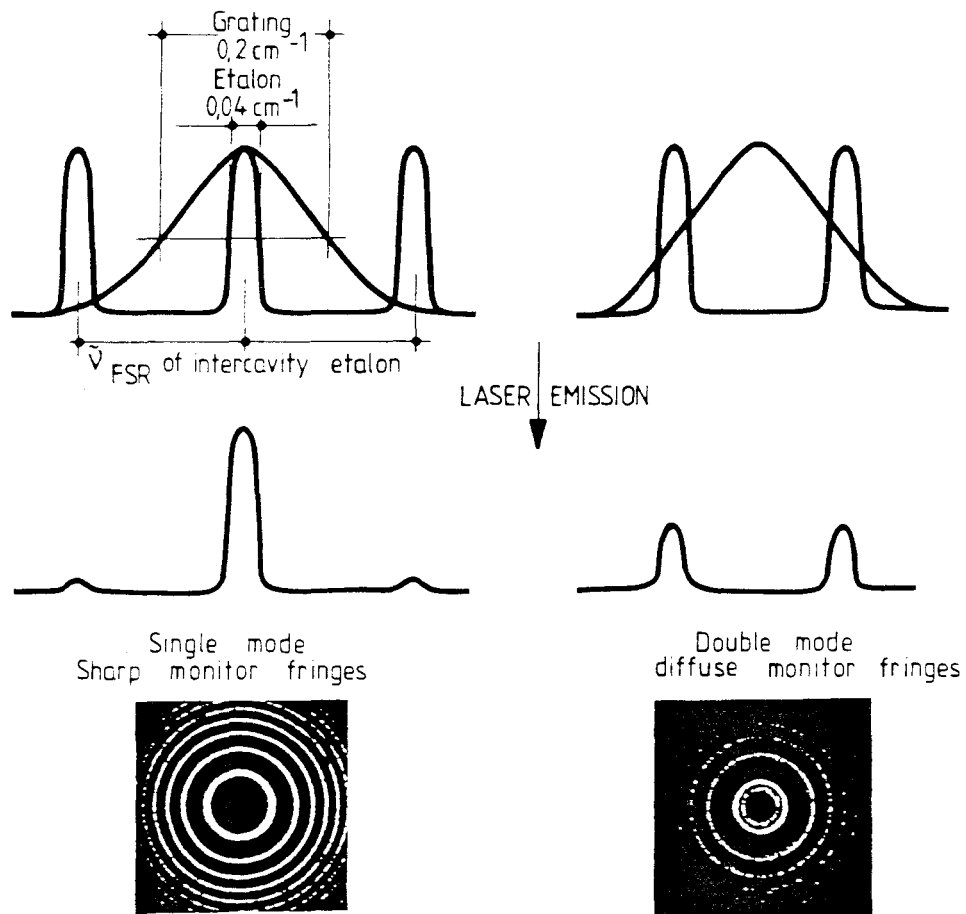
FIG. 2.5 Diagrams showing correct (left) and incorrect (right) alignment of the grating and etalon in the dye laser. Diagrams taken from Lambda Physik FL2001/2002 instruction manual.
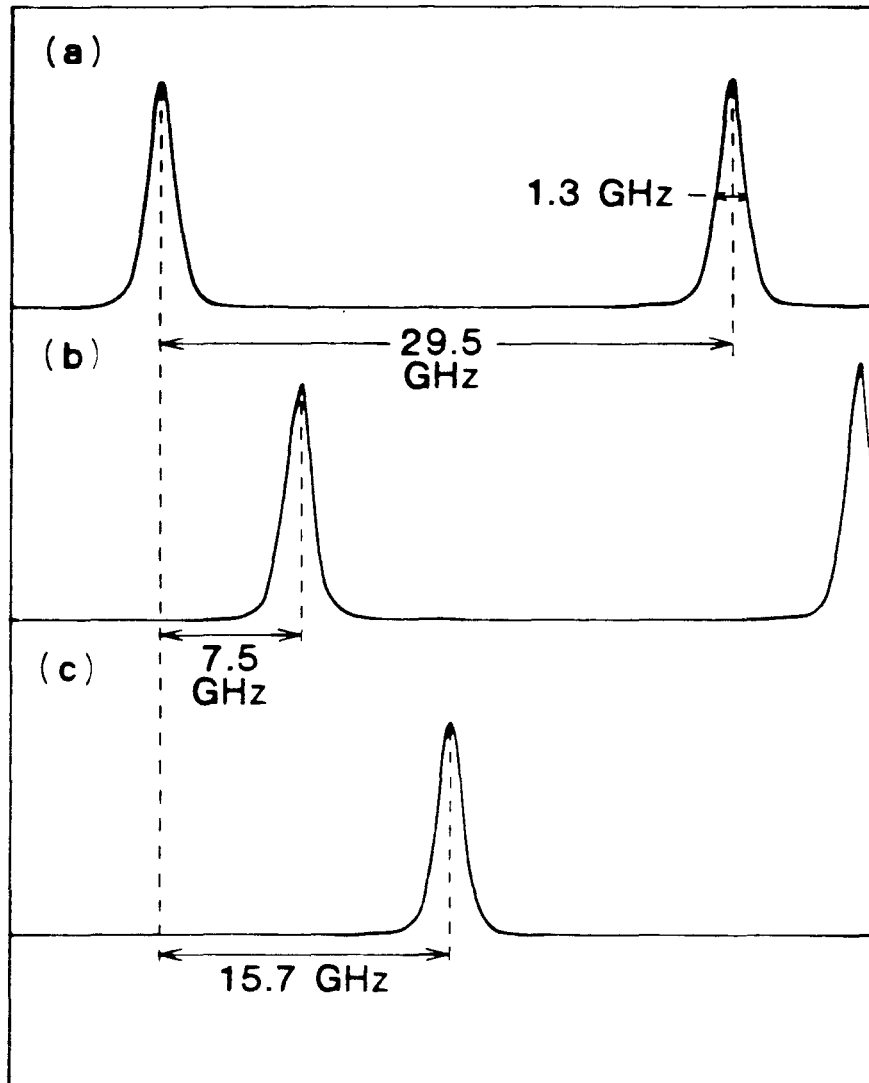
FIG. 2.6   Calibration of the FL2001 dye laser using an ex-
ternal etalon. Output of the etalon showing; (a) a scan
over the free spectral (29.5GHz), (b) the effect of scan-
ning the laser over 8GHz, and (c) the effect of scanning
the laser over 16GHz.

corresponds to an ion temperature resolution of 0.047eV in argon. Figures 2.6(b) and (c) show the effect of scanning the dye laser by 8.0GHz and 16.0GHz, respectively. The measured scans were actually 7.5GHz and 15.7GHz, giving scanning accuracies of a few percent.

The copper vapor laser (CVL) pump is characterized by a very high repetition rate of 4-6kHz, which allowed the tokamak to be run at high repetition rates of 15-30Hz. The laser tube consisted of a refractory ceramic surrounded by a stainless steel water jacket. An electrical discharge through the neon buffer gas heated the ceramic tube, causing the copper to be evaporated. The discharge also caused a population inversion in the copper atoms and hence lasing. Lasing occurred at 510nm and 578nm. Typical parameters for this laser are: repetition rate=6kHz, pulse length=30ns, pulse power=250kW, average power=40W and pulse jitter=3ns. The short pulse length meant that the time resolution of the system was much less than the scale times of the fastest phenomena observed in Encore ($\simeq 1\mu s$).

The pulse power of the CVL was less than the optimum power required to pump the Lambda Physik dye laser. Also, the CVL beam was 54mm in diameter and was not diffraction limited, which made focussing of the beam difficult. To obtain adequate pumping of the dye laser oscillator, it was necessary to design an unstable resonator cavity in order to minimize the output beam divergence. The details of this resonator are given in Appendix A. Using the unstable resonator optics, the beam divergence was reduced from $\sim$ 10mrad to $\sim$ 1mrad and the threshold for laser action was reduced from about 180kW to about 90kW.

The laser dye selected for the present work was Kiton Red 620. This dye has a lasing maximum at 620nm and a useful wavelength range of 595-639nm when
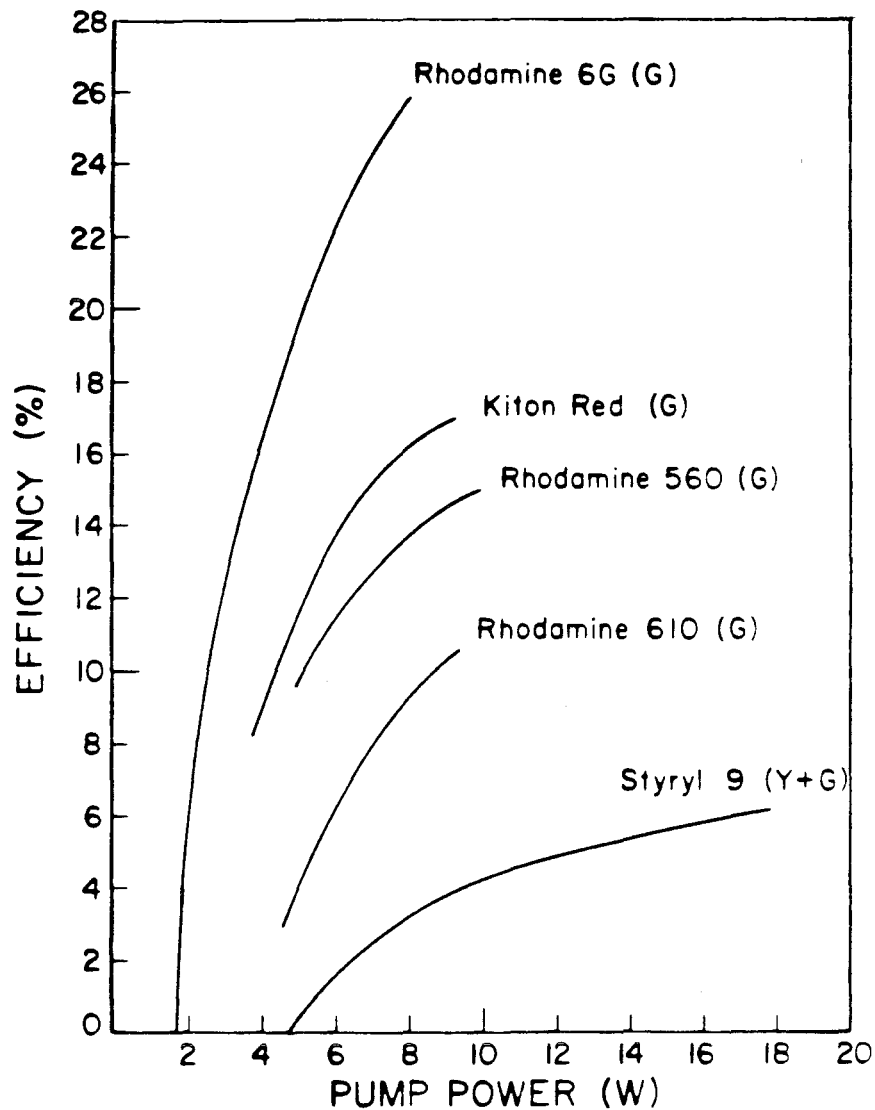
FIG. 2.7 Efficiency of various laser dyes as a func-
tion of CVL pump power. "G" stands for pumping with
the green line and "Y" stands for pumping with the
yellow line. Data supplied by W. Ruster.
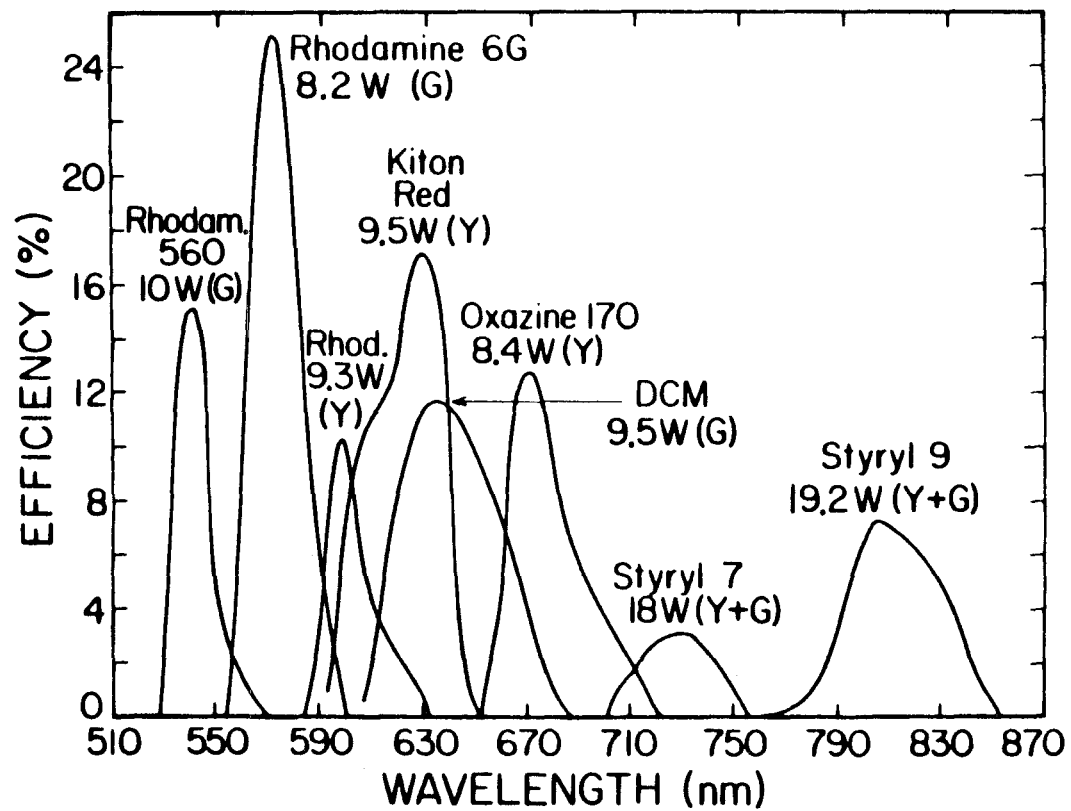
FIG. 2.8 Tuning curves for CVL pumping of various laser dyes. "G" stands for pumping with the green line and "Y" stands for pumping with the yellow line. Data supplied by W. Ruster.
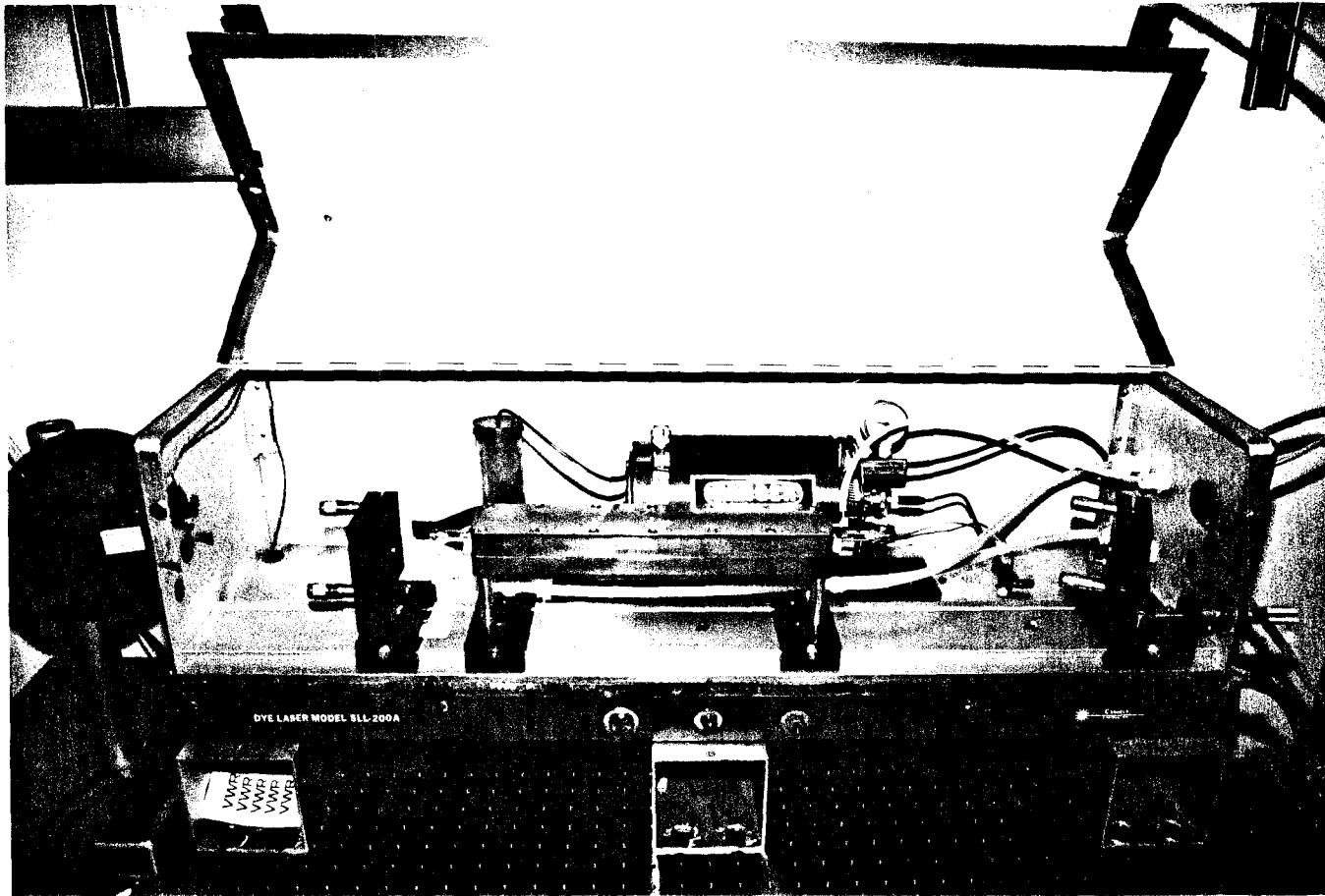
FIG. 2.9  The flashlamp pumped dye laser used for the optical tagging experiments.

The dye cell was constructed of quartz and was also 12 in. long with a 5mm bore. The construction of the cavity and dye cell are shown in Fig. 2.10. The windows were broadband-A.R. coated on one side and were then glued onto the dye cell by means of RTV silicone sealant. The lamp was energized by a $0.3\mu F$ capacitor, and the capacitor voltage was held off by a triggered spark gap. The laser output energy was ~100mJ with a pulse length of ~ 500ns (FWHM). The maximum repetition rate was 10Hz, although the laser was generally run at 5Hz. The laser was tuned by means of grating with 1200G/mm blazed for 500nm. Using this grating, the linewidth was about 0.2nm. This linewidth was 10-20 times the Doppler-broadened linewidth in argon plasmas. The spectral intensity, however, was still sufficient to ensure saturation of the transition. This allowed for efficient pumping of the target state. Maximum power in the range 610-620nm was obtained using a mixture of Rhodamine 610 and Rhodamine 590, the dye concentrations being 38mg $l^{-1}$ and 10mg $l^{-1}$, respectively. Kiton Red 620 was also used successfully.

## 2.4 EXPERIMENTAL LAYOUT AND TIMING

The layout of the apparatus was staightforward and is shown in Fig. 2.11. The probing laser beam was directed vertically into the plasma by means of a movable mirror. The fluorescence signal induced by this beam was viewed perpendicular to the beam direction by a simple lens/PMT combination. The lens was situated at a distance equal to twice its focal length from both the PMT and laser beam so that the object and the image sizes were identical. The focal length of the lens used was 15cm. An interference filter (linewidth 1nm) centered on the fluorescence line was used to remove all but the desired line. A 1mm diameter pinhole served to limit

**(a)**



**(b)**
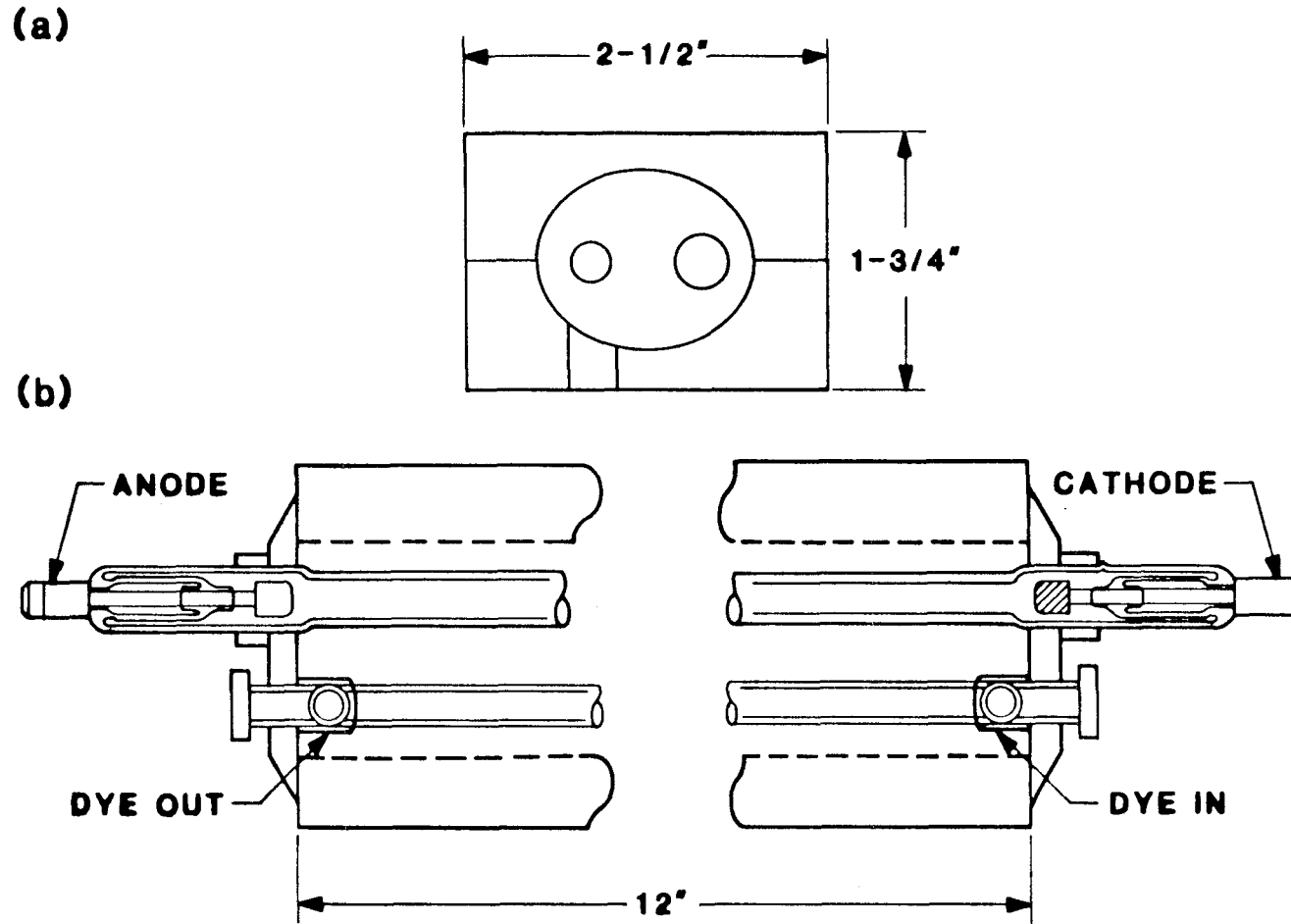
FIG. 2.10   Details of the elliptical cavity used in the flashlamp pumped dye laser. (a) End view showing the outline of the ellipse and the position of the flashlamp and dye cell. (b) Top view showing the mounting of the flashlamp and dye cell.

TO BOXCAR INTEGRATOR
AND COMPUTER

LASER OUT

TRANSLATOR

PMT

1mm PINHOLE
AND 1nm FILTER

2f

CONVERGING LENS
f = 15cm

1/2 WAVE RETARDER
POLARIZATION
ROTATOR

POLARIZER

TOKAMAK
CHAMBER

LASER IN

TRANSLATOR
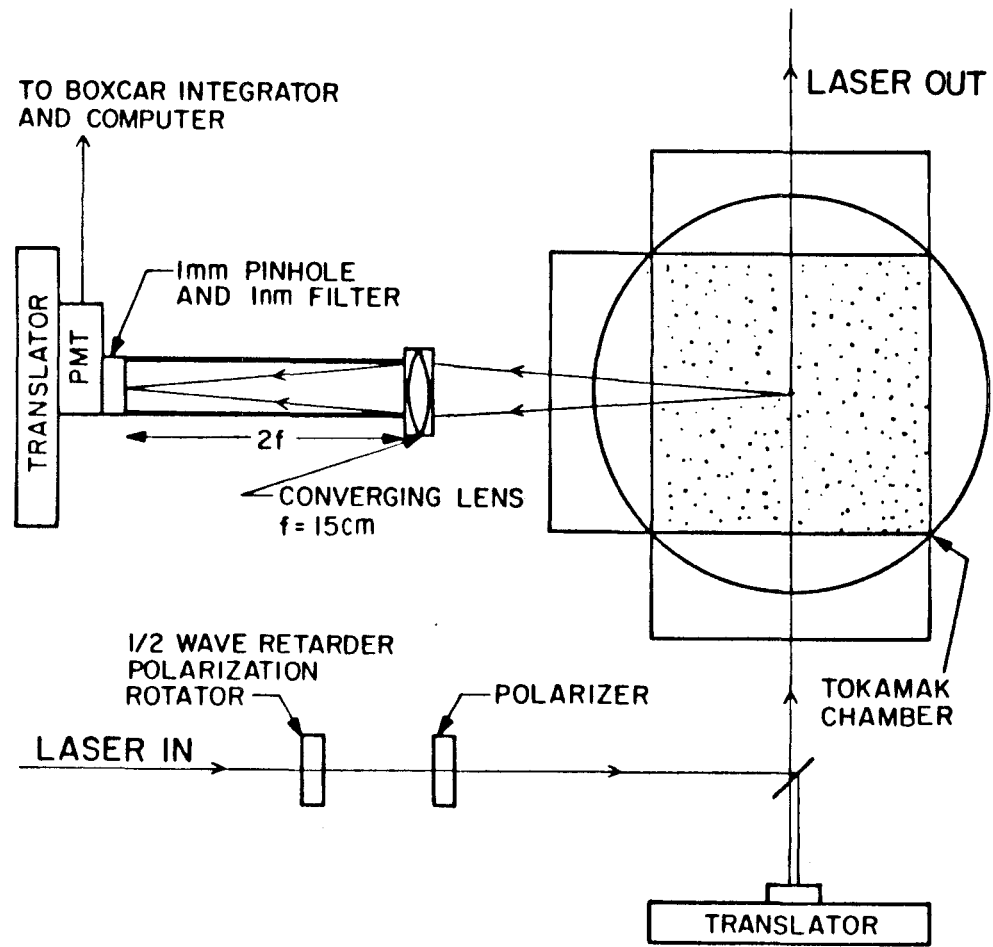
FIG. 2.11 Schematic showing the experimental layout.

the light incident on the PMT to acceptable levels and at the same time set the spatial resolution. The lens/PMT combination was also movable, allowing the entire shaded region shown in Fig. 2.11 to be interrogated. In addition, the translators were driven by computer- controlled stepper motors, allowing the scanning process to be fully automated. Finally, a polarization rotator and a polarizer were used to polarize the probe beam parallel to the toroidal field direction. As will be shown in Chap. 3, this was done to minimize the observed Zeeman splittings, which were generally negligible in any case.

The (pulsed) laser intensity at the output of the polarizer was $6\mathrm{MWm}^{-2}$; a value that was sufficient to ensure strong fluorescence signals, but low enough to prevent power broadening from occurring. For the optical tagging work, where the actual lineshape was unimportant, the intracavity etalon and the polarization rotator/polarizer combination were removed, and the laser intensity at the plasma was $20\mathrm{MWm}^{-2}$.

The CVL could be pulsed only at a constant rate, requiring the timing of the experiment to be slaved to the CVL, not a very satisfactory set of circumstances. A block diagram of the timing system is shown in Fig. 2.12. All trigger signals were derived from a single 6kHz oscillator, ensuring that laser, boxcar integrator and tokamak trigger signals were synchronous. The laser trigger was slightly delayed relative to the boxcar by means of a long length of coaxial cable. This delay was sufficient to ensure that the boxcar trigger preceded the laser trigger by about 50ns. This delay was necessary because the boxcar required at least 25ns between triggering and sampling.
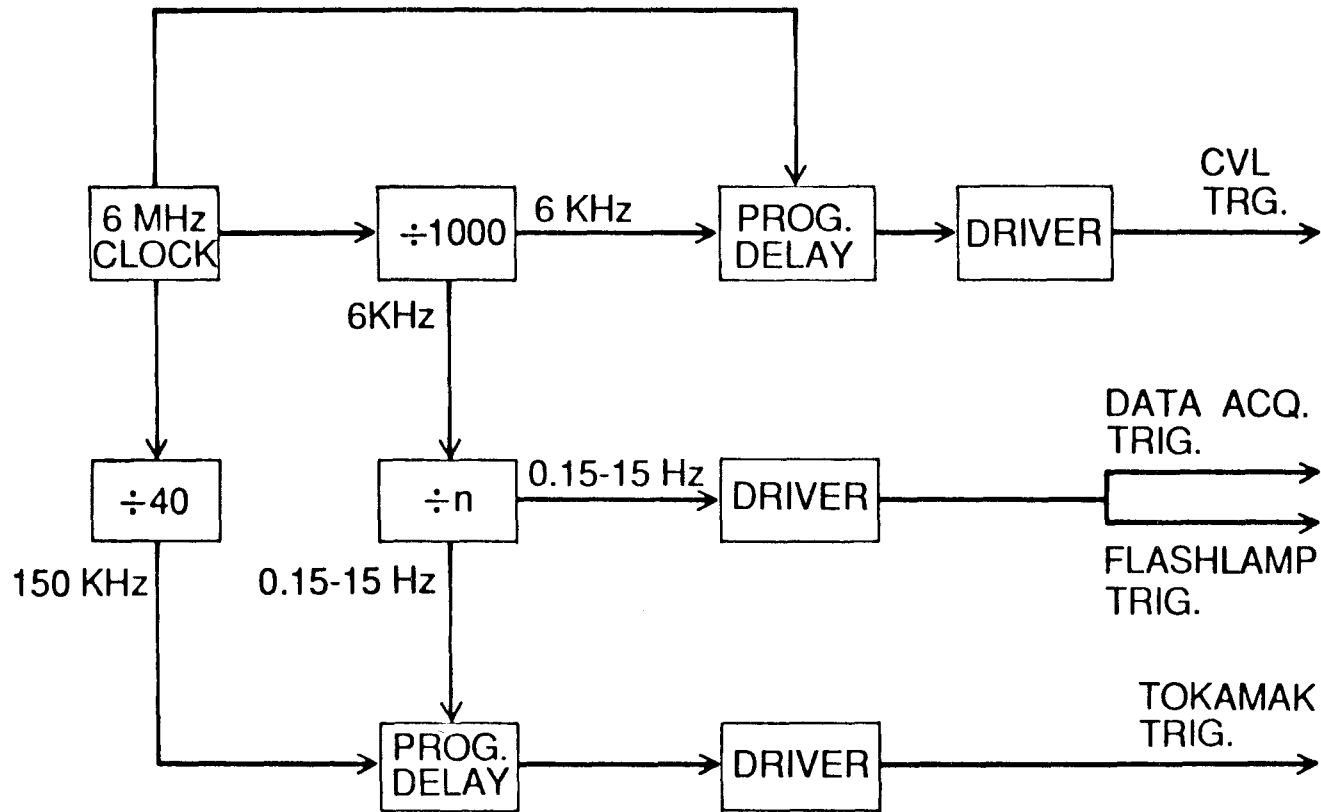
FIG. 2.12 Schematic of the timing circuit. The programmable delays were generated using the 6MHz clock giving a resolution of 167ns.

CHAPTER 3

LASER INDUCED FLUORESCENCE TECHNIQUES

## 3.1 INTRODUCTION

Laser induced fluorescence (LIF) is technique that has found application in many fields; including atomic physics, molecular physics and fluid dynamics. Its use as a plasma diagnostic was first suggested in 1968 by Measures (Measures, 1968). LIF is based upon the selective excitation of an atomic transition by the absorption of laser radiation of the appropriate wavelength. The chief attraction of the fluorescence method is its high sensitivity that is due to the large cross section for photoexcitation. This cross section is of the order of $\lambda^2/8\pi \sim 10^{-10} \text{cm}^2$ (Mitchell and Zemansky, 1934). This value is roughly 14 orders of magnitude larger than that for Thomson scattering. Once in the upper level, an atom or ion may decay via a different transition, emitting a photon having a different wavelength from the absorbed photon. This process is shown schematically in Fig. 3.1. This emission will, of course, originate from the region along the beam path. By viewing the emitted radiation perpendicular to the beam direction, the diagnosed volume will be determined by the intersection of the field of view of the viewing optics and the beam path.

In principle, LIF is capable of viewing virtually all plasma parameters of interest:

(i) ion and atomic velocity distribution functions (hence, ion and atomic temperatures) and densities;

(ii) ion and atomic particle trajectories;

FLUORESCENCE           LASER

$(^1D)4p^2\,F_{5/2}$

458.990 nm

617.228 nm

$(^1D)3d^2\,G_{7/2}$

$(^1D)4s^2\,D_{3/2}$
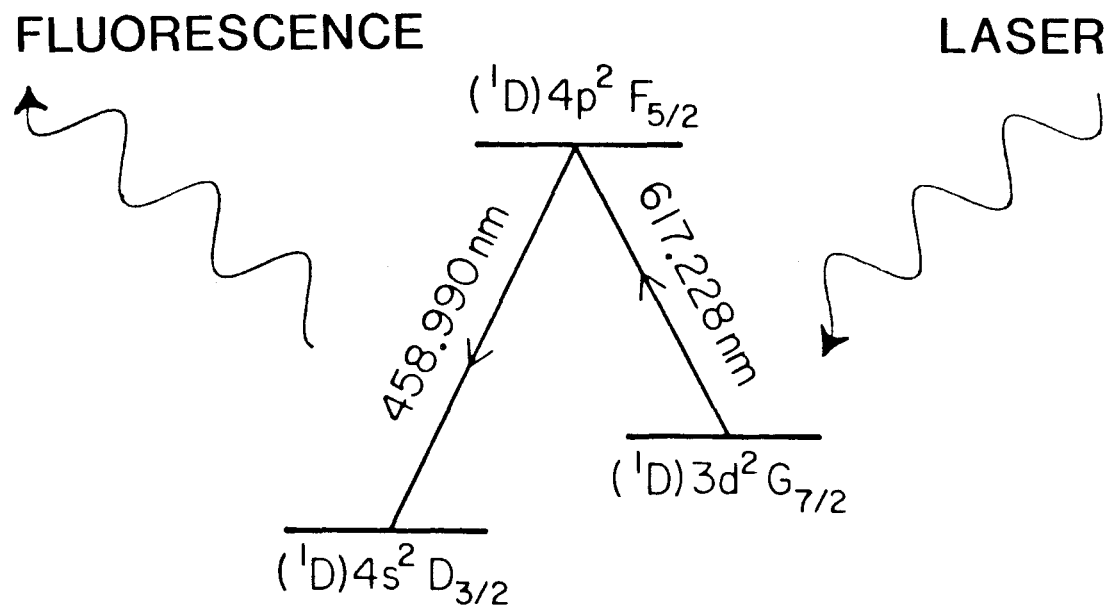
FIG. 3.1  Schematic demonstrating the principles of LIF. The particular transitions shown were used in the present work.

(iii) electron temperature from the relative populations of the excited levels;

(iv) the vector direction and magnitude of the local magnetic field by means of the Zeeman effect;

(v) the effective ion charge and the local electric field by means of the Stark effect.

In the present work, only techniques for (i) and (ii) will be discussed. Discussions of techniques (iv) and (v) can be found in the work of Moore et. al. (1984) and West et al. (1986), respectively. Technique (iii) can be applied only to high density plasmas, where the ions are in local thermodynamic equilibrium, i.e., the populations of the ionic states follow a Boltzmann distribution. Other examples of the application of LIF in laboratory and fusion plasmas include the work of Stern and Johnson (1975) (local ion densities and temperatures); Stern et al. (1983) (ion transport through optical tagging); Koslover and McWilliams (1986) (multidimensional, ion velocity distributions by optical tomography); Burakov et al. (1977) (local hydrogen densities in a tokamak); Muller and Burrell (1981) (metal impurity ion densities in a tokamak).

The LIF method does have limitations. Obviously, it cannot be applied to $H^+$ or other fully stripped ions. This deficiency immediately limits the use of the technique in fusion reactors. Strong background radiation may mask the emitted fluorescence radiation. In high density plasmas, the plasma may become optically thick and absorb the fluorescence signal. Also, it is essentially confined to the visible and near UV regions of the spectrum because convenient, tunable radiation sources are unavailable outside this region.

## 3.2 IONIC COMPOSITION OF ENCORE PLASMAS

Argon plasmas were used exclusively in the present work. Such plasmas were found to be particularly reproducible. In addition, several LIF schemes were possible in singly ionized argon plasmas. Spectroscopic studies indicated that argon discharges in Encore were for the most part singly ionized (Ar II). The intensities of Ar III lines were found to be considerably lower than the intensities of Ar II lines. No Ar IV lines were observed. Fig. 3.2 shows the relative intensities of various Ar II and Ar III lines during a typical discharge during which the plasma current was 1kA. For the lower plasma currents used in the present work, the ratio of Ar III to Ar II line intensities were even lower than indicated by Fig. 3.2. This observation was somewhat surprising since a charge state of $Z = 4 - 5$ would be expected if the plasma assumed a coronal equilibrium.

At this point, a digression concerning the relative abundance of Ar II and Ar III is in order. If plasma confinement times are long compared to collision times, then the ionization state will reach some equilibrium. In low density, relatively hot plasmas, the equilibrium charge state may be found by balancing the rates of collisional ionization with the rates of radiative recombination. Such an equilibrium is known as coronal equilibrium. For high density plasmas, collisional or three-body recombination will balance collisional ionization, and the relative populations of the various ionization states will follow the well-known Saha equation. The plasma is then said to be in local thermodynamic equilibrium (LTE). A complete discussion of these ideas may be found in the work of Griem (1964). On the basis of density and temperature, one might propose a coronal equilibrium model to describe Encore plasmas and hence suspect that the dominant charge state was
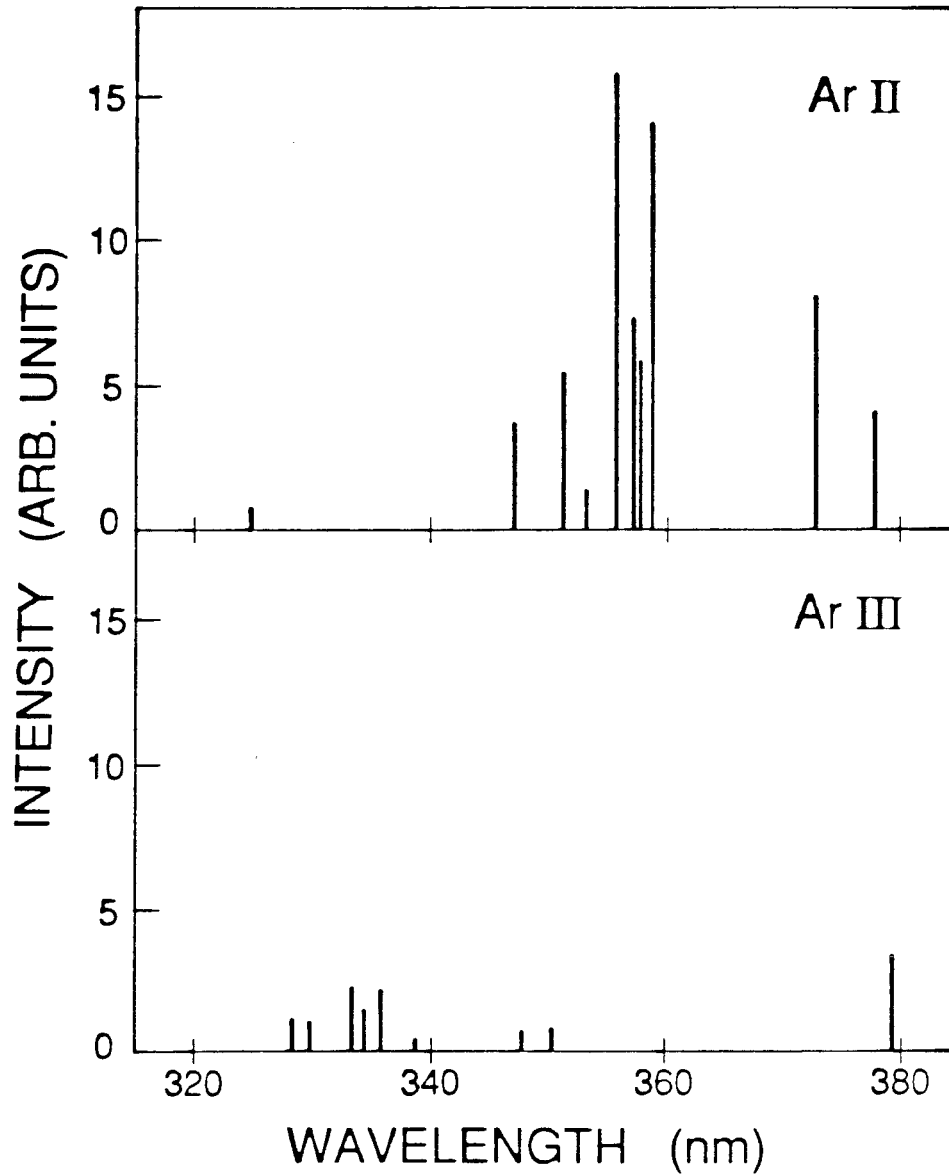
FIG. 3.2  Relative intensities of ArII and ArIII lines
in the range 320-380nm for a typical Encore discharge.
The plasma current was 1kA and the field strength was
350G.

$Z = 4 - 5$. The solution to the paradox presented above, is of course, that the ions never achieve coronal equilibrium or LTE. Ion confinement times in Encore are rather low, and the ions are lost before reaching equilibrium. It is relatively straightforward to calculate the densities of each of the first few ionization states of argon by solving the rate equations on a computer. The collisional ionization rate coefficients for the various charge states of argon were determined using the semiempirical formula given by Müller et al. (1980). These coefficients were found to be very similar to those calculated using the formulae given by Lotz (1968). The rate coefficients for radiative recombination can be calculated using the formulae given by McWhirter (1965). The rate coefficients for radiative recombination are negligible for the first few ionization states of argon, and so were ignored in the calculations. The results of these calculations are shown in Fig. 3.3. The density and electron temperature assumed were $5 \times 10^{11} \text{cm}^{-3}$ and 12eV, respectively. Also plotted is $Z_{eff} = \Sigma n_Z Z^2 / n_e$. For the first $300\mu s$, the population of Ar II exceeds that of Ar III, and the population of Ar IV is negligible. For the first $500\mu s$, $Z_{eff}$ was less than 2. Ion confinement times are estimated to be around $300\mu s$, and few multiply ionized argon ions will be observed. These calculations neglected the fact that density and temperature fall off toward the plasma edge resulting in even lower ionization rates and lower $Z_{eff}$ away from from the plasma center.

## 3.3 FLUORESCENCE SCHEMES IN SINGLY IONIZED ARGON

Examples of Ar II fluorescence schemes are shown in Fig. 3.4. For all these schemes, the fluorescence lines are different from the exciting laser lines. The scheme selected for most of the present work was that shown in Fig. 3.4(a). This scheme
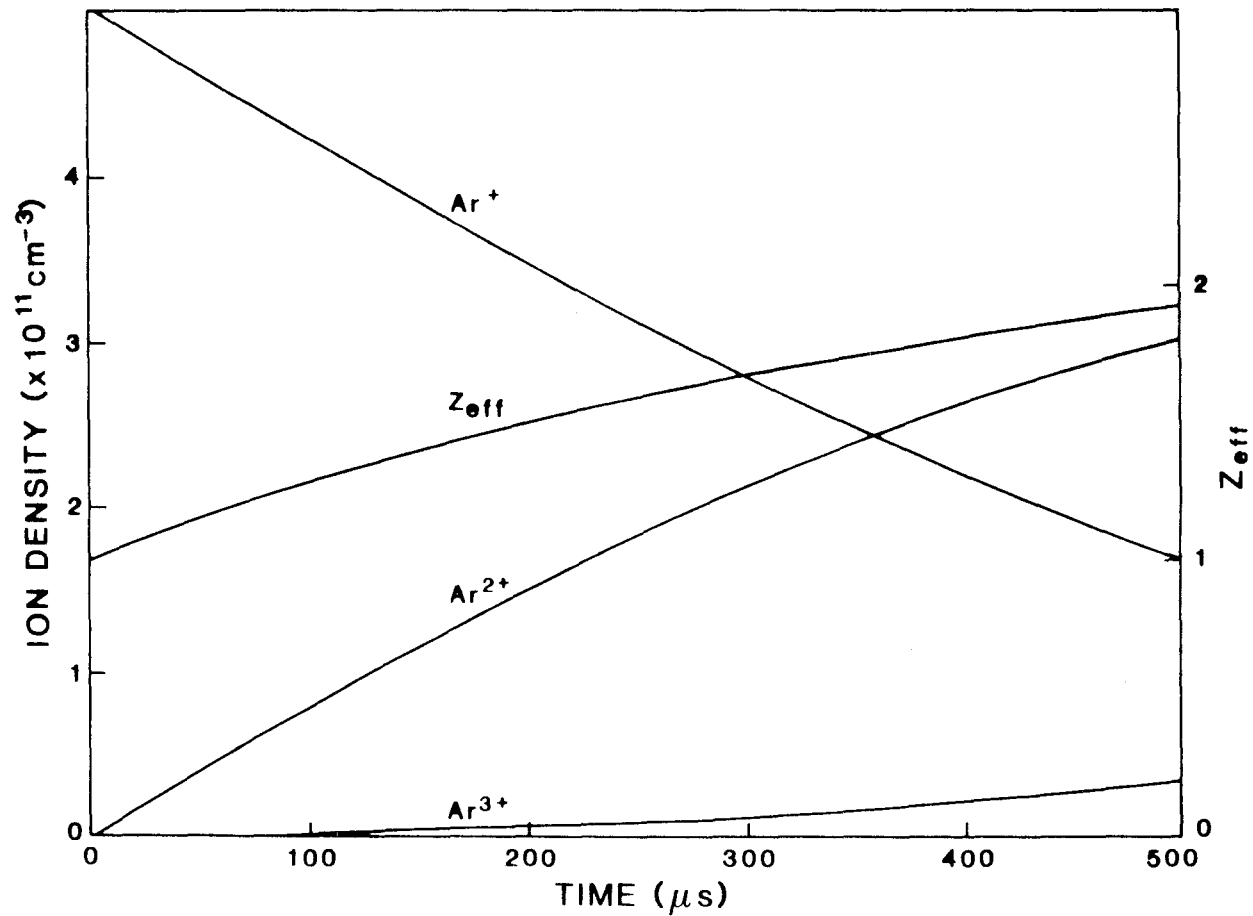
FIG. 3.3 Calculations showing the relative densities of singly, doubly and triply ionized argon as a function of time. Also plotted is the effective ion charge $Z_{eff}$. We assumed that $T_e = 12eV$ and $n_e = 5 \times 10^{11} cm^{-3}$.

33

**(a)** $4p^2F_{7/2}$

461.0    611.5

$4s^2D_{5/2}$    $3d^2G_{9/2}$ (metastable)

**(b)** $4p^2F_{5/2}$

459.0    617.2

$4s^2D_{3/2}$    $3d^2G_{7/2}$ (metastable)

**(c)** $4p^4D_{7/2}$

401.4    688.7

$4d^4D_{7/2}$ (metastable)    $3d^4F_{7/2}$ (metastable)

**(d)** $4p^4D_{7/2}$

401.4    664.4

$4d^4D_{7/2}$ (metastable)    $3d^4F_{9/2}$ (metastable)

**(e)** $4p^2F_{7/2}$

461.0    612.3

$4s^2D_{5/2}$    $3d^2G_{7/2}$ (metastable)
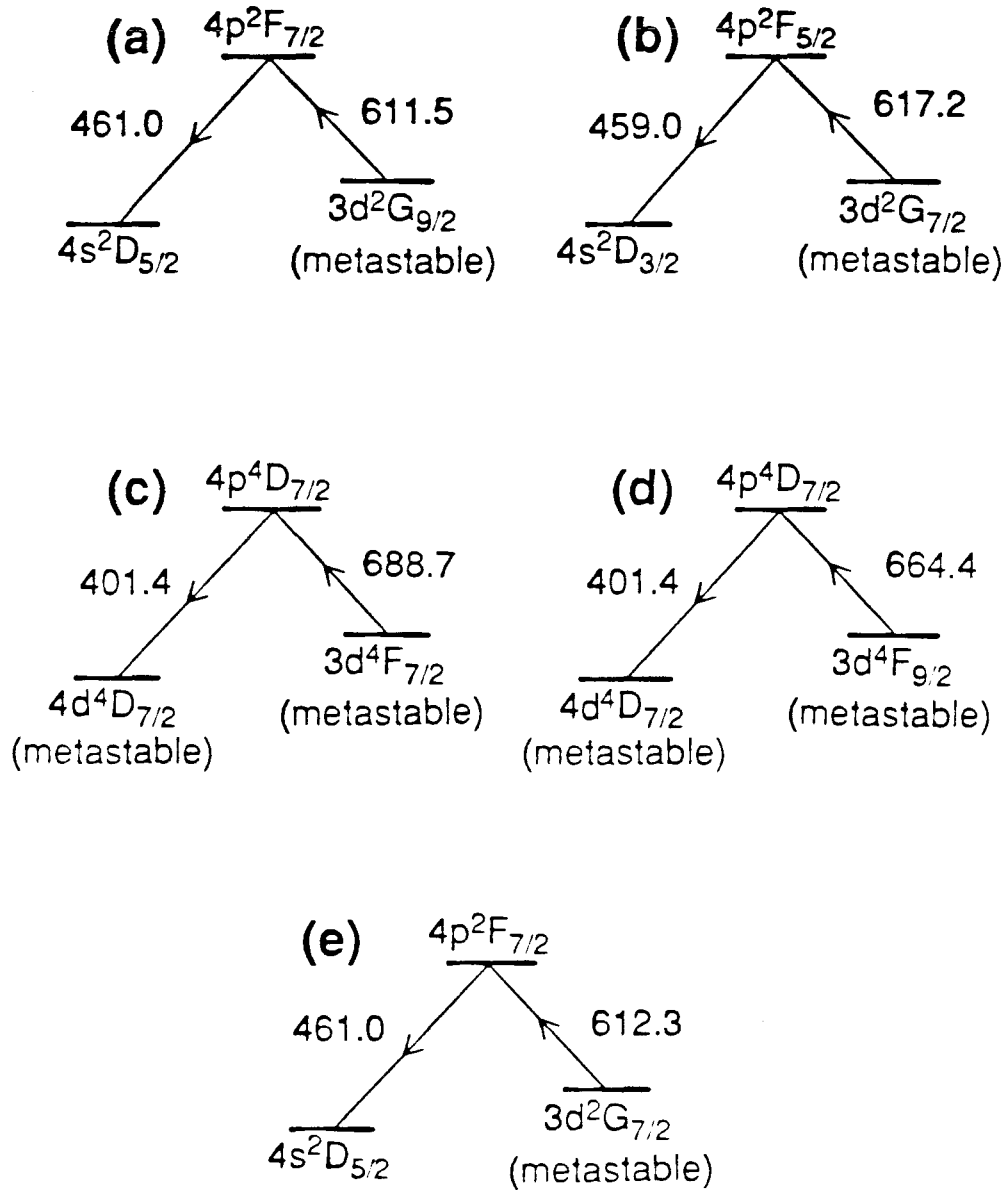
FIG. 3.4 Possible fluorescence schemes in ArII. Only Schemes (a) and (b) were used in the present work.

was particularly convenient because the excitation line was in the red region of the spectrum, where several efficient laser dyes can be used. In addition, the fluorescence line was in the blue, where photomultiplier tubes are particularly efficient. In all the schemes shown in Fig. 3.4, the target state was an elevated metastable state (not the ground state), allowing visible laser radiation to be used. Note that in Figs. 3.4(c) and 3.4(d), the final state is also metastable. Once a convenient fluorescence scheme had been selected, it was possible to obtain the ion velocity distribution function by scanning the narrowband dye laser across the Doppler-broadened absorption line. This technique will be discussed in Section 3.4.1. It is important to ensure that all line broadening mechanisms other than Doppler broadening are negligible, or can be corrected for. This will also be discussed in succeeding sections.

## 3.4 LINE BROADENING MECHANISMS

## 3.4.1 DOPPLER BROADENING

We will now turn our attention to the determination of the one-dimensional ion velocity distribution function by means of Doppler-broadening of the ion absorption line. All plasma emission or absorption lines exhibit line broadening, which may be due to one or more possible line broadening mechanisms. Plasma radiation lines often exhibit significant Doppler broadening in addition to their natural linewidths. In low to moderate density plasmas, Doppler broadening is generally the dominant broadening mechanism. The natural linewidth is determined by the uncertainty relation $\Delta\nu\,\Delta t \sim 1$. For a line at 500nm, the natural linewidth is approximately $10^{-4}$nm, while the Doppler width for the same line in a 10eV argon plasma is approximately $2 \times 10^{-2}$nm.

Doppler broadening is due to the random thermal motion of the radiating species. If a radiating particle is moving away from an observer at a velocity $u_x$, then the wavelength of the light as seen by the observer ($\lambda$) is Doppler-shifted away from the wavelength in the rest frame ($\lambda_0$) according to the relation,

$$\frac{\lambda - \lambda_0}{\lambda_0} = \frac{u_x}{c}. \tag{3.1}$$

Emitters in a plasma have a distribution of velocities, so that the light intensity $I$ at a wavelength $\lambda$ is proportional to the number of emitters having a particular value of $u_x$, i.e., $I(\lambda)d\lambda \sim f(u_x)du_x$. Plasma velocity distributions are often Maxwellian and can be expressed in the form,

$$f(u_x) = \sqrt{\frac{m_i}{2\pi\kappa T_i}} \exp\left(\frac{-m_i u_x^2}{2\kappa T_i}\right). \tag{3.2}$$

Substituting for $u_x$ from Eq. 3.1 gives the Doppler-broadened intensity distribution function as a function of wavelength, i.e.,

$$I_D(\lambda) = \sqrt{\frac{m_i c^2}{2\pi\kappa T_i \lambda_0^2}} \exp\left(\frac{-m_i c^2 (\lambda - \lambda_0)^2}{2\kappa T_i \lambda_0^2}\right). \tag{3.3}$$

Equation 3.3 has been normalized so that $\int I_D(\lambda)d\lambda = 1$. The half-width for such a Doppler broadened spectrum is given by,

$$\Delta\lambda_{1/2} = 7.7 \times 10^{-5}\lambda_0\sqrt{\frac{T_i}{\mu}}, \tag{3.4}$$

where $T_i$ is the ion temperature in eV and $\mu$ is the mass number of the ion. The above discussion applies equally well to plasma emission lines and, in our work, it was actually the emission line that was scanned by means of a tunable laser source.

## 3.4.2 STARK BROADENING

In dense ($> 10^{16} \text{cm}^{-3}$) plasmas, both the natural linewidth and the Doppler width are often negligible compared to the linewidths of the so-called pressure-broadening mechanisms. These are associated with the interaction of the radiating particles with surrounding atoms or ions. Pressure broadening includes the effects of collisions with neutral particles (van der Waals broadening), resonance interactions between identical particles (resonance broadening), and collisions with charged particles (Stark broadening). The first two mechanisms are more important for slightly ionized plasmas, while the last is most important for highly ionized, high density plasmas. Encore plasmas are highly ionized so van der Waals and resonance broadening play no role. Strong electric fields produce splitting of atomic energy levels, so that the spectral lines resulting from transitions between the levels are also split (Stark effect). Collisions with charged particles produce locally strong electric fields in high density plasmas. Since these electric fields are random in magnitude and direction, the observed spectral lines appear broadened rather than as distinct lines. Stark broadening profiles may be approximated by a Lorentzian lineshape,

$$I(\lambda) \sim \left( 1 + \frac{4(\lambda - \lambda_0)^2}{\Delta \lambda^2} \right)^{-1}. \tag{3.5}$$

Stark broadening is the most important of the pressure broadening mechanisms, but produces negligible line broadening in Encore plasmas. An extensive discussion of Stark broadening may be found in the work of Griem (1964). He gives the following expression for the FWHM for Stark-broadened lines of singly ionized ions (in nm).

$$\Delta\lambda_{1/2} = 2 \times 10^{-17}\left[1 + 1.75 \times 10^{-4}\alpha\left(1 - 1.02 \times 10^{-3}\frac{n_e^{1/6}}{T_e^{1/2}}\right)\right]wn_e, \qquad (3.6)$$

where $n_e$ is the electron density in $\text{cm}^{-3}$, $T_e$ is the electron temperature in eV and $\alpha$, $w$ are tabulated parameters. For typical Encore parameters of $n_e = 1 \times 10^{12}\text{cm}^{-3}$, $T_e = 8\text{eV}$ we obtain $\Delta\lambda_{1/2} = 2 \times 10^{-7}\text{nm}$, which is negligible compared to the Doppler width and even the natural linewidth.

### 3.4.3 INSTRUMENTAL BROADENING

The only other broadening mechanism that can play a role in our work is instrumental broadening that is due to the finite linewidth of the laser. The laser linewidth was determined by the finite resolution of the intracavity etalon, which was $0.035\text{cm}^{-1}$. This gave an effective ion temperature resolution of $0.03\text{eV}$ at $611.5\text{nm}$. This linewidth was small when compared to the observed Doppler widths. However, for the sake of completeness, the observed Doppler lineshape was corrected for instrumental broadening during data reduction. This correction was carried out in the following fashion. If two statistically independent, linebroadening mechanisms resulting in lineshapes of $I_1(\Delta\lambda)$ and $I_2(\Delta\lambda)$, respectively, are simultaneously at work, then the resultant lineshape is given by the convolution of the two component lineshapes (Griem, 1964),

$$I_{obs}(\Delta\lambda) = \int\limits_{-\infty}^{+\infty} I_1(\Delta\lambda - \Delta\lambda')I_2(\Delta\lambda')\mathrm{d}\Delta\lambda'. \qquad (3.7)$$

The reason for this convolution product may be seen as follows. If only line broadening mechanism "2" is present, then the line intensity at a wavelength distance

$\Delta\lambda'$ from the line center is given by $I_2(\Delta\lambda')$. With broadening mechanism "1" also present, this intensity is smeared out over all other positions of the line. Hence, at the position $\Delta\lambda$ the total intensity is given by the product of $I_2(\Delta\lambda')$ and the function "1" centered at $\Delta\lambda'$ viz., $I_1(\Delta\lambda - \Delta\lambda')$. The final result is then obtained by integration over all possible contributions. For our case, $I_2$ is a gaussian of the form given in Eq. 3.3, and $I_1$ is assumed to be a Fabry-Perot "comb" function that takes the form (Hecht and Zajac, 1974)

$$\frac{I_1(\Delta\lambda)}{I_0} = \left[1 + \left(\frac{2F}{\pi}\right)^2 \sin^2\left(2\frac{\pi\Delta\lambda}{\Delta\lambda_{fsr}}\right)\right]^{-1}, \qquad (3.8)$$

where $\Delta\lambda_{fsr}$ is the free spectral range and $F$ is the finesse. The ion temperature may now be found iteratively by evaluating the integral $\int I_1(\Delta\lambda - \Delta\lambda')I_2(\Delta\lambda')d\Delta\lambda'$ for different assumed ion temperatures until the difference between $I_{obs}$ and the integral is minimized.

If the pulsed laser power is too high, the effective laser linewidth may be increased by power broadening effects. Power (or saturation) broadening occurs when the stimulated photon emission rate equals the photon absorption rate and both are greater than the spontaneous photon emission rate. Further increases in the laser intensity will not change this balance. When saturation occurs, the power residing in the wings of the laser line becomes important, resulting in photon absorption far from the laser line center and therefore extra line broadening. A simple check on the possible effects of power broadening was made. The laser intensity was progressively reduced by means of neutral density filters, and the Doppler lineshape was measured at each stage. No change in the lineshape was discernible. Goeckner and Goree (1988), have studied the effects of pumping the $3d^2G_{9/2} \rightarrow 4p^2F_{7/2}$

ArII transition, by a 1GHz bandwidth laser. For $T_i \sim 0.5\text{eV}$, they found negligible power broadening for laser intensities $< 5\text{MWm}^{-2}$. For $T_i \sim 0.1\text{eV}$, they found power broadening was negligible for intensities $< 500\text{kWm}^{-2}$, but appreciable when the intensity was increased to $5\text{MWm}^{-2}$. At the latter intensity level the Doppler linewidth of $T_i \sim 0.1\text{eV}$ ions was increased by about 50%. The measured laser intensity in our work was $6\text{MWm}^{-2}$. It is therefore possible, that power broadening was significant for the lowest temperature measurements in our work ($T_i < 0.2\text{eV}$). We did not, however, check this experimentally.

## 3.4.4 ZEEMAN SPLITTING OF THE ABSORPTION LINES

The interaction of the magnetic moment of an atom with an applied magnetic field results in the splitting of the observed spectral lines. In the so-called "normal" Zeeman effect, the single line splits into three polarized components. In the "anomalous" Zeeman effect, the single line is not split into a single triplet but into a group of four or more components.

When a spectral line splits in a magnetic field, the Zeeman components are polarized either parallel or perpendicular to the magnetic field; the former are known as $\pi$ components, while the latter are known as $\sigma$ components. The Zeeman components are always shifted symmetrically about the position of the undisplaced line. In the "normal" triplet, the three components arising from the line of frequency $f$ have frequencies of $f, f+\Delta f$ and $f-\Delta f$. The undisplaced line is the $\pi$ component, and the two displaced lines are the $\sigma$ components. The $\pi$ component is linearly polarized along the magnetic field direction, while the $\sigma$ components are circularly polarized perpendicular to the field. The $\sigma$ components rotate in opposite directions.

Numerically, these Zeeman shifts are of the order of $\Delta\lambda \simeq 10^{-9}\lambda^2 B$, where

the wavelengths are in Angstrom units and the magnetic field is in kilogauss. For $B \sim 1kG$ and $\lambda \sim 600nm$ the shift is $\sim 4 \times 10^{-3}nm$, resulting in a slight broadening of the observed Doppler-broadened distribution. Because the Doppler broadening masks the individual Zeeman components, it is impossible to unfold the Doppler broadening directly from the Zeeman components. However, by polarizing the probing laser beam, it is possible to excite only the $\pi$ transitions. The splittings of the individual $\pi$ components are much smaller than those between the $\pi$ and $\sigma$ components and therefore are much smaller than the observed Doppler broadening. Figure 3.5 shows the Zeeman structure for the transition $3d^2G_{9/2} \rightarrow 4p^2F_{7/2}$; the magnetic field assumed was 1kG. The numbers next to each line represent the relative Zeeman line intensities. Also shown are the maximum $\pi$ and $\sigma$ splittings of $1.94 \times 10^{-4}nm$ and $2.13 \times 10^{-3}nm$ respectively. For comparison the FWHM for 2eV argon ions is $1.05 \times 10^{-2}nm$.

## 3.5 MEASUREMENTS OF ION DISTRIBUTION FUNCTIONS

From the above discussion, it is clear that the dominant line broadening-mechanism in Encore is Doppler broadening. Figure 3.6 shows several ion velocity distribution functions obtained by LIF. The LIF scheme used for these data was that shown in Fig. 3.4(b). These distribution functions were obtained during the application of lower hybrid RF power. As the RF power level was increased from zero to 16kW, a clear rise in ion temperature was observed. The ohmic heating power applied during these discharges was about 20kW, so that the RF power was a substantial fraction of the total power deposited into the plasma. It is not the intention of the present work to discuss lower hybrid heating; these data are pre-

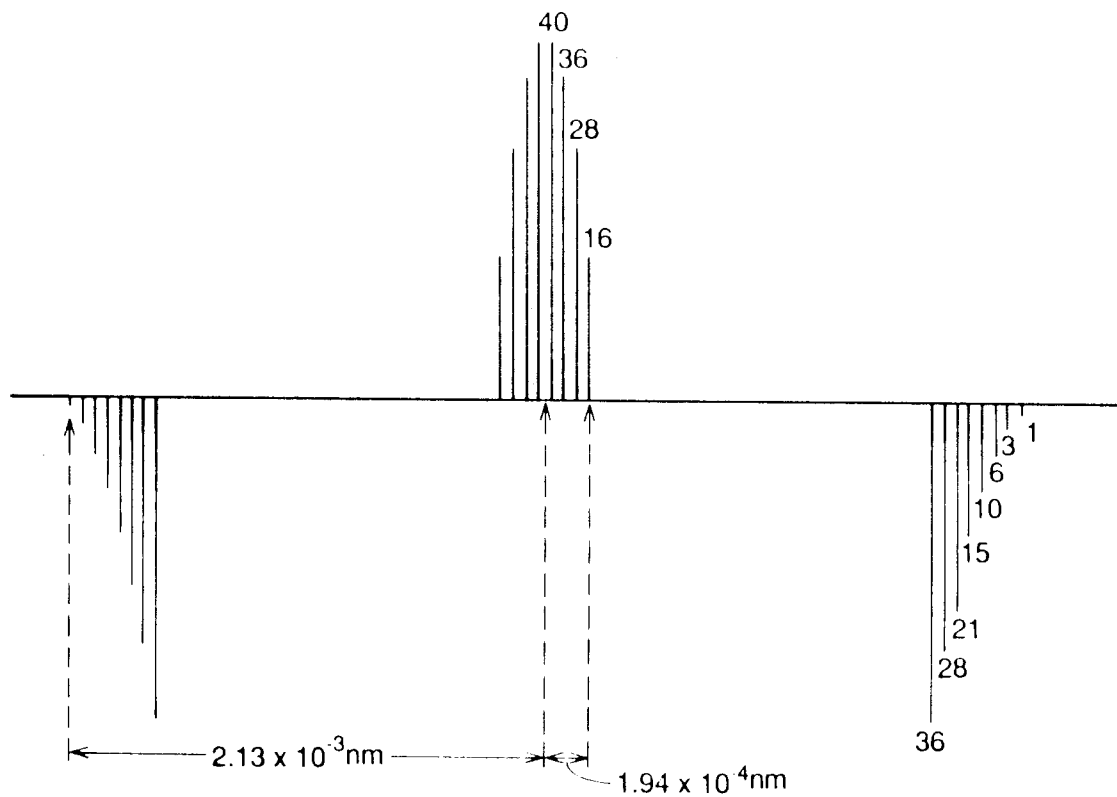FIG. 3.5   Zeeman structure for the transition $3d^2G_{9/2}$ to $4p^2F_{7/2}$. The magnetic field was assumed to be 1kG.
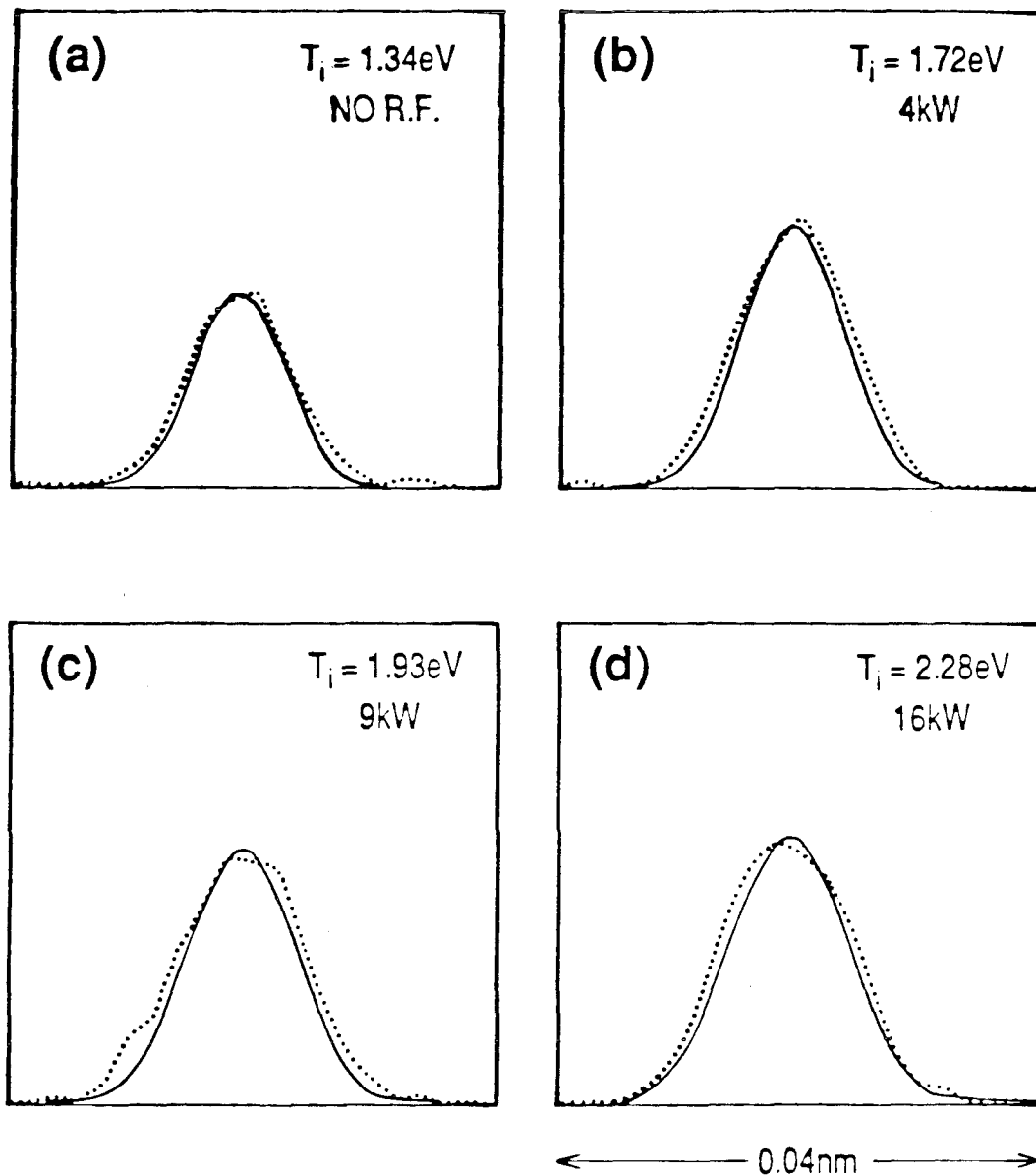
FIG. 3.6 Ion distribution functions obtained during the application of lower hybrid R.F. power. The dotted curves are actual LIF determined distribution functions. The solid curves are the Gaussian fits to the data, which have been corrected for the effects of finite laser linewidth.

sented purely to demonstrate the LIF technique. To obtain these plots, the laser wavelength was scanned through 0.04nm in steps of 0.002nm. At each step the photomultiplier signal was averaged 100 times using a boxcar averager (Stanford Research Systems model SR250), and the boxcar output was digitized for analysis. A Gaussian fit was then made to the digitized data. Only data points near the peak of the distribution function were used in the analysis. The Gaussian fitting routine involved taking logarithms of the digitized data, and in such circumstances the use of data points in the wings of the distribution function is dangerous because of the large relative errors in these points. In retrospect, it would have been preferable to fit the data directly to Gaussian without first taking logarithms in order to avoid this systematic error. However, due to the fairly large number of data points available from each scan, good fits to the data were still obtained. The distribution function was corrected in the same routine for the finite laser linewidth, as described in Sec. 3.4.3. This correction resulted in the width of the fitted Gaussian, being somewhat less than the width of the experimentally observed distribution function.

Signal averaging was necessary, partly because of shot-to-shot variations in the plasma breakdown and laser intensity, and partly because of the presence of ubiquitous plasma oscillations known as drift waves. The relative density fluctuations caused by these modes could reach 40% at the plasma edge. By averaging over 100 or more shots it was possible to reduce the noise level in the measured ion distribution functions to less than 4%, allowing good fits to be made to the data. It was seldom necessary to average to this extent, however, because most of our measurements were made at the plasma center, where the density fluctuation levels were negligible.

## 3.6 OPTICAL TAGGING

### 3.6.1 INTRODUCTION

Optical tagging is an extension of the LIF technique that allows the transport of small groups of ions to be determined (Stern et al., 1983). The technique requires a multilevel quantum system with at least one long- lived state.

Optical tagging can be demonstrated conceptually by considering a three-level system with two metastable states A and C. (Refer to Fig. 3.7.) A pump laser tuned to the transition A-B will decrease the density $(\rho_A)$ of A state ions and ultimately will increase the density of C state ions $(\rho_C)$ at the position of the pump laser (P). Suppose now that some or all of these pumped ions are transported to the position of a second laser beam (S). This laser we will call the search laser. If the search laser is tuned to any transition having either A or C as its lower level, it will induce a fluorescence signal with an intensity that is dependent on either $\rho_A$ or $\rho_C$ as chosen. For instance, if the search laser is tuned to a transition with state A as the lower level, the intensity of the fluorescence signal obtained will be reduced since we have reduced the density of target states by means of the pump laser. Conversely, if the search laser is tuned to a transition having state C as its lower level, the fluorescence signal induced will be increased. The modification to the fluorescence signal reflects species transport from position P to position S. The first mode of operation is referred to as "dark signal" operation while the second mode is referred to as "bright signal" operation.

### 3.6.2 LIFETIMES OF TAGGED STATES

Clearly, the utility of this method is limited by the lifetime of the metastable
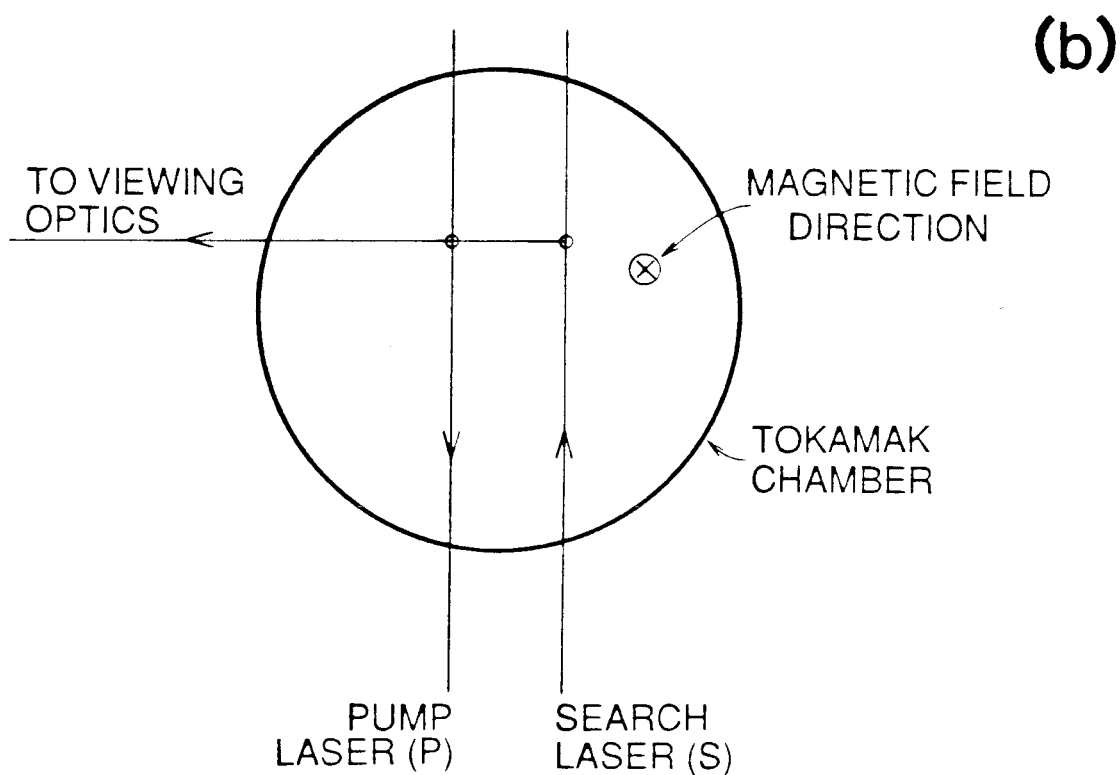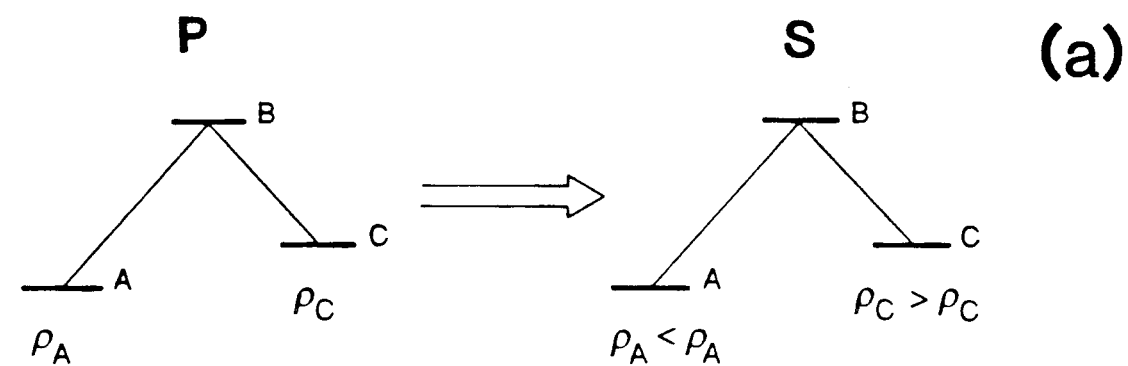
FIG. 3.7 (a) Principle of optical tagging. (b) Experimental configuration used in the optical tagging work.

target states concerned, and it is important to estimate the time for which ions remain "tagged." Electron excitation serves to return metastable populations to their steady state levels. To estimate the useful tagging lifetime consider the fluorescence scheme shown in Fig. 3.4(a). To perform optical tagging, we could deplete the population of $3d^2G_{9/2}$ ions by means of laser radiation tuned to the transition $3d^2G_{9/2} \to 4p^2F_{7/2}$. Because of the high transition probability for the transition $4p^2F_{7/2} \to 4s^2D_{5/2}$, many ions will end up in the $4s^2D_{5/2}$ state. We now consider the rate at which the reverse process can occur by means of electron-ion collisions. We use the results presented in the work of Book (1983). The cross section (Bethe approximation) for electron excitation by the dipole allowed transition m→n is given by

$$\sigma_{mn} = \frac{2.36 \times 10^{-13} f_{mn} g(n,m)}{\epsilon \Delta E_{mn}} \text{cm}^2, \qquad (3.9)$$

where $f_{mn}$ is the oscillator strength, $g(n,m)$ is the Gaunt factor, $\epsilon$ is the incident electron energy and $\Delta E_{nm} = E_n - E_m$. The electron excitation rate is then averaged over a Maxwellian velocity distribution to obtain

$$X_{mn} = n_e < \sigma_{mn}v > = \frac{1.6 \times 10^{-5} f_{mn} < g(n,m) > n_e}{\Delta E_{mn}\sqrt{T_e}} \exp\left(-\frac{\Delta E_{mn}}{T_e}\right) \text{s}^{-1}, \qquad (3.10)$$

where $< g(n,m) >$ is the thermally averaged Gaunt factor ($\sim 1$ for atoms and $\sim 0.2$ for ions). The oscillator strength for the transition $4s^2D_{5/2} \to 4p^2F_{7/2}$ is $f_{mn} = 0.387$ (Wiese et al. (1966)). Substituting reasonable values for the temperature and density (12eV and $10^{12}\text{cm}^{-3}$), we find $X_{mn} \sim 10^5\text{s}^{-1}$. Ions in the $4p^2F_{7/2}$ state will spontaneously de-excite (in $\sim$10ns) with significant numbers of ions returning

to the original $3d^2G_{9/2}$ state, thereby destroying the tagging effect. The electron excitation rate is the slowest step in this process and determines the effective time scale for the ions to become untagged. The anticipated time for which ions remain tagged is therefore $\sim 10\mu$s. The $3d^2G_{9/2}$ level is radiatively connected to several levels, and these will all contribute to the repopulation of this particular level and will further decrease the tagging lifetime by several microseconds. Since ion thermal velocities are only of the order of $1-2\times 10^5$cms$^{-1}$, it proved difficult to observe transport over distances greater than a 1-2cm.

The lifetimes of tagged states was experimentally measured and as estimated above, they were found to be 5-10$\mu$s. This was done by using a 1.2cm diameter pump beam and a 0.5cm diameter search beam. The two beams were coincident. The pump beam area was made much larger than the search beam area in order to minimize the effect of ion transport on the measurements. It was hoped that, since ion velocities were $1-2\times 10^5$cms$^{-1}$, relatively few untagged ions would have sufficient time to move into the search beam path before the search laser was fired. It is obvious that ions moving at the thermal velocity will move 1-2cm in a 10$\mu$s period; however, it was difficult to enlarge the pump beam diameter any further without lowering the beam intensity to the point where pumping of the target state was seriously compromised. In addition, the present port configuration limited the beam diameter to 1.2cm. "Dark signal" tagging was selected and the fluorescence scheme used is shown in Fig. 3.4(a). The metastable state used was of course the target state ($3d^2G_{7/2}$). A high power, flashlamp-pumped dye laser was used as the pump laser, while the CVL pumped dye laser was used as the search laser. Tagged state lifetimes were measured for two different plasma discharges. The parameters

for these discharges are shown in Table 3.1. Ion temperatures were determined using LIF, while the electron temperatures and densities were determined using Langmuir probes. The results of the tagging measurements are shown in Fig. 3.8, the boxcar averaged, search beam fluorescence signal is normalized to the peak fluorescence and plotted as a function of the time interval seperating the two laser pulses. For discharge 1, the tagged lifetime was about $5\mu$s and for discharge 2, the lifetime was about $10\mu$s. Since the ion thermal velocity goes as the square root of the ion temperature, ion velocities were similar for both the above discharges, so transport effects are evidently not responsible for the different tagging lifetimes. Within the limits of experimental error, electron temperatures were identical for both discharges, and temperature differences could not have caused the lifetime differences. On the other hand, the electron density for discharge 2 was twice that for discharge 1, and from Eq. 3.10 it is obvious that increasing electron density will increase the electron excitation rate and thereby reduce the lifetime of the tagged state.

## 3.6.3 OBSERVATION OF ION GYROMOTION USING TAGGING

Optical tagging can be used to perform velocity selection perpendicular to the direction of the probing laser beams. If two pulsed laser beams are spatially separated by a distance $d$ much greater than their diameters and are temporally separated by a period $t$ much longer than their duration, then only those ions moving from the pump beam to the search beam with an average velocity of $d/t$ will contribute to the reduction or enhancement of the search beam fluorescence. If we assume that the ions perform perfect gyromotion, i.e. their orbits are perfectly circular or helical, then only a small subclass of ions can interact with both beams.

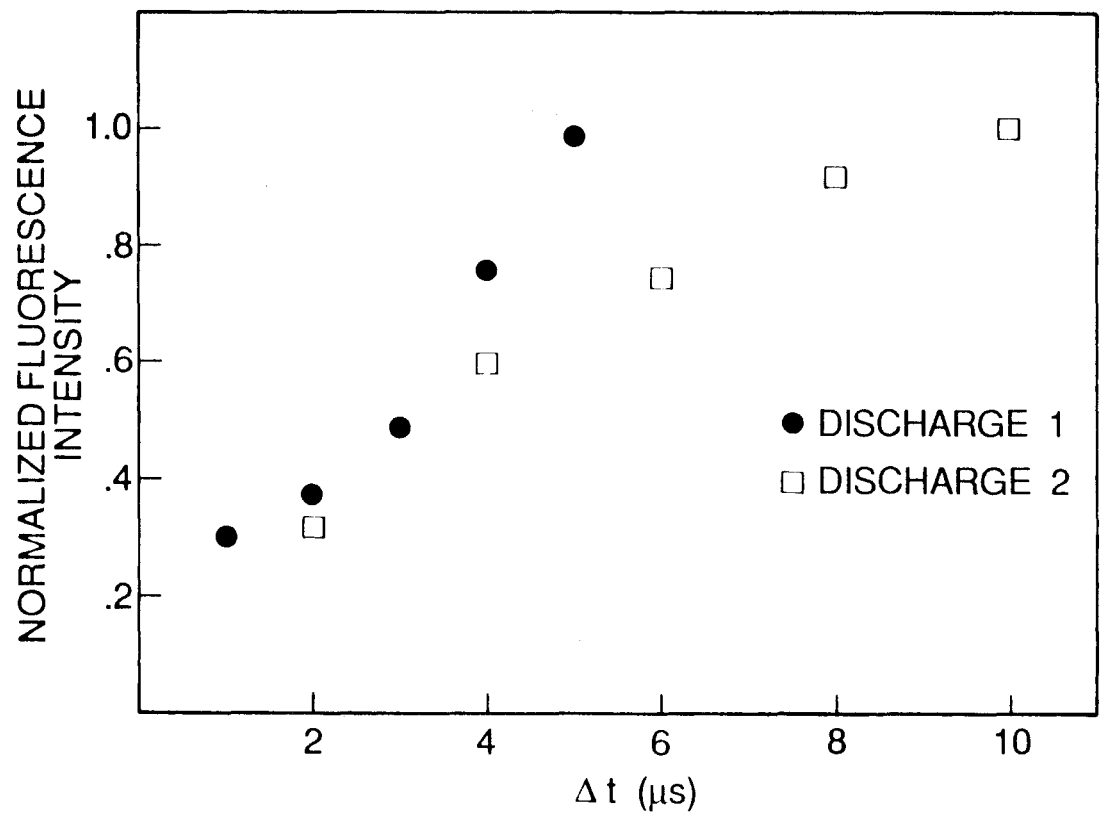| Discharge | $T_i$ (eV) | $T_e$ (eV) | $n$ (cm$^{-3}$) |
|-----------|-----------|-----------|-----------------|
| 1 | 1.47 | 8.06 | $1.02 \times 10^{12}$ |
| 2 | 1.05 | 7.93 | $4.90 \times 10^{11}$. |

Table 3.1 Parameters for lifetime measurements.

FIG. 3.8 Results of measurements to determine lifetimes of tagged states. The "S" beam fluorescence has been normalized to its value when no "P" beam is present. Δt is the temporal separation between the "P" and "S" beams.

Such ions must possess a both a perpendicular velocity ($v_\perp$) and an initial phase ($\phi_0$) that satisfy the relation,

$$d = \frac{v_\perp}{\omega_{ci}}[\sin(\omega_{ci}t + \phi_0) - \sin(\phi_0)]. \tag{3.11}$$

Refer to Fig. 3.9(a) for the geometry involved in this problem.

If the search beam is narrowband, it may be scanned to perform velocity selection parallel to the beam direction. The only tagged ions that can now interact resonantly with the beam are those whose y-components of velocity are given by $v_y = v_\perp\sin(\omega_{ci}t + \phi_0)$, where $v_\perp$ and $\phi_0$ satisfy Eq. 3.11. Assuming that the initial phase $\phi_0$ is completely random and that the ions assume a Maxwellian distribution, it was possible to calculate the lineshape of the tagged ion velocity distribution. This is shown in Fig. 3.9(b). Also plotted in this figure is the Maxwellian ion distribution used to derive the tagged function. The resulting distribution is no longer Maxwellian and its peak has been shifted away from zero. Reversing the direction of gyrorotation will clearly reverse the direction of this shift. To obtain the data shown in Fig. 3.9(b), the following parameters were assumed: $d$=0.5cm, $t = 3\mu$s, $B_0$=1400G and $T_i$=1.5eV. These parameters corresponded to those used in the actual experiment.

To scan only the tagged ions, the following procedure was adopted. The "S" laser was scanned across the Doppler-broadened line on a shot-to-shot basis but the "P" laser was fired only every alternate "S" laser shot. In this manner, it was possible to obtain simultaneously the usual Doppler-broadened distribution function and the distribution function that contains the tagged component. By subtracting these, it was possible to obtain the distribution function for the tagged component
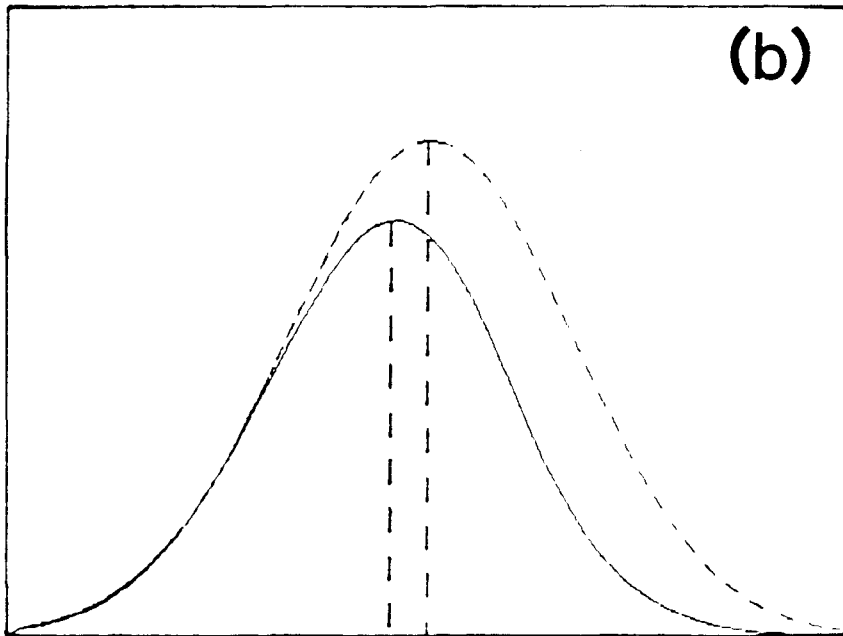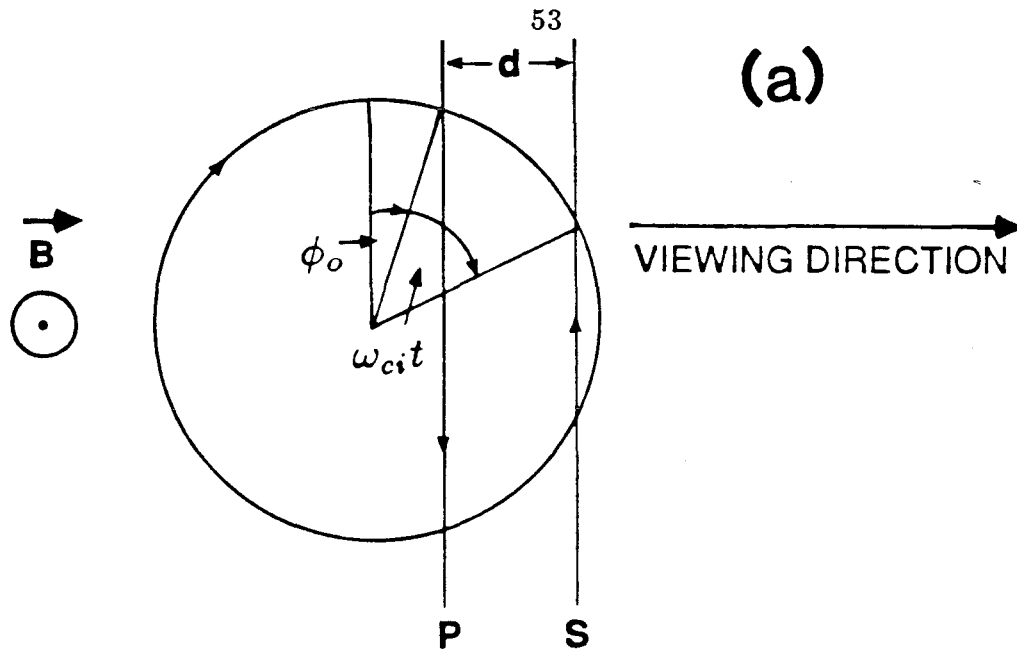
FIG. 3.9 (a) Geometry of the experiment to show gyro-
rotation, showing "P" and "S" beams and Larmor orbit of
an arbitrary 1.5eV ion. (b) Calculated lineshapes for
normal Doppler-broadened line (dashed line) and for tag-
ged ion component (solid line).

alone. This experiment was then repeated with the toroidal magnetic field reversed. The results are shown in Fig. 3.10. The tagged distributions are definitely shifted relative to the untagged Maxwellian, and the direction of this shift depends on the direction of the toroidal field. It is evident from Fig. 3.10 that the distribution functions of the tagged ions were non-Maxwellian but the quality of the data was not good enough to allow for further speculation regarding the actual lineshape.

## 3.7 ANOMALOUS ION HEATING IN ENCORE

The plasma in Encore is ohmically heated by means of a toroidally directed plasma current. The ohmic heating process involves the rapid heating of the electrons, followed by the heating of the ions on a time scale slower by a factor of $m_i/m_e$ ($\approx 10^5$ for argon ions). The classical time for equilibration between electron and ion temperatures is given by Trubnikov (1965),

$$\tau_{ie}^E = \frac{3\sqrt{2\pi}\pi\epsilon_0^2(m_i\kappa T_e + m_e\kappa T_i)^{3/2}}{Z^2\sqrt{m_e m_i}n\lambda_{ie}e^4},$$ (3.12)

where the symbols have their usual meanings. For parameters relevant to Encore, $\tau_{ie}^E \simeq 20 - 50\text{ms}$. Figure 3.11(a) shows a sequence of ion distribution functions recorded during the first $500\mu s$ of an Encore discharge. The data were taken at the center of the plasma. Plotted in Fig. 3.11(b) are ion temperatures $T_i$ determined from gaussian fits to these distribution functions, normalized to the electron temperature $T_e$ determined from Langmuir probe measurements. The surprising feature of Fig. 3.11(b) is that the observed rates of ion heating far exceed those predicted by Eq. 3.12. Ion temperatures reach $\sim 4\text{eV}$ within 100-200$\mu$s giving a
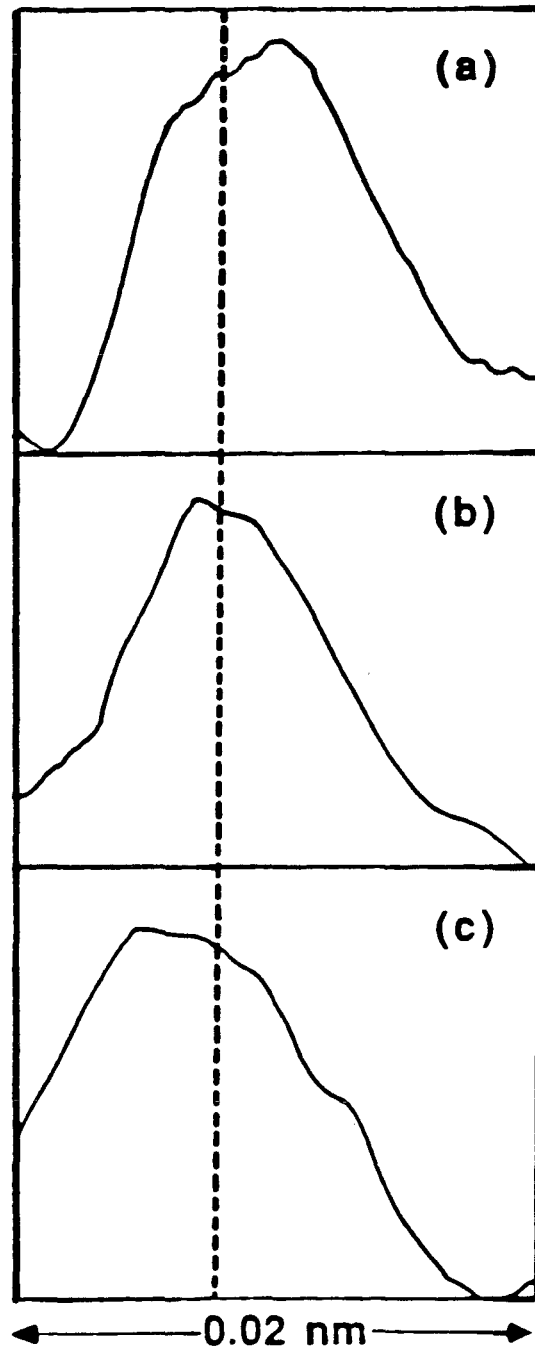
FIG. 3.10  Measured ion distribution functions. (a) Lineshape of tagged component. (b) Lineshape of normal Doppler-broadened line. (c) Lineshape of tagged component with magnetic field reversed.
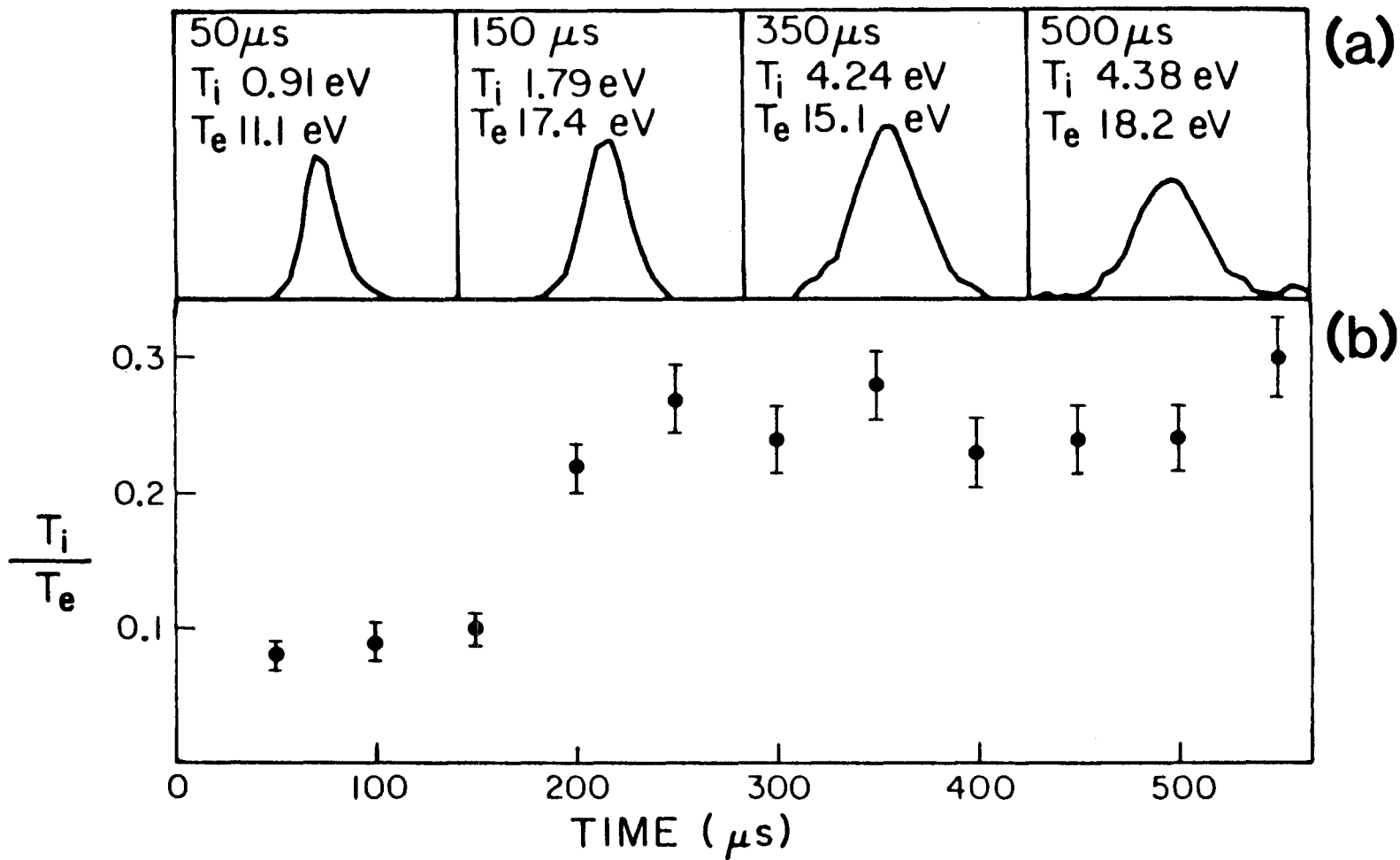
FIG. 3.11 Experimental demonstration of fast ion heating in Encore. (a) Series of measured ion distribution functions. (b) $T_i/T_e$ as a function of time for the first 550 s of the discharge.

heating rate of about $2 - 4 \times 10^4 eVs^{-1}$. For the electron temperature and density relevant to this discharge, a heating rate of about $350eVs^{-1}$ is predicted from Eq. 3.12. Such a heating rate implies that the ratio $T_i/T_e$ should never exceed 0.5% during the first $200\mu s$ of the discharge. As will be shown in the next chapter, none of the usual ion heating mechanisms is able to explain the observed ion heating.

Another noteworthy observation from Fig. 3.11(b) is that the ion temperature levels off after rising for about $100\mu s$. If collisional energy transfer from the hot electrons were the dominant heating mechanism, then a steady rise in ion temperature would be expected. It is probable that, after reaching a few electron volts, the ion confinement limit is reached since $r_{Li} \approx r_p$ (where $r_p$ is the plasma radius). However, this levelling off is also suggestive of the total decoupling between ion and electron temperatures.

# CHAPTER 4

# THEORETICAL BACKGROUND

## 4.1 PARTICLE HEATING MECHANISMS

Particle heating (as with all transport phenomena) requires that particle motion be irreversible. In a non-turbulent plasma, it is evident that there exist only three means to ensure irreversibilty: collisions, resonant wave particle interactions and intrinsic stochasticity. Collisions are the chief mechanism in low temperature or dense plasmas, but collisions cannot increase the aggregate energy of the colliding particles. Resonant wave-particle interactions lead to irreversibility and can also increase the aggregate particle energy (at the expense of wave energy). However, they do not heat the plasma bulk and require collisions to transfer energy from the resonant particles to the bulk. As will be seen, stochastic heating mechanisms can lead to the irreversible transfer of energy to the bulk plasma particles. At the end of Chap. 3, it was shown that the the ion heating rate in Encore was about $2 - 4 \times 10^4 \mathrm{eVs}^{-1}$. Heating by collisions and resonant interactions will be considered and shown to be insufficient to explain the high ion heating rates observed.

First, consider direct heating by the toroidal electric field $E$. The ion and electron drift velocities $u_i$, $u_e$ that are due to $E$ are determined by

$$m_i \frac{du_i}{dt} = eE - \frac{m_i(u_i - u_e)}{\tau_{ie}}, \tag{4.1}$$

$$m_e \frac{du_e}{dt} = -eE - \frac{m_e(u_e - u_i)}{\tau_{ei}}, \tag{4.2}$$

where total momentum conservation gives $m_i u_i + m_e u_e = 0$ and $\tau_{ei} m_i = \tau_{ie} m_e$. The steady-state drift velocities are $u_e = -eE\tau_{ei}/m_e$ and $u_i = eE\tau_{ie}/m_i \simeq 1200$cm s$^{-1}$ with $\tau_{ei} = 3.5 \times 10^5 T_e^{3/2}/n\lambda \simeq 1\mu$s, where $n \simeq 10^{12}$cm$^{-3}$, the Spitzer $\lambda \simeq 15$ and $T_e \simeq 12$eV. Frictional drag of ions on electrons will give ion heating. The frictional ion heating rate is

$$\frac{dT_i}{dt} = \frac{eE^2\tau_{ei}}{m_i} \simeq 60\text{eVs}^{-1}. \tag{4.3}$$

Similarly, the drag that is due to neutrals is, $(\sigma_{neut}n_{neut}u_i)m_i u_i$ giving

$$\frac{dT_i}{dt} \simeq \frac{\sigma_{neut}n_{neut}u_i^3 m_i}{e} \simeq 4 \times 10^{-4}\text{eVs}^{-1}, \tag{4.4}$$

with $\sigma_{neut} \simeq 5 \times 10^{-15}$cms$^{-1}$ and $n_{neut} \simeq 10^{12}$cm$^{-3}$. Clearly, direct heating by the toroidal electric field is insufficient. It is also clear that ions cannot drag on themselves. Therefore, even though ion-ion collision times may be as short as $50\mu$s ion-ion collisions cannot directly contribute to heating.

In ohmically heated discharges, the electrons are rapidly heated, while ions are heated more slowly by collisional energy exhange with the hot electrons. Electrons can heat up to 10-15eV very quickly,

$$\frac{dT_e}{dt} = \frac{eE^2\tau_{ei}}{m_e} \simeq 4.5 \times 10^6\text{eVs}^{-1}, \tag{4.5}$$

and will then transfer energy to the ions at a rate of

$$\frac{dT_i}{dt} = \frac{T_e}{\tau_{ie}^E} \simeq 350\text{eVs}^{-1}, \tag{4.6}$$

where $\tau_{ie}^E = m_i/3m_e \simeq 35\text{ms}$. This mechanism is also wholly insufficient to account for the observed ion heating rate of $\sim 4 \times 10^4 \text{eVs}^{-1}$.

Several electrostatic instabilities have been observed to cause ion heating in other devices. These include the ion cyclotron instability (Dakin, et al., 1976) and the ion acoustic instability (Mah, et al., 1970). The only instability of significant amplitude observed in Encore is the drift-Alfvén instability. This mode has been studied extensively by Fredricksen and Bellan (1985) and it will be shown that it is responsible for the observed ion heating. Earlier plasma simulation studies (Cheng and Okuda, 1978) have shown that low-frequency drift waves can cause significant ion heating. Hatakeyama et al. (1980) have observed ion heating by current-driven, collisionless drift waves in a Q-machine but didn't specify the actual heating mechanism. Also, Skiff et al. (1987) have observed stochastic ion heating by neutralized ion Bernstein waves. Also relevant is the theoretical work of Drake and Lee (1981), who discuss the stochastic heating of electrons by low-frequency lower hybrid drift waves.

## 4.2 DRIFT-ALFVÉN WAVES

### 4.2.1 INTRODUCTION

Drift waves are microinstabilities driven by the free energy available in the density ($\nabla n$) and temperature ($\nabla T$) gradients found in all laboratory plasmas. They propagate almost perpendicular to the magnetic field and to these gradients. This perpendicular propagation is in the direction of the electron diamagnetic drift, and the phase velocity is approximately the diamagnetic drift velocity. Drift waves also propagate parallel to the magnetic field and possess a very long parallel wavelength.

According to the linear theory, the driving mechanism for these waves depends on the existence of phase difference between the wave electric field and the plasma density fluctuations. In collisional plasmas electron-ion collisions are responsible for this phase shift. In collisionless plasmas this phase difference is introduced by means of Landau damping of resonant electrons or by the presence of an electron drift parallel to the magnetic field. The mechanism for stabilization according to linear theory is provided by ion Landau damping in the collisionless regime and by finite Larmor radius effects and ion-ion collisions in the collisional regime.

To determine whether drift waves are collisional or not, it is necessary to compare the relative effects of collisional and electron Landau damping. When the electron mean free path is shorter than the $k_z^{-1} \simeq qR$ where $q$ is the safety factor and $R$ is the major radius, then the electron Landau damping becomes less important than the collisional damping, and the waves are collisional. This condition may be written as $\nu_{ei}qR/v_e > 1$. Conversely, when $\nu_{ei}qR/v_e < 1$, the drift waves are collisionless. For typical Encore parameters ($q \sim 2$, $R$=38.1cm, $v_e = 1.5 \times 10^8$cms$^{-1}$, $\nu_{ei} = 8.4 \times 10^5$s$^{-1}$) $\nu_{ei}qR/v_e \sim 0.4$ and the drift waves are apparently in the collisionless regime. In order to determine whether or not the axial current has a significant destabilizing effect, it is necessary to look at the growth rate of the instability in detail. Examination of the dispersion relation for current driven collisionless drift waves gives the following relations for the frequency and growth rate (Bellan, private communication):

$$\omega_r = \frac{\omega_e^*}{1 + k_y^2 \rho_s^2} \tag{4.7}$$

$$\omega_i = \frac{\sqrt{\pi}\omega^2}{k_z v_e (1 + k_y^2 \rho_s^2)} \left[ k_y^2 \rho_s^2 + \frac{k_z v_0}{\omega} \right], \qquad (4.8)$$

where

$$\rho_s = \frac{c_s}{\omega_{ci}} \qquad \omega_e^* = -\frac{k_y T_e}{m_e \omega_{ce}} \frac{d\ln n}{dx},$$

and where $v_0$ is the parallel, electron drift velocity. The first term in brackets in Eq. 4.8 represents the contribution of Landau damping to the growth rate, while the second term represents the contribution of the axial current. Typical parameters for Encore are: $k_z \simeq (qR)^{-1} \sim 0.013 \text{cm}^{-1}$; $k_y = m/r \sim 0.25 \text{cm}^{-1}$; $v_0 \sim 3 \times 10^7 \text{cms}^{-1}$; $\rho_s \sim 5 \text{cm}$. Inserting these values into the expression for the growth rate, we find that the current driven term is about an order of magnitude larger than the Landau damping term and that the drift waves are strongly current-driven. In our experimental work it was possible to obtain modes that were saturated but coherent, and to control the amplitude of these modes by carefully altering the destabilizing plasma current. In the saturated state we assume that the mode amplitude is proportional to the growth rate which, in turn, was proportional to the electron drift velocity $v_0$. In very low current operation (plasma currents less than 100A), we could stabilize the drift waves in Encore at very low or negligible amplitudes.

## 4.2.2 DRIFT-ALFVÉN WAVES

Mikhailovskii and Rudakov (1963) predicted the existence of drift waves having substantial magnetic fluctuations in plasmas for which $\beta > m_e/m_i$, where ($\beta = 8\pi n T_e/B^2$). When the parallel phase velocity of the electrostatic drift wave

becomes comparable to the Alfvén velocity ($\omega/k_z \sim v_A$), the magnetic field becomes perturbed and the electric field can no longer be considered curl-free, and this effect must be considered when calculating the drift wave dispersion relation. A derivation of the drift-Alfvén dispersion relation is given in Appendix B. In this derivation the "bending" of the field lines is taken into account by introducing a longitudinal potential $\psi$ such that $E_z = -\partial \psi / \partial z$. Incidentally, the magnetic component of these waves is not important to the present work and will be ignored when describing the actual ion heating mechanism.

## 4.2.3 OBSERVATIONS OF DRIFT-ALFVÉN WAVES IN ENCORE

The modes observed in Encore may be coherent or turbulent, depending on the plasma conditions. Figure 4.1 shows two ion saturation current traces obtained using a simple, cylindrical Langmuir probe. The probe was positioned at the edge of the plasma, where the relative density fluctuation levels are highest. These plots were taken with a toroidal magnetic field of 300G and plasma currents of 0.2kA and 2kA, respectively. For 0.2kA the mode was clearly highly coherent (with toroidal mode number n=1, poloidal mode number m=2 and frequency=5.0kHz), while for 2kA the drift modes were fairly turbulent. Figure 4.2 shows contour plots of density, electron temperature, space potential and vector potential the m=2 mode. The poloidal mode structure is clearly evident from the plots. These plots were made using cylindrical, tungsten Langmuir probes and magnetic loop probes (Fredrickson and Bellan, 1985). From the space potential plot it can be seen that the drift waves generate very large electric fields ($E_\perp = k_\perp \phi_0 \simeq 100\text{Vm}^{-1}$). Such fields are much larger than the toroidal electric field due to the ohmic heating transformer ($E_{\parallel} \simeq 5\text{Vm}^{-1}$). Mode structures other than m=2 were also observed, depending
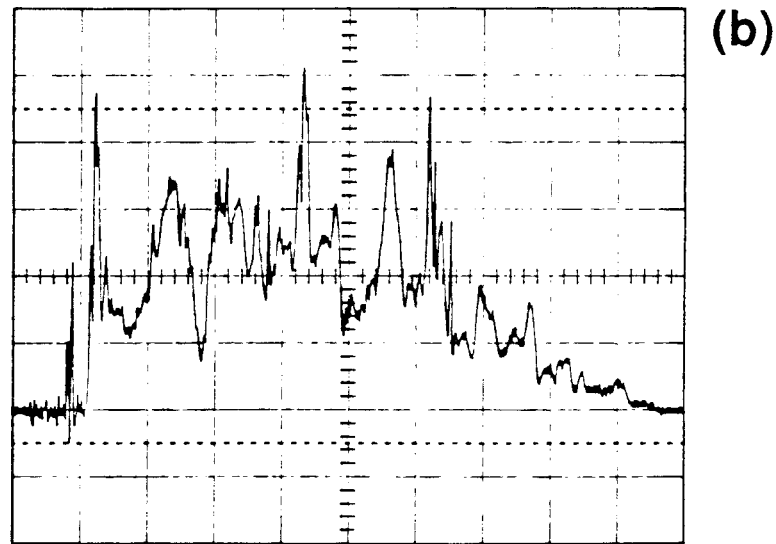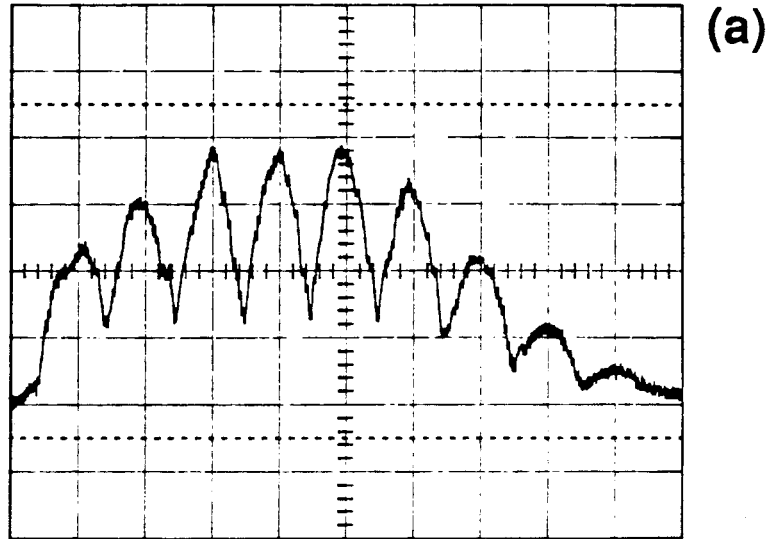
Hor. Scale 200 μs/div

FIG. 4.1  Ion saturation current traces showing, (a) coherent m=2 drift waves and (b) drift-wave turbulence.
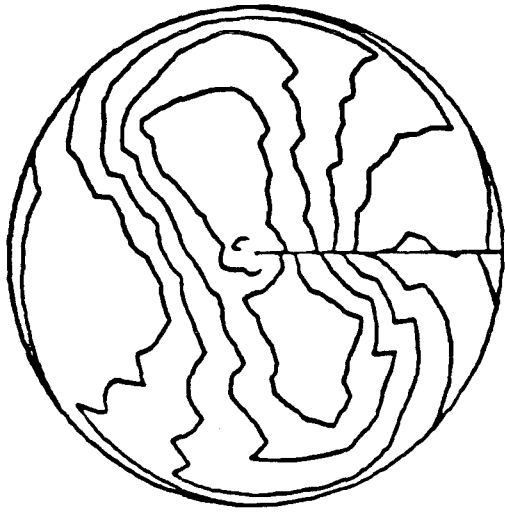
(a) Density (0.5·10$^{12}$/contour)
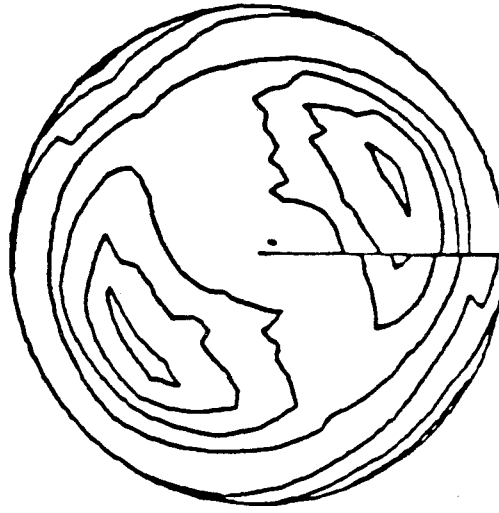
(b) Electron temperature (2.5 eV/contour)
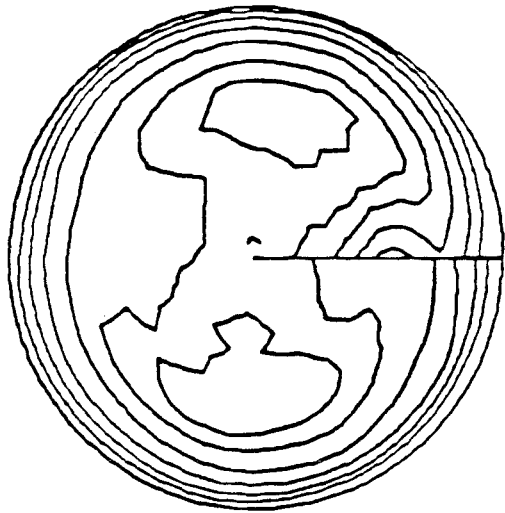
(c) Space potential (2.5 volts/contour)
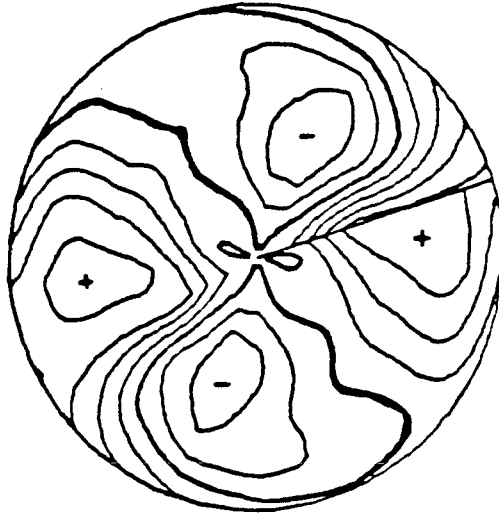
(d) Vector potential (1 statvolt/contour)

FIG. 4.2   Contour plots of (a) density, (b) electron tem-
perature, (c) space potential and (d) vector potential.
Plots are due to Fredrickson and Bellan (1985). The figures
are plotted so that 2π radians corresponds to twice the wave
period. Contour plots then approximate the mode structure.

on the toroidal magnetic field strength and the plasma current. It is noteworthy that anomalous ion heating was observed in all cases. Hence, turbulent heating is not the primary heating mechanism. Nor is the heating due to ion Landau damping of the drift-Alfvén mode. During the first $50\mu s$ of the discharge, $T_i \ll 1eV$, and the ion thermal velocity ($\sim 1 \times 10^5 cms^{-1}$) was much less than the drift wave, parallel phase velocity ($\sim 5 \times 10^6 cms^{-1}$). In the next sections of this chapter, it will be shown that the drift-Alfvén mode heated the ions stochastically.

## 4.3 STOCHASTIC ION MOTION IN A DRIFT-ALFVÉN WAVE

The importance of Hamiltonian stochasticity in classical systems has long been recognized. Several theoretical papers have predicted that the motion of a single magnetized ion may become stochastic in the field of an electrostatic wave (e.g., Smith and Kaufman, 1975; Fukuyama et al., 1977; Karney, 1978). Particularly pertinent to the present work was the study by Drake and Lee (1981) of stochastic ion heating of electrons by low-frequency lower hybrid drift waves. Although we didn't discover this work until near the end of the present study, it proved to be very useful in clarifying our ideas on stochastic heating by low-frequency modes. Experimentally, stochastic electron motion has been observed in a standing plasma wave by Doveil (1981). Skiff et al. (1987) have reported stochastic ion heating in the field of a neutralized ion Bernstein wave.

In a reference frame moving with the wave, the Hamiltonian of a particle is time-independent but in the laboratory frame, the Hamiltonian is time-dependent and the particle energy can increase. In the study of non-linear dynamics, the term "chaos" is used to describe the irregular, unpredictable behavior of deterministic

systems. Deterministic systems with a small number of degrees of freedom may exhibit behavior that is as statistically random as a system with many degrees of freedom. When particle motion becomes stochastic, small changes in the initial condition of the particle can result in radically different phase-space trajectories. Stochastic heating takes place when particle motion becomes sufficiently chaotic, so that large regions of phase space can be traversed by the particles. In Encore the cross-field ion motion that was due to the drift wave can become comparable to the drift wave perpendicular wavelength. Hence, an ion may rapidly traverse regions of widely varying phase of electric potential $\tilde{\phi}$, and in this way its motion can be randomized.

We investigate the conditions under which stochastic ion heating by drift waves can occur in Encore by considering a simple slab model of an ion moving in the potential of an electrostatic drift wave ($\theta \rightarrow y$, $r \rightarrow x$, $m/r \rightarrow k$). The fields are described by

$$\vec{E} = k\phi_0\hat{y}\cos(ky - \omega t), \quad \vec{B} = B_0\hat{z}. \tag{4.9}$$

The Lorentz equation describing the ion motion is

$$m_i\frac{d\vec{v}}{dt} = q(k\phi_0\hat{y}\cos(ky - \omega t) + \vec{v} \times B_0\hat{z}). \tag{4.10}$$

When $\omega \ll \omega_{ci}$, Eq. 4.10 is usually solved using the guiding-center approximation:

$$\vec{v} = \vec{v}_{larmor} + \vec{v}_{E \times B} + \vec{v}_{pol}, \tag{4.11}$$

where

$$\vec{v}_{pol} = \frac{\dot{\vec{E}}}{\omega_{ci}B_0}. \tag{4.12}$$

In this approximation it is assumed that $\dot{\vec{v}}_{pol} \ll \dot{\vec{v}}_{E \times B}$. Substituting the expression for the electric field into Eq. 4.12 and taking into account the dependence of $y$ on $t$ in the phase gives

$$\vec{v}_{pol} = v_y \hat{y} = \frac{\omega}{k} \frac{\alpha \sin(ky - \omega t)}{(1 + \alpha \sin(ky - \omega t))}, \tag{4.13}$$

where

$$\alpha = \frac{m_i k^2 \phi_0}{q B_0^2}, \tag{4.14}$$

The polarization drift is in the direction of the wave phase, whilst the $\vec{E} \times \vec{B}$ drift moves the ion perpendicular to the direction of phase propagation. From Eq. 4.14 we see that for $\alpha \sim 1$, the assumption that $\dot{\vec{v}}_{pol} \ll \dot{\vec{v}}_{E \times B}$ breaks down and the guiding- center approximation is no longer valid, and the ion motion must be calculated exactly. From Eq. 4.14, $\alpha \sim k\Delta y$, where $\Delta y$ is the ion displacement that is due to the polarization drift, so the condition $\alpha \sim 1$ means that the displacement that is due to the polarization drift becomes comparable to the drift wave perpendicular wavelength. It is also apparent that the above notions apply only to electrostatic modes where $\vec{E} \parallel \vec{k}$; hence, $\vec{v}_{pol} \parallel \vec{k}$ and the polarization drift is capable of pushing ions into regions of different wave phase. For purely electromagnetic waves, $\vec{E} \perp \vec{k}$ and the polarization drift cannot do this.

To perform the exact numerical calculations we first normalize lengths and times appropriately. Normalizing times to $\omega_{ci}^{-1}$, lengths to $k^{-1}$ and writing $\nu = \omega/\omega_{ci}$ Eq. 4.10 becomes

## 4.4 SURFACE OF SECTION PLOTS

For $\alpha > 0$, the ion motion becomes complicated and it is convenient to use Poincaré surface of section plots (Lichtenberg and Lieberman, 1983) in order to visualize the ion trajectory through the 3-D phase space. A surface of section is a means of visualizing in two dimensions the motion of a particle in a higher dimensional phase space. A surface of section is made by taking successive "slices" through the higher dimensional phase space. For the 3-D phase space considered here the "slice" was defined by $y = 0$.

Figure 4.3 shows a series of surface of section plots for $\nu=0.4767$ and for increasing values of $\alpha$. The different orbits shown in each plot represent different initial conditions $y$, $\dot{y}$ for the ion. Each test ion trajectory was followed for several hundred cyclotron periods allowing the surface of section to be penetrated several hundred times. For small values of $\alpha$, the orbits all lie on smooth curves and are integrable. For intermediate values of $\alpha$, some of the orbits may be stochastic, depending on the initial position. For $\alpha > 0.8$, however, essentially all orbits for $\dot{y} < 3$ are stochastic, and ions may be heated through the range of phase space $\dot{y} < 3$. Figure 4.4 shows an identical series of plots, except that $\nu=0.1234$. The behavior with increasing $\alpha$ is essentially the same, indicating similar stochastic thresholds for very low-frequency waves. The same behavior was observed for $\nu$ down to 0.05. Clearly, when $\nu = 0$, however, the Lorentz equation (Eq. 4.15) becomes integrable, and ion motion cannot become stochastic. It is important to note that although it takes several hundred cyclotron periods to build up a surface of section plot, the motion is actually randomized on a very much shorter time scale (1-2 cyclotron periods). We follow the motion for the longer period only to improve the plots.

FIG. 4.3  Surface of section plots in $(\dot{y}, y, \nu t)$ space defined by y=0. $\nu$=0.4767 and $\alpha$ increases from 0.2 to 1.0

FIG. 4.3(continued)

(e)

$\alpha = 0.8$

(f)

$\alpha = 1.0$
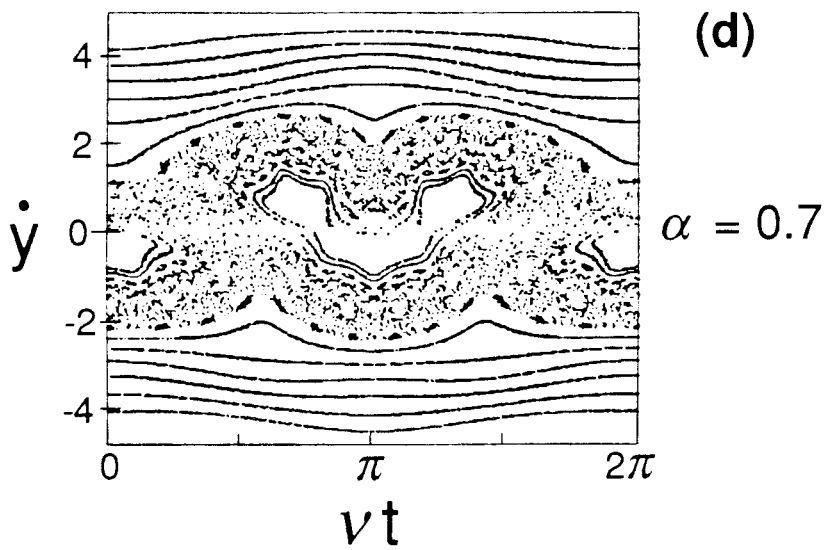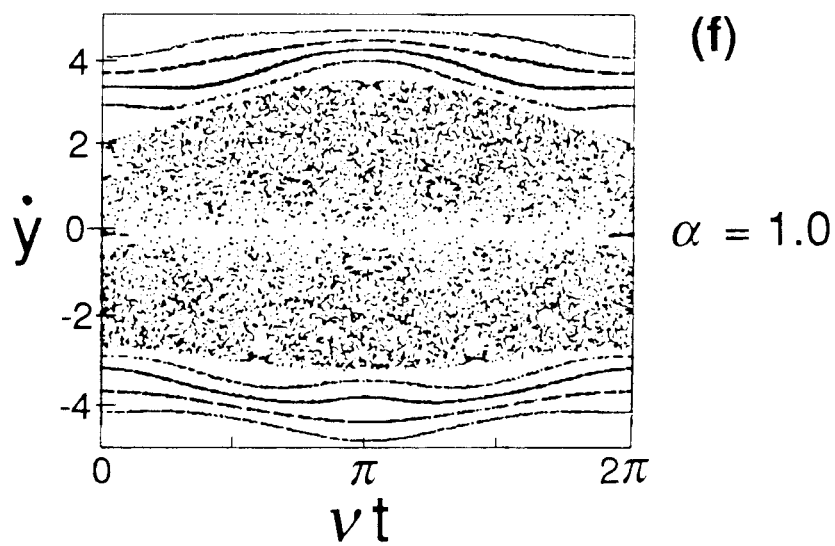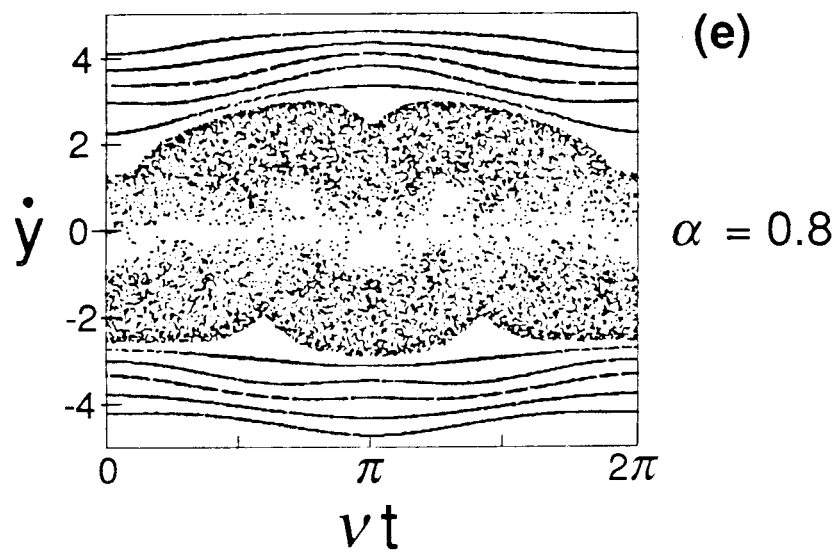
FIG. 4.3(continued)
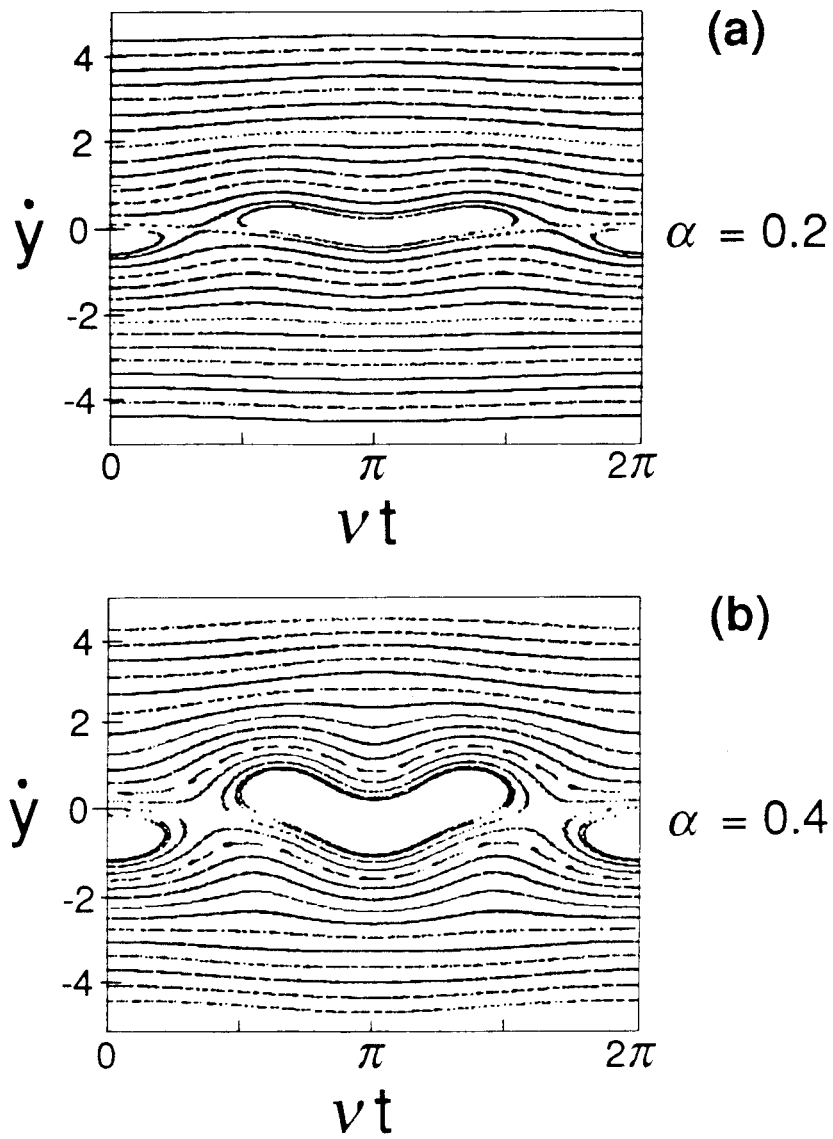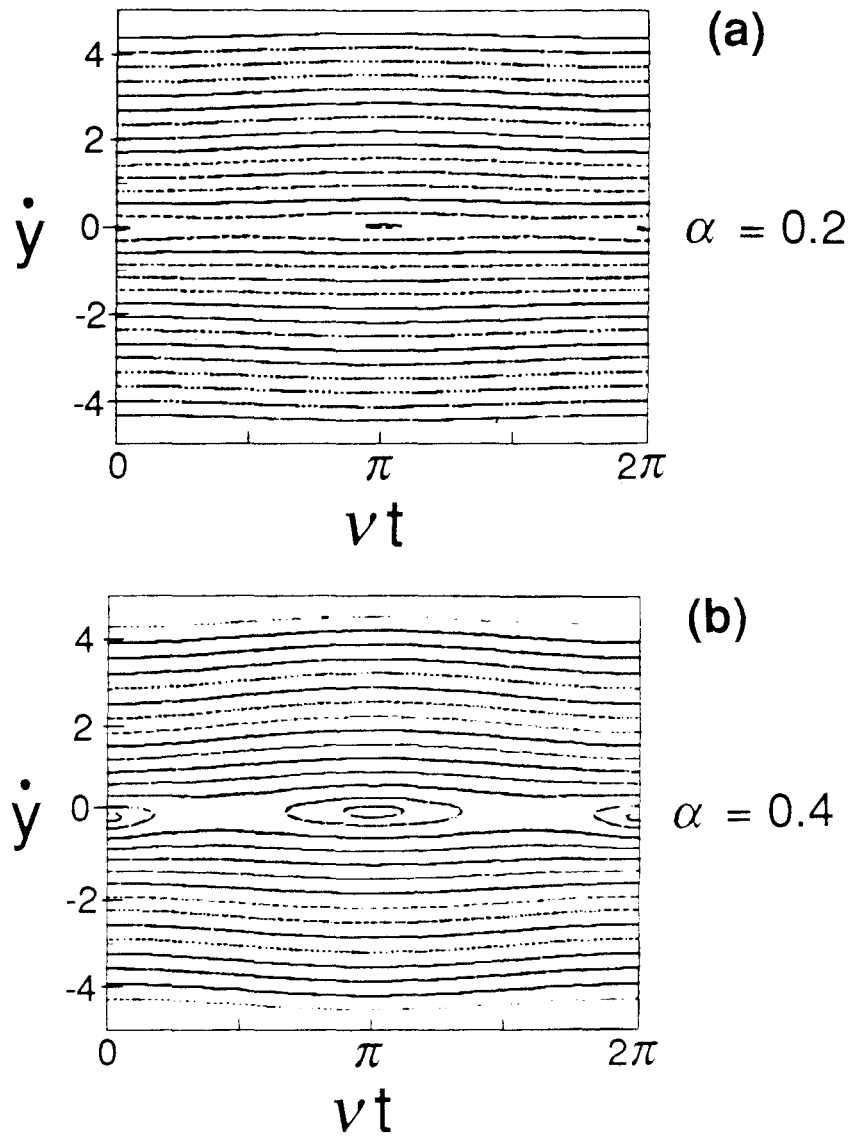
FIG. 4.4  Surface of section plots in $(\dot{y}, y, \nu t)$
space defined by y=0. $\nu$=0.1234 and $\alpha$ increases
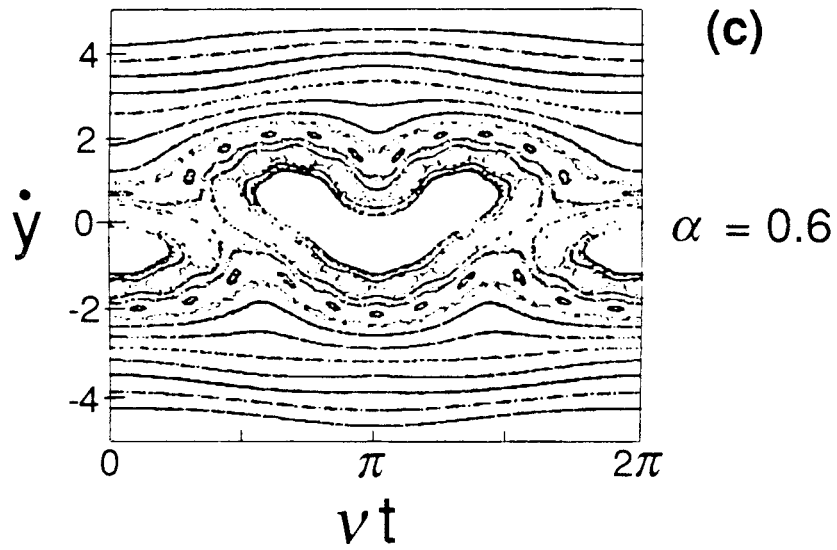from 0.2 to 1.0

(c)

$\alpha = 0.6$

$\dot{y}$

$\nu t$

(d)

$\alpha = 0.8$

$\dot{y}$

$\nu t$

FIG. 4.4(continued)

**(e)**

$\dot{y}$

$\alpha = 0.9$

$\nu t$

**(f)**

$\dot{y}$

$\alpha = 1.0$

$\nu t$
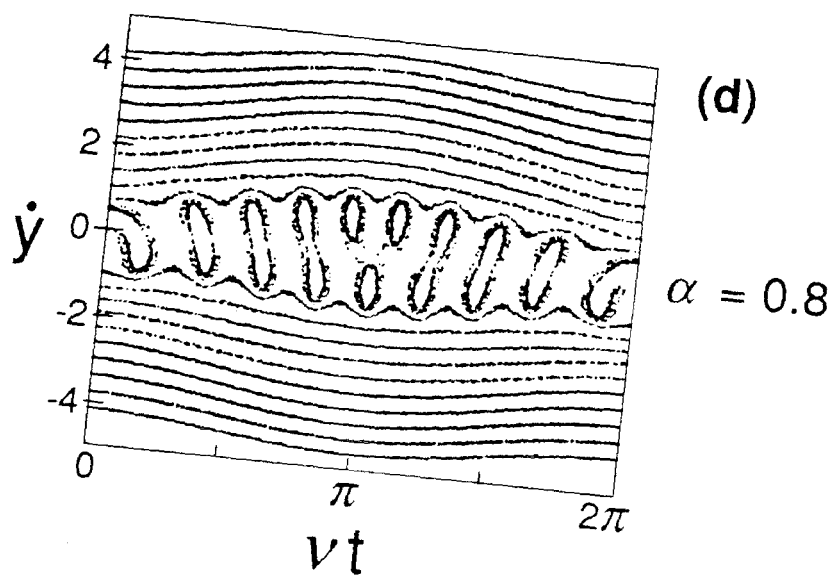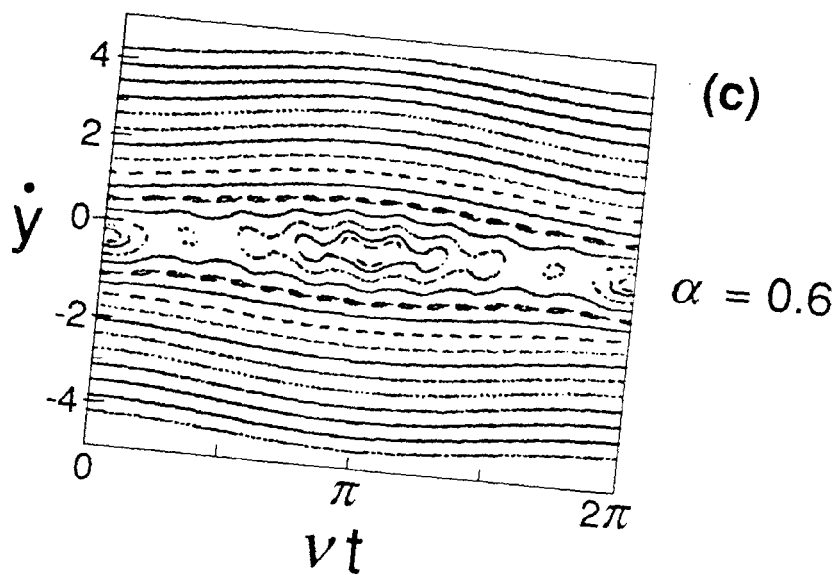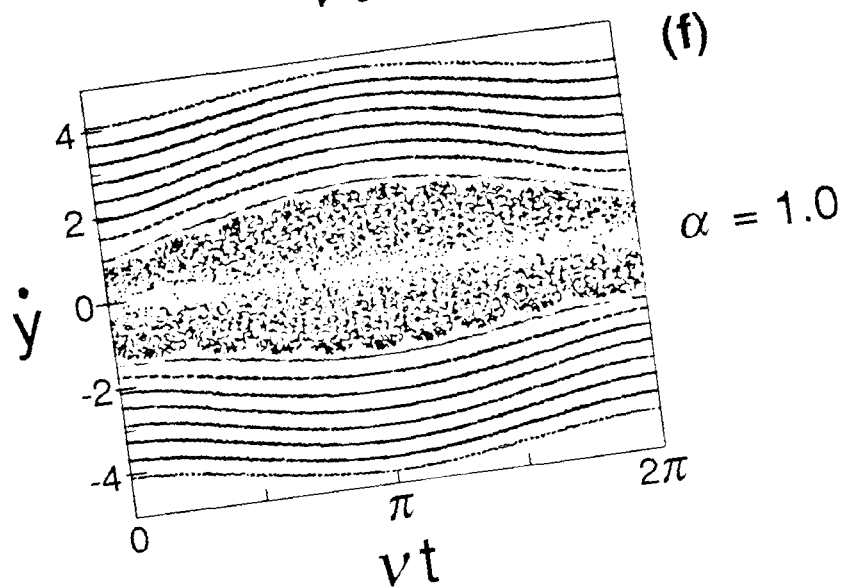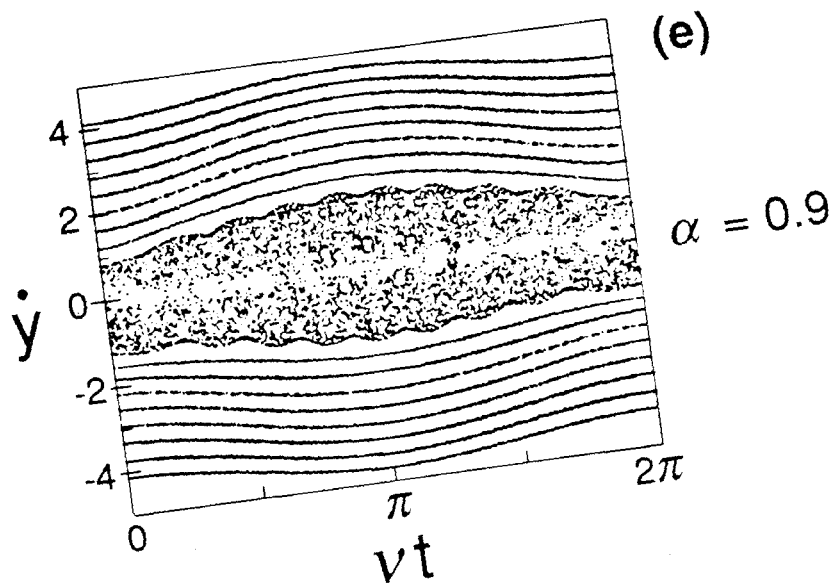
FIG. 4.4(continued)

From Fig. 4.3(f) it can be seen that stochastic ions may be accelerated to velocities of $\dot{y} > 3$. By constructing a series of surface of section plots for $\alpha > 0.8$, it was found that the stochasticity boundary is given by $\dot{y}_{max} \simeq \alpha + 2$, so that very large ion energies can be obtained by increasing the wave amplitude $\alpha$. In particular, ions can be accelerated to energies far in excess of the electrostatic potential energy of the "well" that is due to the drift mode. There is nothing surprising about this of course. When $\alpha > 0.8$, ion motion is not conservative and an ion is free to visit large regions of phase space and attain very high energies. The maximum velocity that an ion can attain in a stationary wave potential is $2q\phi_0$, giving $\dot{y}_{max} = 2\sqrt{\alpha}$. As a function of $\alpha$, the ratio of maximum stochastic energy to maximum non-stochastic ion energy is

$$\frac{H_{stochastic}}{H_{non-stochastic}} \simeq \frac{(\alpha + 2)^2}{4\alpha} \tag{4.18}.$$

Typically, for our experiments; $\omega/2\pi \sim 5\text{kHz}$, $k_\perp = m/r \sim 40\text{m}^{-1}$ ($m = 2$, $r = 0.05\text{m}$), $\phi_0 \sim 2\text{V}$ and $B_0 \sim 0.03\text{T}$ giving $\nu \sim 0.5$ and $\alpha \sim 1.5$, so that stochastic ion heating should occur. The above surface of section plots show a distinct threshold for stochastic behavior. Hence, below a drift wave amplitude corresponding to $\alpha \sim 0.8$, the ion heating rate should be very low. For $\alpha \sim 0.8$, the energy ratio given by Eq. 4.18 is $\sim 2.5$, so there should be significant numbers of ions having kinetic energies greater than the "well" potential energy.

## 4.5 PHYSICAL MECHANISM FOR STOCHASTIC MOTION

It is apparent that the stochastic behavior described above is due to the trapping and detrapping of ions in the periodic, potential troughs of the drift waves.

Discussions of particle trapping in the absence of a magnetic field may be found in any basic plasma physics text (e.g., Chen (1974)). Basically, a particle becomes trapped when its energy in the wave frame is smaller than the wave potential

$$2q\phi_0 > \frac{1}{2}m_p\left(v_p - \frac{\omega}{k}\right)^2. \tag{4.19}$$

This effect may be seen in the surface of section plots (Fig. 4.3(c)-(e)), where the central region is sparsely populated. After being detrapped, the ions move randomly in the presence of the fluctuating electric field. To trap particles near the peak of the distribution (near $v_p = 0$) would require a potential of

$$q\phi_0 > \frac{1}{4}m_p\left(\frac{\omega}{k}\right)^2. \tag{4.20}$$

When a strong magnetic field is present, this simple reasoning is inappropriate and the following arguments must be used.

The Hamiltonian describing ion motion (Eq. 4.17) can be rewritten as

$$h = \frac{1}{2}p_y^2 + \Phi, \tag{4.21}$$

where the effective potential $\Phi$ is defined by

$$\Phi = \frac{1}{2}(p_x + y)^2 - \alpha\sin(y - \nu t). \tag{4.22}$$

From Eq. 4.17 we see that $p_x = -(y - \dot{x})$ is the negative of the $y$ component of the guiding-center and without loss of generality may be taken to be zero giving.

$$\Phi = \frac{1}{2}y^2 - \alpha\sin(y - \nu t) \tag{4.23}$$

The first term in Eq. 4.23 represents the magnetic part of the effective potential, while the second term represents the electrostatic potential that is due to the drift wave. Equation 4.23 may be represented graphically, as shown in Fig. 4.5. The initial guiding-center position is $y=0$. If $T_i$ is the initial ion kinetic energy, then the ion Larmor radius is given by the intersection of the $T_i$ energy level with the parabola $y^2/2$. For convenience, the wave trough is assumed initially to be at the origin. As the wave travels from left to right, the ion is carried along by the wave until, $y \sim \alpha$, at which point the wave electric force equals the magnetic $\vec{v} \times \vec{B}_0$ force, and the ion will be untrapped. This point is clearly demonstrated in Fig. 4.5, where it is seen that when $\alpha \sim 10 \sim y$ the potential trough disappears. (The large value for $\alpha$ was selected to make this effect more obvious in the figure.) The time during which an ion will see a trough is (in unnormalized units) $\tau \sim y/\nu \sim \alpha/\omega$. Now for effective trapping to occur, it is necessary that $\tau > \tau_b$, where $\tau_b \ (= 2\pi\sqrt{m_i/4qk^2\phi_0})$ is the unmagnetized bounce period. The use of the unmagnetized bounce period is justified because $y < \alpha$ and the wave electric force dominates the magnetic force. This trapping condition requires

$$\frac{\omega}{\alpha} < \omega_b \Rightarrow q\phi_0 > \left(\frac{1}{4}\right)^{1/3} m_i \left(\frac{\omega}{k}\right)^2 \left(\frac{\omega_c}{\omega}\right)^{4/3}. \tag{4.24}$$

This condition is larger by a factor of $\sim (\omega_c/\omega)^{4/3}$ than the potential required for trapping in the absence of a magnetic field. Rearranging Eq. 4.24, the trapping condition may be rewritten as

$$\alpha > \left(\frac{1}{4}\right)^{1/3} \left(\frac{\omega}{\omega_{ci}}\right)^{4/3}, \tag{4.25}$$

i.e., somewhat less stringent than the condition for stochastic motion. For the
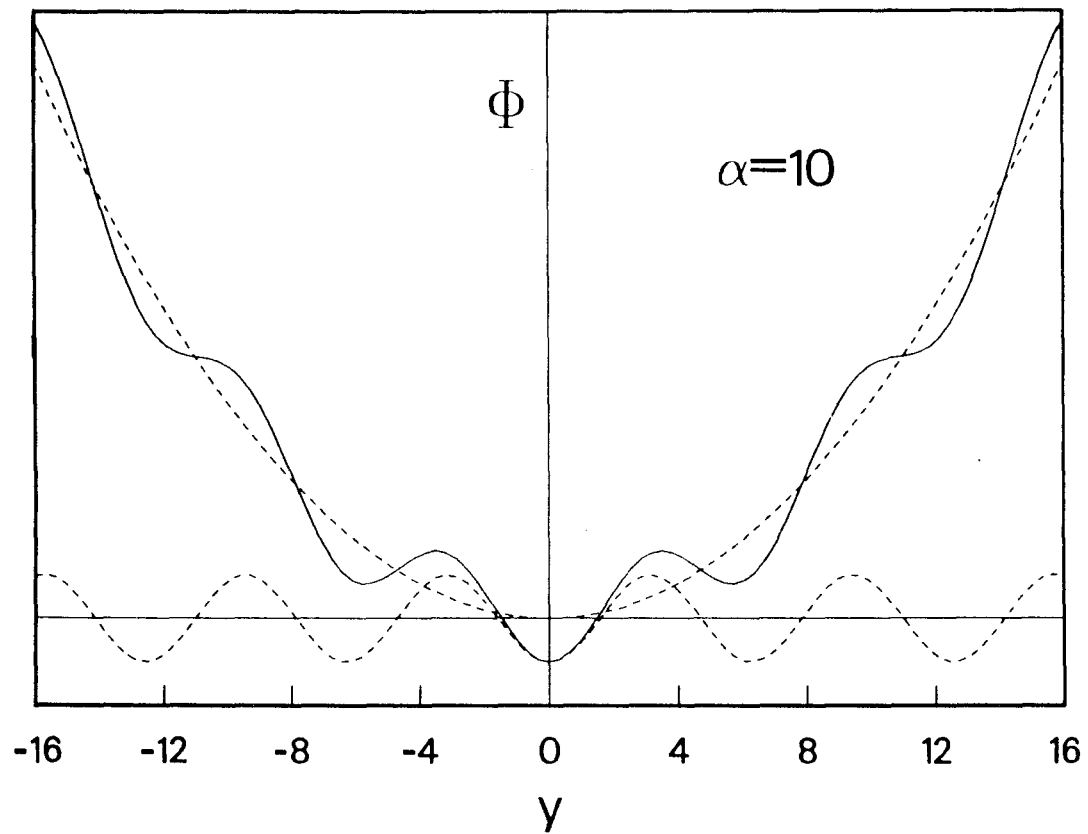
FIG. 4.5 Effective potential seen by an ion. The effective potential is the solid curve. The magnetic and electrostatic potentials are the dashed curves. The sinusoidal wave propagates from left to right.

parameters relevant to the present work, particle trapping will occur.

When an ion becomes trapped in the trough of the drift wave, it will be carried up the magnetic force potential until $y \sim \alpha$, where it will be released with an increased kinetic energy of $\sim \frac{1}{2}\alpha^2$. Most ions with energy less than $\frac{1}{2}\alpha^2$ will participate in this trapping/detrapping process. In unnormalized units, the effective ion temperature is given by

$$T_i \simeq m_i \left( \frac{k\phi_0}{B_0} \right)^2. \qquad (4.26)$$

In other words, the ion thermal velocity will be of the order of the $\vec{E} \times \vec{B}$ drift velocity.

At this point it is perhaps appropriate to emphasize the importance of the concept of intrinsic stochasticity. The conditions necessary for stochastic heating to occur are modest in the sense that any combination of electric and magnetic fields that predicts stochastic behavior theoretically will unquestionably yield stochastic behavior experimentally. I quote Chernikov et al. (1987): "Stochasticity has a number of amusing and interesting properties. We are accustomed to the fact that various solutions which are "good" in simple models, are spoiled when more complex models are adopted. The situation changes, however, in the region of stochastic dynamics. Further complications of the model lead to an increase in the phase volume occupied by the stochastic region. Hence to discover the condition for the onset of stochasticity, *it is sufficient to study the simplest situations.*" (My emphasis.) Hence, the simple model discussed above is in no sense academic; in fact, it yields necessary and sufficient conditions to ensure stochastic ion behavior.

## CHAPTER 5

## EXPERIMENTAL VERIFICATION OF STOCHASTIC ION HEATING

### 5.1 INTRODUCTION

In this chapter several pieces of evidence supporting stochastic acceleration of ions will be presented. Firstly, it will be shown that the heating occurs predominantly where the modes are present, i.e., at the plasma edge. Secondly, it will be shown that the observed ion heating displays the expected threshold with increasing mode amplitude. The mode electric potentials were obtained from Langmuir probe measurements. Next, we will examine the Landau damping of ion acoustic waves for increasing ion temperature. Below the threshold for ion heating where ion temperatures are low, Landau damping is seen to be fairly weak, while damping increases strongly when the ions are heated. This behavior is in accordance with well-known theoretical results. These results proved that true ion heating took place; i.e., the ion distribution functions observed represented a true spread in the ion thermal energy and were not merely an artifact of the measurement technique. It will then be shown that true ion heating is obtained, i.e., that the ion motion is completely non-conservative, by showing that some groups of ions that were initially cold, attain kinetic energies that exceed the maximum possible electrostatic potential energies. This was shown in two ways. One method was simply to measure the drift wave space potential amplitude by means of probes and then to search for high energy ions by means of a narrow band laser. The second method involved the use of the optical tagging diagnostic to detect energetic ions in the vicinity of the peak in the wave potential. Finally, a numerical simulation of ion heating in the field of

a prescribed electrostatic mode was performed in tokamak geometry and compared with experimentally observed ion temperatures and heating rates.

## 5.2 RADIAL VARIATION OF ION HEATING

The relative density fluctuation levels $(\tilde{n}/n)$ of drift-type instabilities are generally largest at the region of maximum density gradient (Fredrickson and Bellan, 1985), i.e., at the edge of the plasma. Hence, if drift-Alfvén waves do indeed cause anomalous ion heating, the highest heating rates would be expected to occur at the plasma edge. Such results were, in fact, observed. Figure 5.1 shows the time evolution of ion temperature at two different radial positions in the plasma. The open circles were taken at points in the center of the plasma, while the open triangles were taken towards the edge of the plasma $(r/a = 0.67)$. The ion heating rate at the edge is clearly higher than that at the center. This phenomenon was also observed by Hatakeyama et al. (1980), who looked at heating by drift waves in a Q-machine plasma. They, however, used electrostatic energy analyzers to measure ion temperatures and evidently did not elucidate the actual ion heating mechanism. It should be noted that because stochastic acceleration results in diffusion in both velocity and coordinate space, ion temperatures at the center are not zero and, in fact eventually come into equilibrium with those at the edge.

## 5.3 OBSERVATION OF THRESHOLD CONDITION

The surface of section plots shown in Chap. 4 indicate a fairly distinct threshold for stochastic heating with increasing mode amplitude. Below a drift wave amplitude corresponding to $\alpha \sim 0.8$, the ion heating rate should be low. This behavior was observed experimentally. Figure 5.2 shows the peak ion temperature
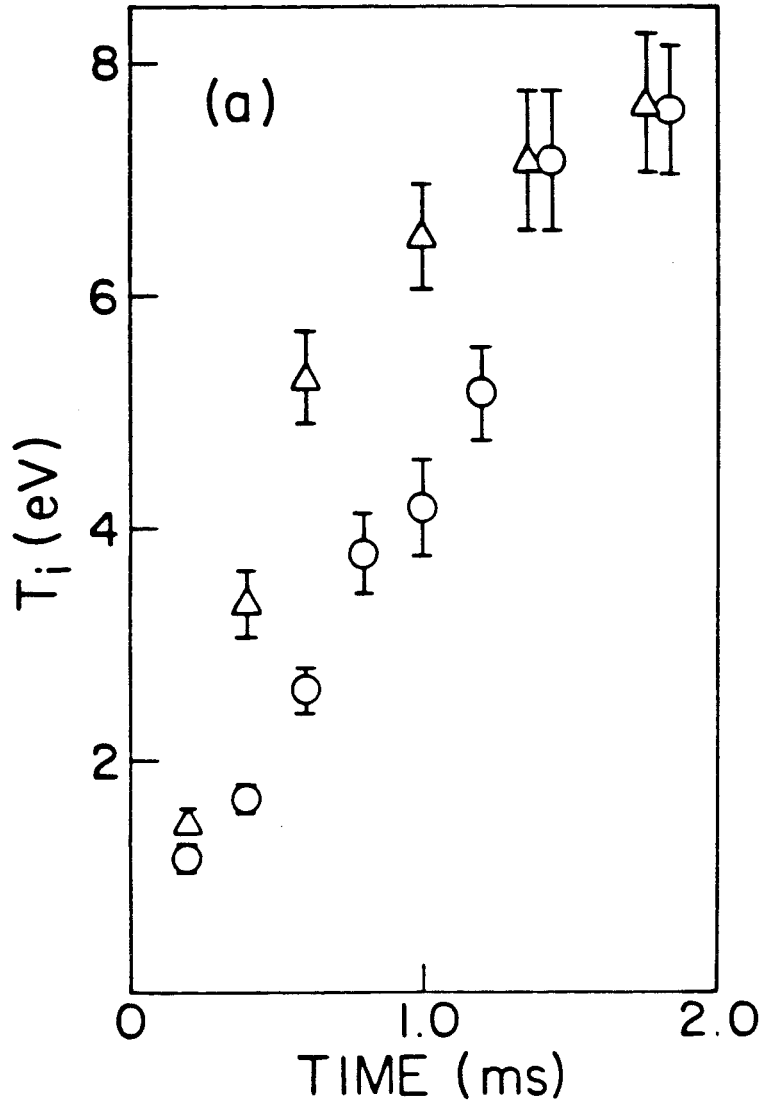
FIG. 5.1  Ion heating at r/a=0 (circles) and at r/a

r/a=0.67 (triangles) showing that the heating is strong-

est at the plasma edge where drift wave amplitudes

are highest.
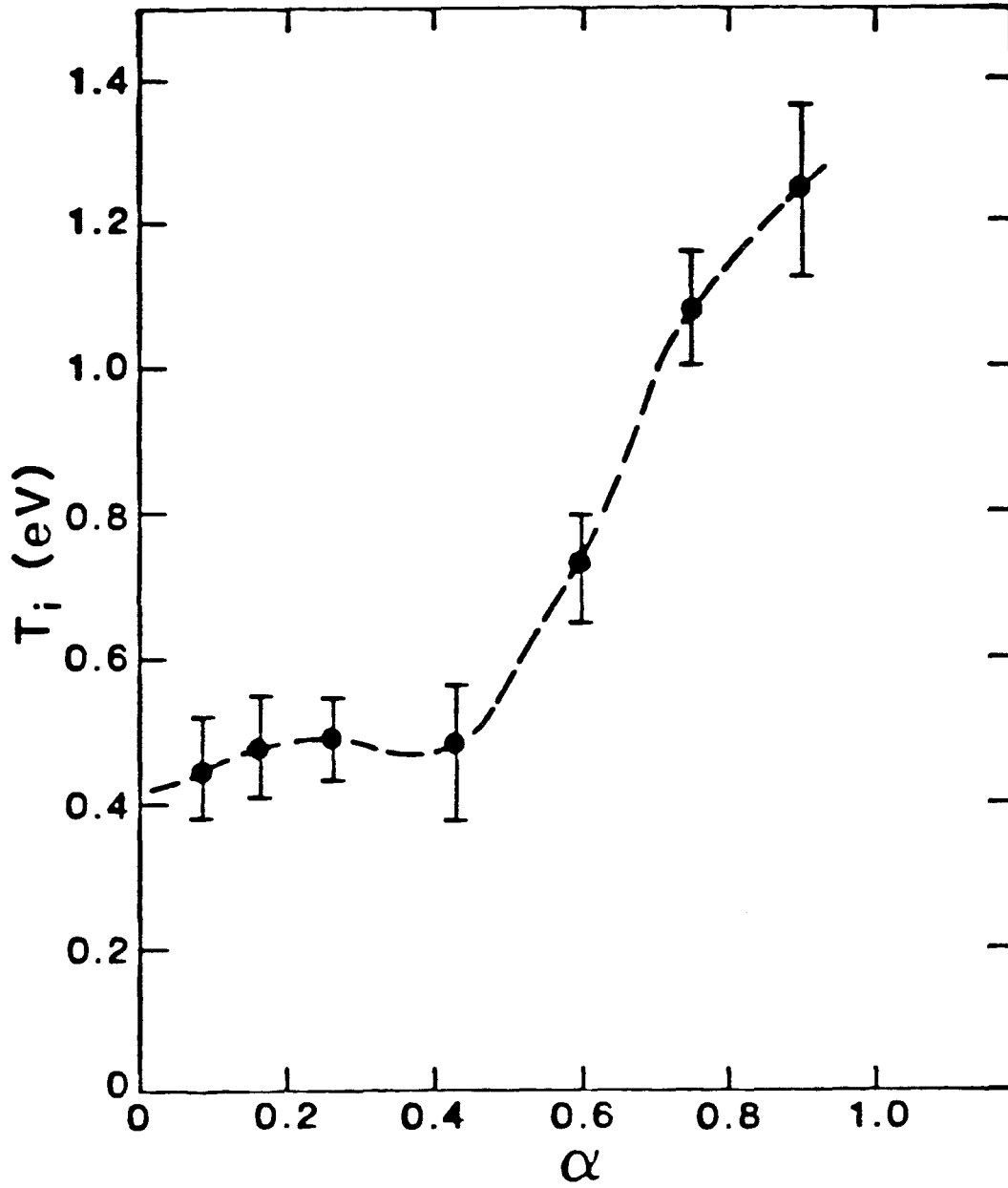
FIG. 5.2 Experimental values of the peak $T_i$ plotted
as a function of the normalized wave amplitude ($\alpha$).
The magnetic field was 300G.

during an Encore shot as a function of $\alpha$, where $\alpha$ was determined using measured values of the plasma space potential and known values of the magnetic field. For small $\alpha$, ion temperatures remained below 0.5eV. However, above $\alpha \sim 0.5$-0.6 peak ion temperatures nearly tripled. This behavior is precisely what would be expected from the theoretical analysis of the last chapter. The final ion temperature is in accord with Eq. 4.24. This equation may be rewritten as $T_i = \alpha^2 \phi_0$. For the last point on Fig. 5.2; $T_i = 1.25$eV, $\alpha = 0.9$, and $\phi_0 = 1.5$V. From Eq. 4.24 we estimate $T_i = 1.22$eV, a value very close to the measured value of 1.25eV.

## 5.4 LANDAU DAMPING OF ION ACOUSTIC WAVES

A number of attempts had been made to observe ion acoustic waves in the Encore device (Bellan, private communication) and these had failed. In the course of the present work it became evident that this failure was due to the unexpectedly high ion temperatures and hence low ratio of $T_e/T_i$ observed in the Encore device. As is well known, the Landau damping rate increases strongly with decreasing $T_e/T_i$. Gekelman and Stenzel (1975) give the following expresions for the ion acoustic wave frequency and the Landau damping constant.

$$k_r = \frac{\omega}{c_s} \qquad (5.1)$$

$$k_i = -k_r \sqrt{\frac{\pi}{8}} \left( \frac{T_e}{T_i} \right)^{3/2} \exp\left( -\frac{T_e}{T_i} + \sqrt{\frac{m_e}{m_i}} \right), \qquad (5.2)$$

where $c_s = \sqrt{\kappa T_e/m_i}$ is the ion sound speed. By running very low current plasmas where the drift waves were not destabilized and strong ion heating was absent, it
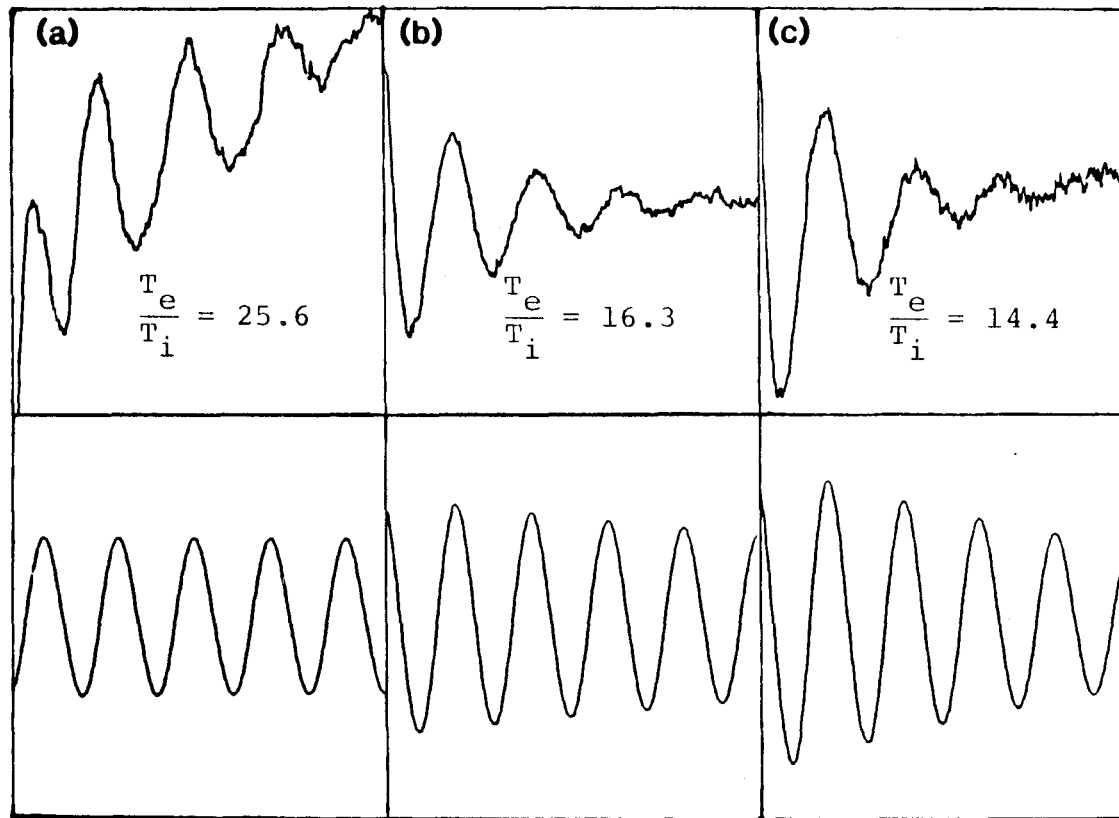
FIG. 5.3  Interferometer traces of Landau-damped ion acoustic waves showing the effect of increasing $T_e/T_i$. The top traces are experimental data. The lower traces are theoretical plots obtained using measured values of $T_e/T_i$.

(d) $\frac{T_e}{T_i} = 11.8$

(e) $\frac{T_e}{T_i} = 10.1$

(f) $\frac{T_e}{T_i} = 7.6$

FIG. 5.3 (continued)

88
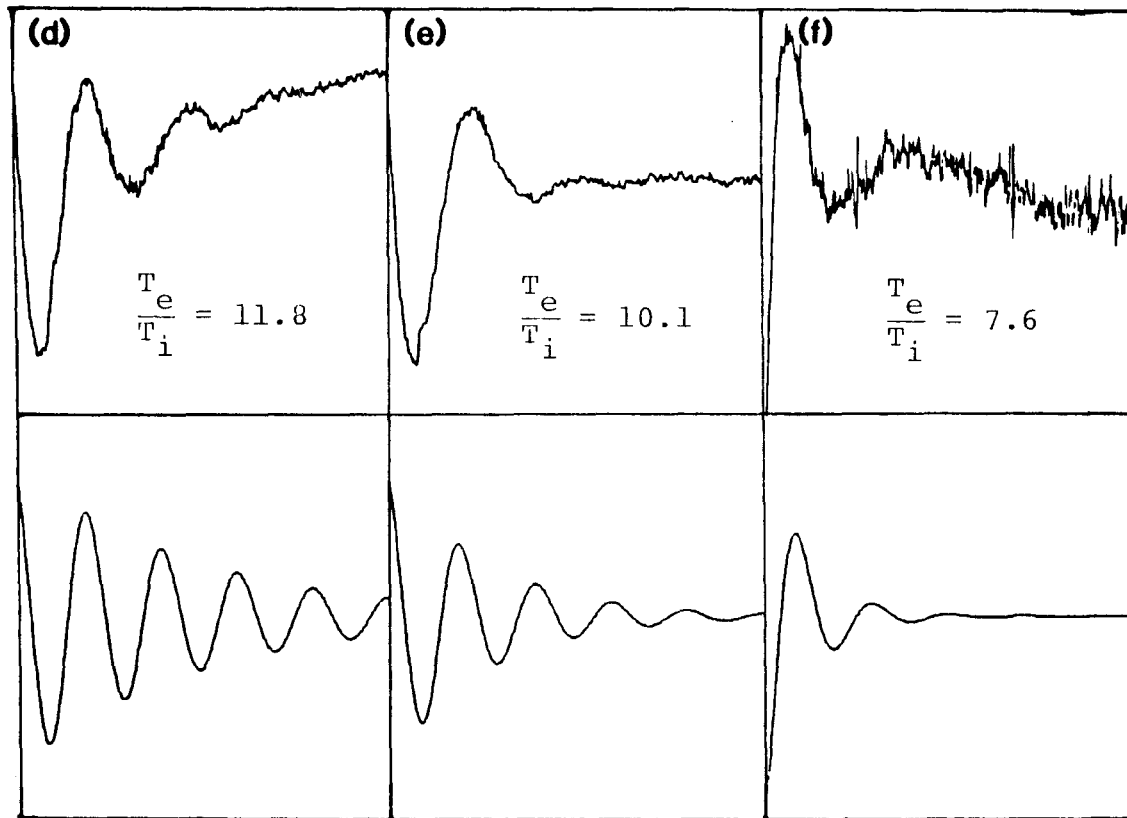
would therefore, be possible to observe ion acoustic waves. To this end an interferometer was set up, and measurements of wavelength and damping were made as a function of increasing plasma current. The details of the interferometer and the transmitting and receiving antennae are left to App. C. The results of this experiment are shown in Fig. 5.3. The ion sound speed was found from the wavelength and frequency of the acoustic waves, which allowed the electron temperature to be determined. Langmuir probe measurements were used to verify the electron temperatures thus determined. The Langmuir probe measurements were found to be about 10% higher than those determined from the wavelength measurements. It was suspected that plasma conditions were slightly different when the probe measurements were made. For this reason, the wavelength-determined electron temperatures were assumed to be correct in discussion that follows. Ion temperature measurements were made using LIF. From the measured values of $T_e$ and $T_i$, the theoretical damping could be calculated. The results of these calculations are displayed beneath the experimental data. In Fig. 5.3(a),(b),(c) the observed damping appears to be stronger than expected. This enhanced damping was evidently due to a $1/r$ fall off in wave intensity from the exciter probe. In Fig. 5.3(d),(e),(f), Landau damping became the dominant mechanism, and the observed and calculated damping were in good agreement. These data were important, not merely because they explain why ion acoustic waves were not previously observed, but also because they prove conclusively that the ion distribution functions determined using LIF were real and not merely an average over a series of coherent ion motions.

## 5.5 EVIDENCE FOR NON-ADIABATIC ION MOTION

### 5.5.1 DISTRIBUTION FUNCTION DATA

As has been noted previously, the ion motion in large amplitude electrostatic modes is non-conservative and an ion is completely free to attain very large (but not infinite) energies. As was noted in Chap. 4, the ratio of maximum stochastic energy to maximum, non-stochastic energy is given by

$$\frac{H_{stochastic}}{H_{non-stochastic}} \simeq \frac{(\alpha+2)^2}{4\alpha} \sim 2.5. \tag{4.18}$$

This result implies that ions can be accelerated to energies far exceeding the potential that is due to the drift wave trough. The potential amplitude of the drift wave can be determined by means of Langmuir probes. The theory of Langmuir probes has been covered in detail elsewhere (see, e.g., Chen (1965)) and will not be discussed in the present work. Electron temperatures were determined by measuring the electron $I - V$ characteristic and performing an exponential fit; electron densities were then determined from the ion saturation current and finally, the plasma potential was then obtained by measuring the floating potential and then correcting for the temperature fluctuations,

$$V_s - V_f = \frac{1}{2}T_e\ln\left(\frac{m_i}{2\pi m_e}\right). \tag{5.3}$$

Examples of the fluctuating plasma parameters are shown in Fig. 5.4. These data were taken at the plasma edge where the fluctuation levels are largest. These data were taken using an 8 bit Transiac transient recorder at a digitization rate of 200kHz. The data were averaged over 1000 plasma discharges to ensure precise plasma po-
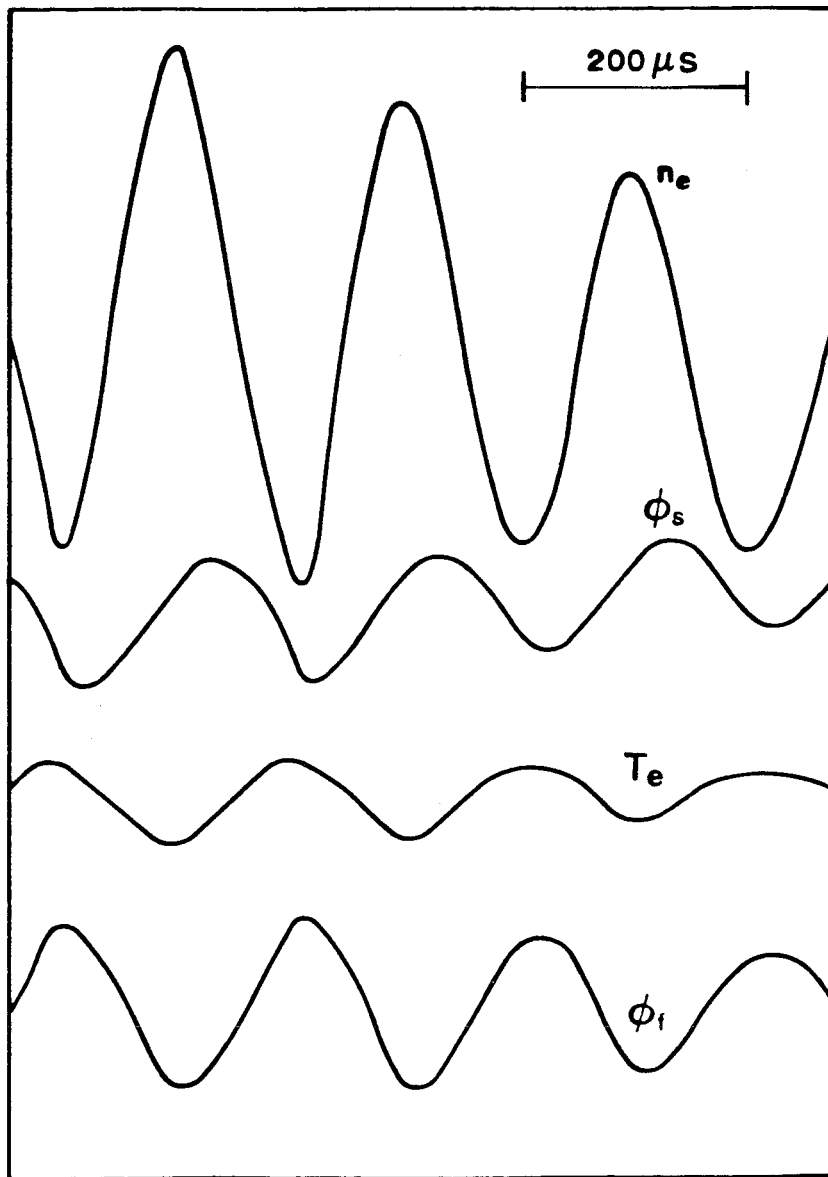
FIG. 5.4 Fluctuating plasma parameters measured by means of a Langmuir probe. 3000 plasma shots were required to obtain these data.

ential measurements. To maintain a constant phase reference, a separate Langmuir probe was used to trigger the data collection system. The duration of the sample shown is $200\mu s$, which corresponds to a full wave period. All fluctuating quantities shown are normalized to their mean values. By making these measurements at different radial positions in the plasma, it was possible to form a 2-D picture of the drift mode structure. Since the mode is rotating, it is possible to map the temporal fluctuations into the poloidal angle of the plots. Fig. 5.5 shows plots of density and plasma potential for a mode that is above the threshold for stochastic behavior. The coherent nature of the modes and their large amplitude are evident from these plots.

Using plots of this type, it was possible to measure the height of the potential trough that was due to the drift wave. The resonance fluorescence technique allows the ion velocity distribution to be mapped out, and hence the ion energy distribution is known and may be compared with the measured wave potential. Figure 5.6 shows two ion distribution functions obtained for wave amplitudes above and below the thresholds for stochastic ion motion (Fig. 5.6(a) and Fig. 5.6(b), respectively). The hatched regions indicate those ions that have energies greater than the peak to peak potential of the drift wave. Clearly, when the wave amplitude is above threshold, there are significant numbers of ions with energies considerably larger than the potential amplitude. Conversely, when the wave amplitude is below threshold, few ions have energies in excess of the potential amplitude of the wave.

## 5.5.2 OPTICAL TAGGING DATA

We hoped initially to use optical tagging to demonstrate non-conservative motion by showing that ions were being transported over the potential peak of the

**(a)**
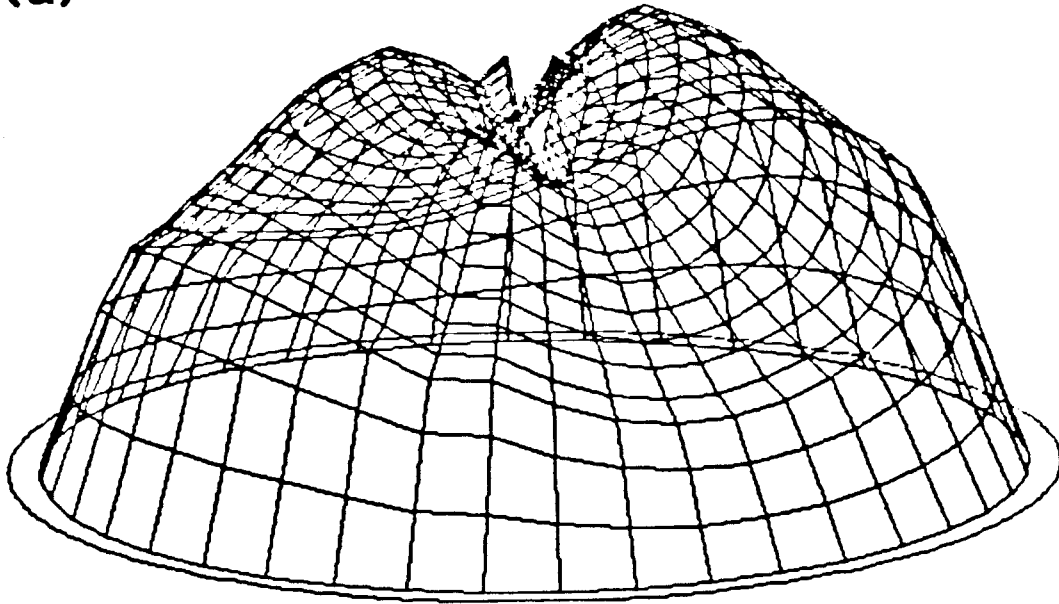


**DENSITY**

**(b)**
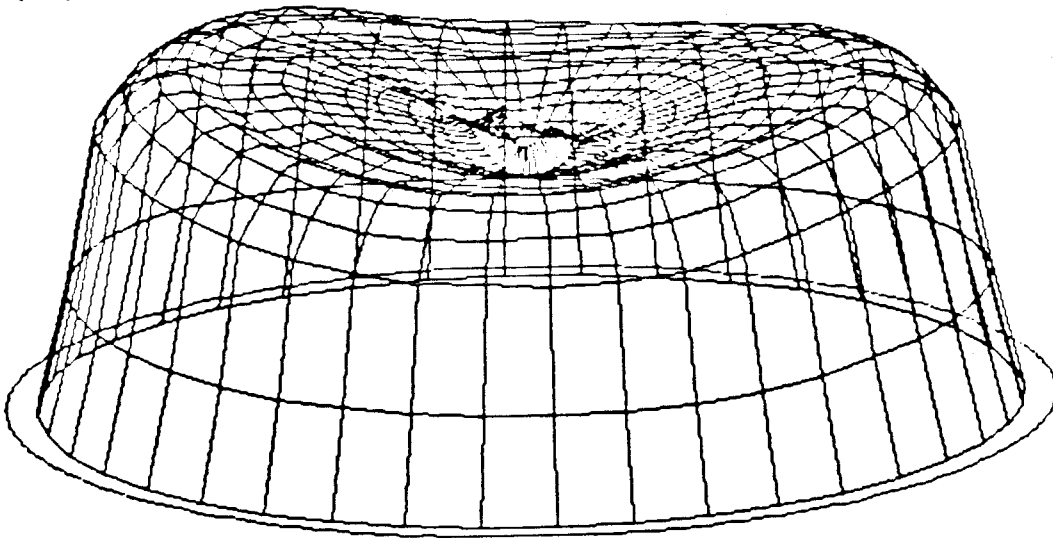


**SPACE POTENTIAL**

FIG. 5.5 Density and space potential plots for an m=2 mode. (a) Density. (Mean density $5 \times 10^{11} \mathrm{cm}^{-3}$.) (b) Space potential. (Mean potential 15V.)
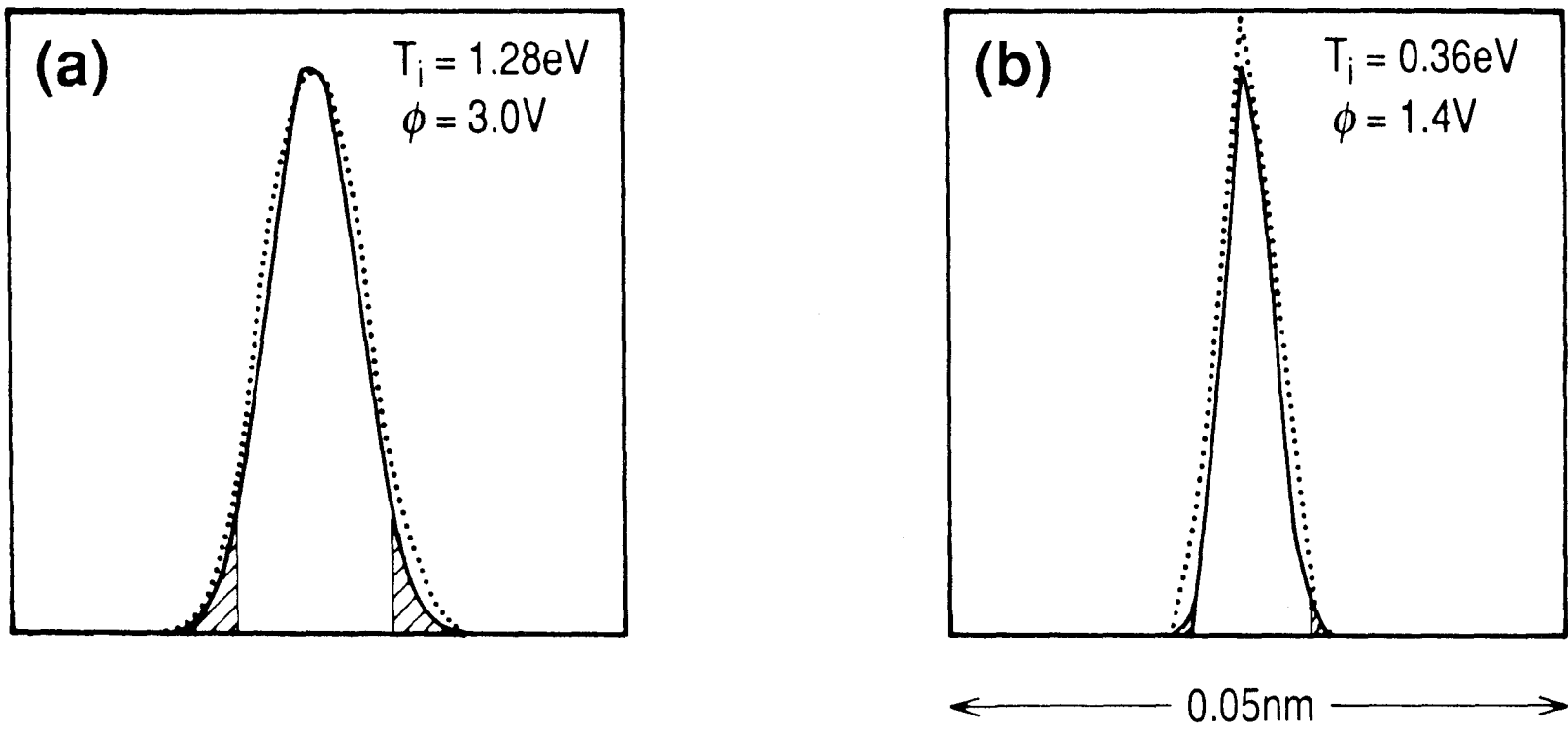
FIG. 5.6  Ion distribution functions, (a) above and (b) below the threshold for stochastic ion motion. The shaded regions represent those ions having energies greater than the peak-to-peak potential of the drift wave.

drift wave. However, this would have required the observation of ion transport over a distance of say $\pm\lambda/8$ relative to the wave peak. In practice, this would amount to a total distance of about 10cm. As described in Chap. 3, preliminary tagging experiments showed that it was difficult to trace tagged particles over distances greater than 1-2cm, this distance being set by the relatively low ion thermal velocities ($\sim 2 \times 10^5 \text{cms}^{-1}$) and the very short period for which the tagged levels remained depleted ($\sim 5\mu s$). In fact, only ions in the high energy tail of the ion distribution could be traced for even 1-2cm.

It was possible, however, to perform velocity selection using tagging as demonstrated in Sec. 3.6.3. The spatial and temporal separation of the pump and search beams was such that only energetic ions could be tagged. In addition, the probing laser pulses were fired only in the vicinity of the potential peak. In this way it was possible to observe quite energetic ions moving in regions of large space potential. If the ion motion were, in fact, conservative, then their energies should have been very low in these regions. A Langmuir probe was used to monitor the drift wave density fluctuations. It was found experimentally that the density fluctuations led the space potential fluctuations by approximately $\pi/4$. This is easily seen from Fig. 4.7 and Fig. 5.5. In the work of Fredricksen and Bellan (1985), it was stated that space potential fluctuations led density fluctuations. This statement is incorrect and leads to the erroneous conclusion that plasma is being transported radially inward and not outward, a result that contradicts the laws of thermodynamics. This reference probe was used to provide a $25\mu s$ gate that fired the pump laser and the boxcar averager whenever the search laser pulse fell within the gate period ensuring that tagging occurred only within $\pm\pi/8$ of the wave peak.

The search beam diameter was 3mm, while the pump beam was roughly 1.2cm square. The minimum beam separation was set to be 4mm. The pump beam was made very much larger than the search beam in the hope that it would essentially swamp the search beam with particles and thereby enhance the tagging effect. The time interval between the two laser pulses was 1.5$\mu$s, implying minimum particle velocities of $2.7 \times 10^5 \text{cms}^{-1}$ or energies of 3eV. Ion transport was examined both above and below the threshold for stochastic heating (see Figs. 5.7 and 5.8, respectively). At the same time, ion distribution functions were determined using LIF, and wave potential measurements were made using Langmuir probes. Figure 5.7(a) shows the boxcar output as a function of time. Very long averaging times were required to achieve a good signal-to-noise ratio. This time was further increased because the the boxcar averager was triggered only when the laser pulse occurred at the correct phase of the drift wave. When the "P" beam was turned on the "S" beam fluorescence signal was reduced by about 18%. Figure 5.7(b) shows the corresponding ion distribution function; the shaded region represents those ions having velocities exceeding $2.7 \times 10^5 \text{cms}^{-1}$. As expected, there exist a large population of energetic ions. Conversely, Fig. 5.8 shows similar plots for the case when ion heating is weaker. As expected, the presence of the "P" beam had little or no effect on the "S" beam fluorescence. The corresponding ion distribution function shows that few ions possess velocities exceeding $2.7 \times 10^5 \text{cms}^{-1}$.

## 5.6 NUMERICAL SIMULATION OF ION HEATING

Stochastic ion heating was demonstrated by means of particle simulations. The orbits of 2000 particles were followed using the representations of the drift wave po-

FIG. 5.7 Optical tagging data that demonstrate the existence of high energy ions when above the threshold for stochastic heating. (a) "S" beam fluorescence with and without the presence of the "P" beam. Beam separation was 4mm and time separation was 1.5µs, implying a velocity of $2.7 \times 10^5 \text{cms}^{-1}$. (b) Ion distribution function showing ions whose velocities exceed $2.7 \times 10^5 \text{cms}^{-1}$ (hatched region).

**(a)** S FLUORESCENCE (ARB. UNITS)

P ON

P OFF

P + S OFF

TIME (HOURS)

**(b)** $T_i = 0.69eV$

0.05nm
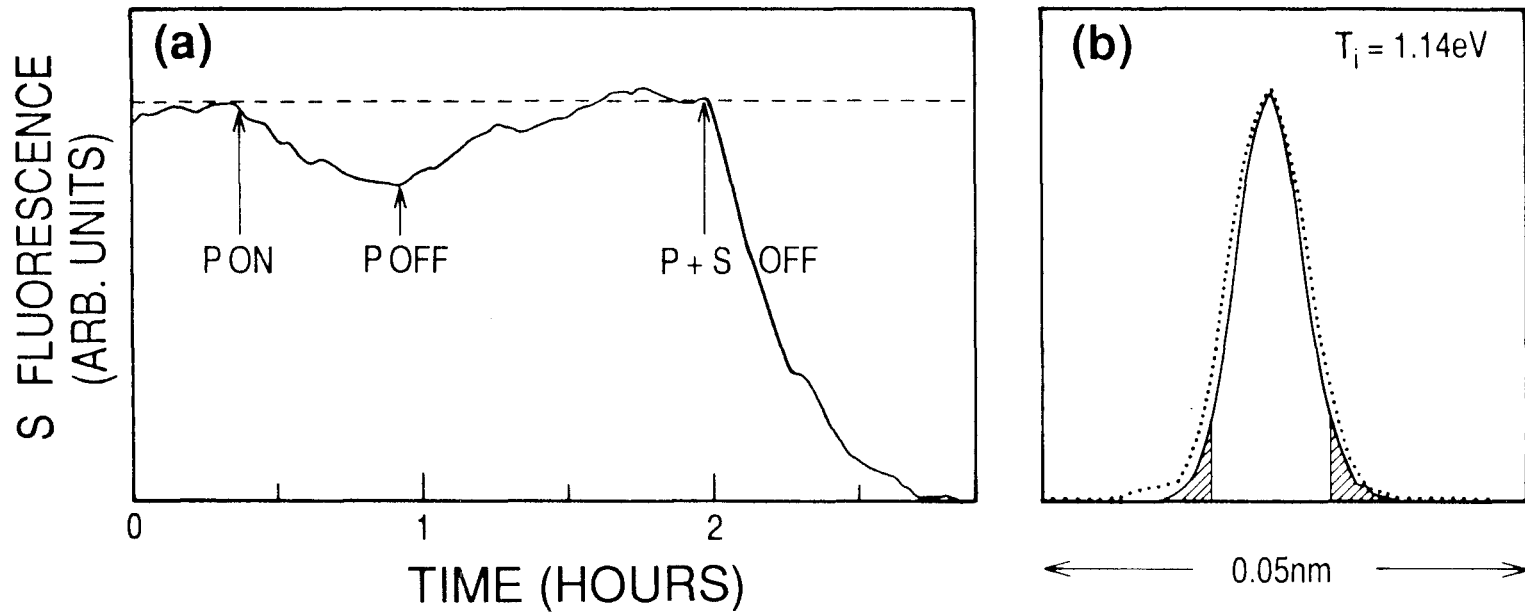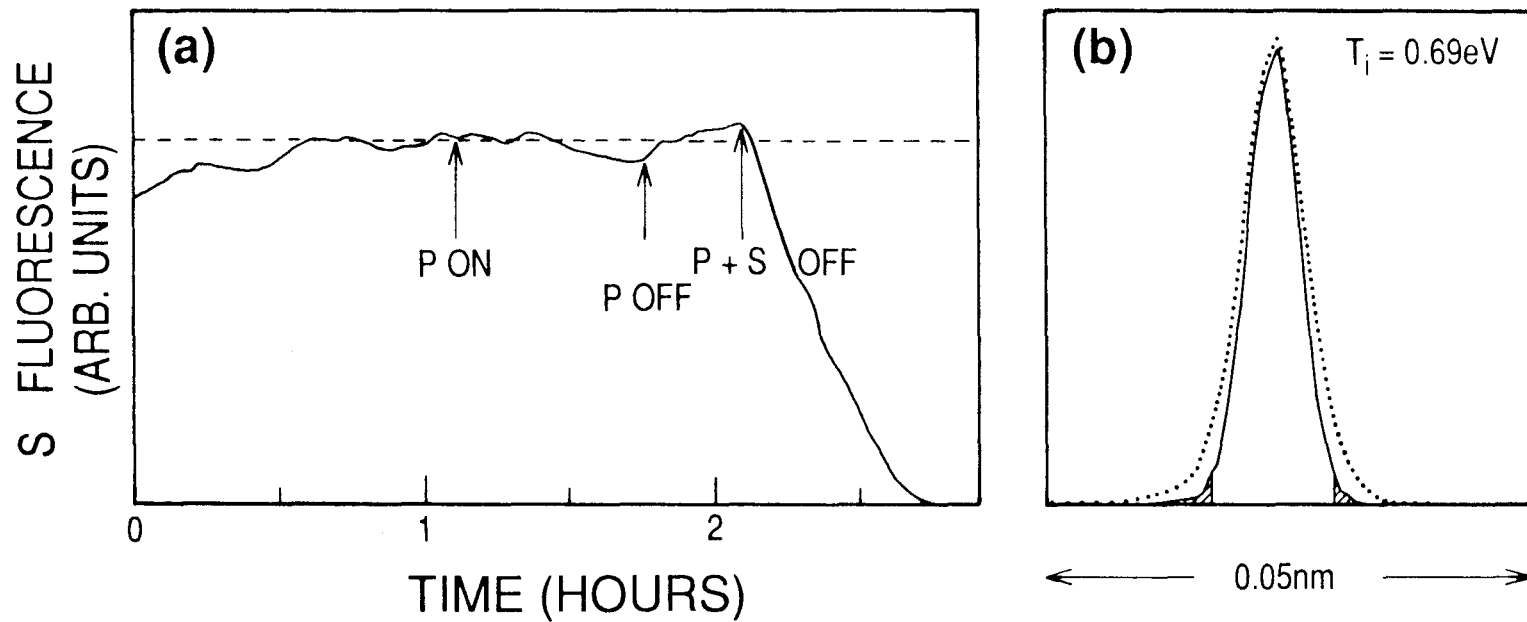
FIG. 5.8 Optical tagging data that demonstrate that few ions have high energies when below the threshold for stochastic heating. (a) "S" beam fluorescence with and without the presence of the "P" beam. Spatial and temporal separations of the beams are as in FIG. 5.7. (b) Ion distribution function showing ions whose velocities exceed $2.7 \times 10^5 cms^{-1}$ (hatched region).

tential pattern similar to that shown in Fig. 5.9(a). Fig. 5.9(a) may be compared to the measured equipotential surfaces shown in Fig. 4.4(b) of Chap. 4. The drift wave pattern was assumed to rotate at half the frequency of the drift wave. In the simulation only the toroidal magnetic field was considered, since this was much larger than the poloidal field. It was assumed to have the usual $R^{-1}$ dependency on the major radius. Ion motion along the magnetic field direction was ignored since for drift-Alfvén waves, $k_\perp \gg k_\parallel$. The ions were started from rest and their initial positions were randomly distributed across the chamber in a normal distribution with standard deviation of one-half the Encore minor radius. Each ion trajectory was integrated, and the one-dimensional velocity distribution function was calculated every 0.05 of a gyroperiod. Only those ions in the inner region of the chamber $(0 < r/a < 0.4)$ were used to calculate the distribution function. If an ion hit the wall, it was assumed to be lost and excluded from the calculation. Fig. 5.9(b) shows an example of an ion distribution function obtained from a simulation that used the pattern shown in Fig. 5.9(a). For this particular calculation; $B_0 = 500G$, $k = 0.317\text{cm}^{-1}$, $\nu = 5\text{kHz}$ and the potential $\phi = 4V$ p-p. The crosses represent calculated points and the solid line is a Gaussian fit to these points. The number of particles used in the simulation was insufficient to determine the deviation from a Maxwellian distribution. However, no gross deviations were ever consistently observed. This is an important point because it strongly suggests that collisions are not required in order to obtain the Maxwellian distribution functions observed experimentally.

Before comparing the experimental results with those obtained from the simulation, it is informative to examine the actual trajectories of individual ions under
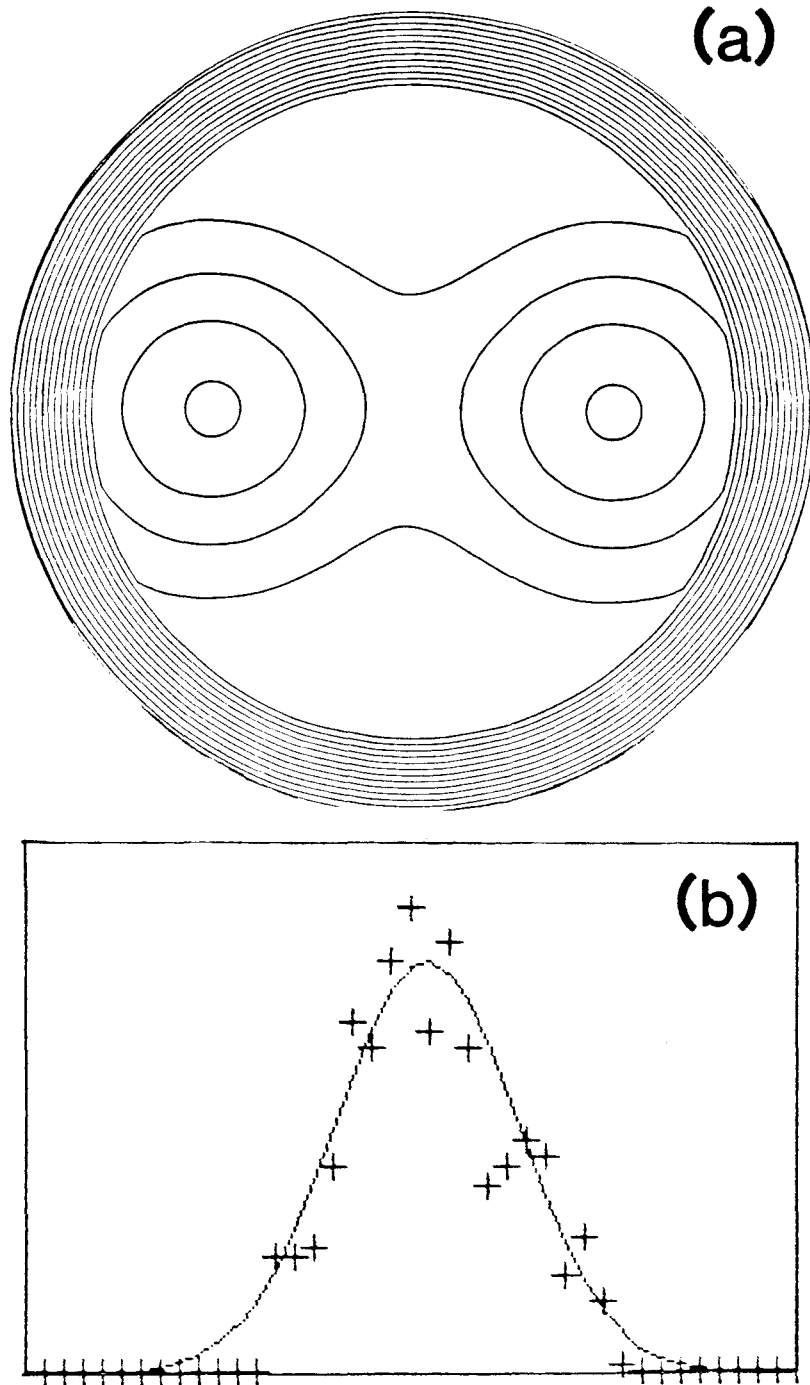
FIG. 5.9 (a) Contour plot of model drift wave space
potential (1V/contour). (b) Typical ion distribution
function determined using the model shown in (a). $T_i$
for this distribution was 2.3eV.

different conditions. In Fig. 5.10(a) we show the trajectory of a single ion executing stochastic motion under the influence of a field pattern of the type shown in Fig. 5.9(a). The inside wall of the chamber is to the left, and the magnetic field strength decreases from left to right across the chamber. For this calculation; $B_0 = 400G$, $k = 0.317\text{cm}^{-1}$, $\nu = 5\text{kHz}$, and $\phi = 1.9\text{V}$ p-p giving, $\alpha = 0.25$. The irregular nature of the ion motion is evident. In Fig. 5.10(b) the ion kinetic energy (normalized to the p-p potential amplitude) is plotted as a function of time for the trajectory shown. As might be expected, the energy varies dramatically and quite randomly and often exceeds the p-p potential energy of the drift wave. In contrast, Fig. 5.11 shows the trajectory and temporal variation of kinetic energy of an ion executing guiding-center motion. The parameters used for this calculation are identical to those used in the first calculation, except that the potential amplitude has been reduced to 1.7V p-p, giving $\alpha = 0.23$. The effect of this very small reduction in wave potential is remarkable. The ion motion is regular and the kinetic energy oscillates sinusoidally between zero and some small amplitude as it gains and loses energy reversibly in the wave field. The two preceding examples were carefully chosen to show the importance of initial conditions on the ion motion. Note that ion motion was not globally stochastic in either of the above cases since, $\alpha \ll 1$.

Figure 5.12 compares the heating results of a simulation to experimental heating results for an $m=2$ drift-Alfvén wave. The experimental data were recorded at the plasma center and the simulation results also pertain to this region. The mode frequency, wavenumber and wave amplitude were measured experimentally by means of a Langmuir probe and the toroidal field power supply was calibrated, so that the magnetic field was known. These experimentally determined parameters

102

**(a)**

START

**(b)**

K. E. / q Φ

2

1

0        100       200       300

TIME (μ s)

FIG. 5.10  (a) Typical calculated ion trajectory showing
stochastic ion motion. (b) Kinetic energy of the same
ion (normalized to max. potential energy in the wave)
as a function of time.

**(a)**

**START**

**(b)**
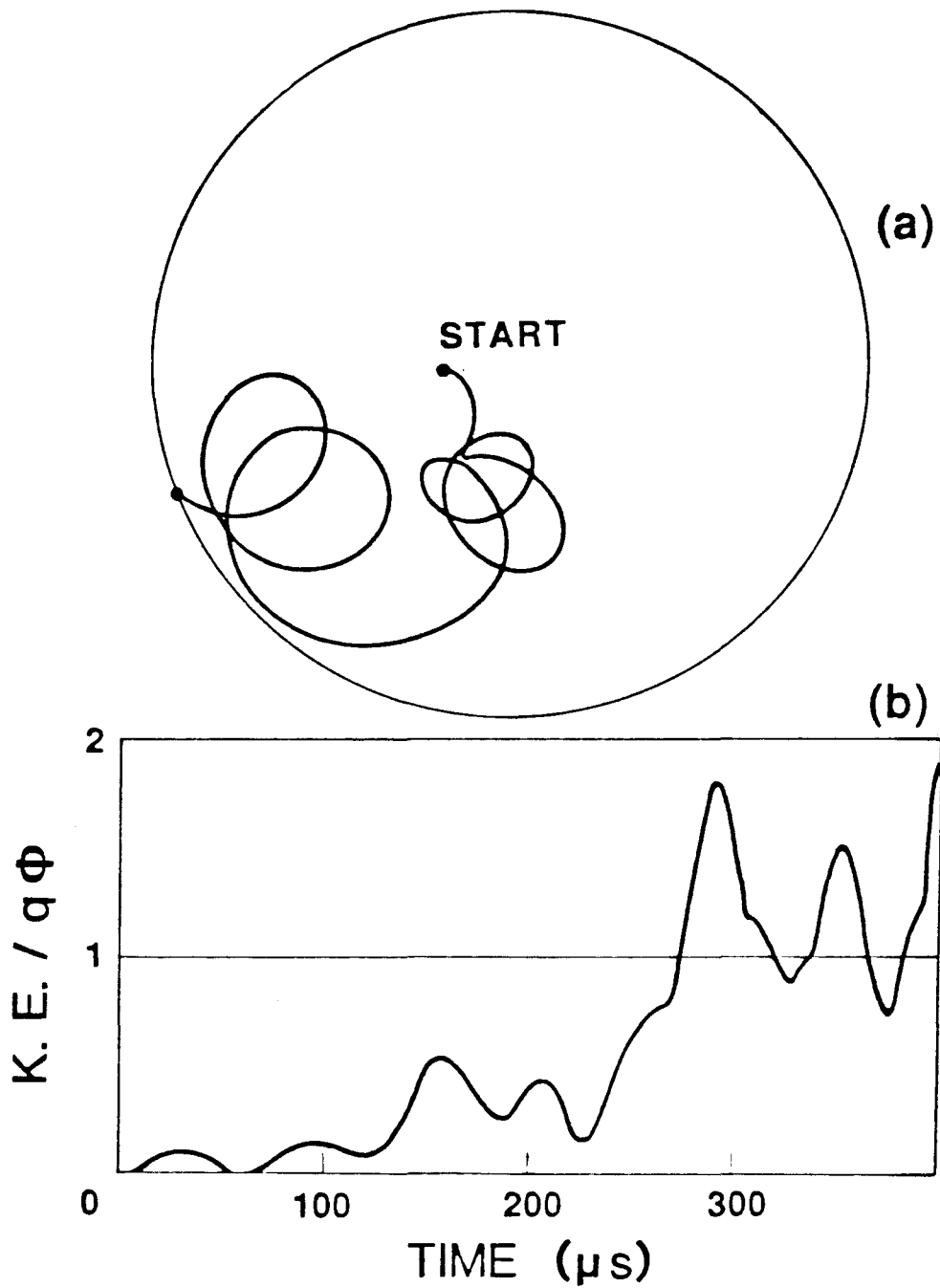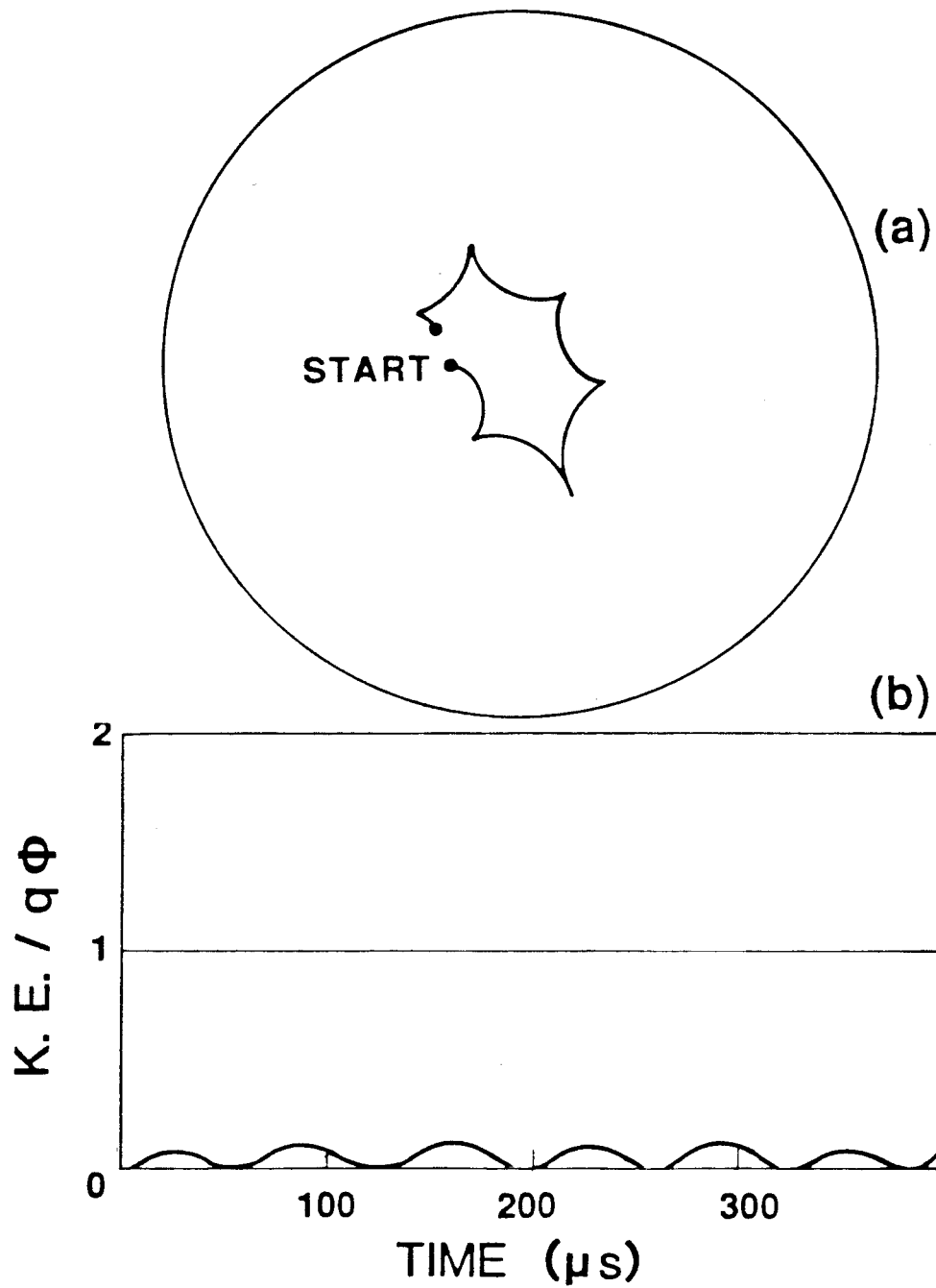
FIG. 5.11 (a) Typical calculated ion trajectory showing
regular ion motion. (b) Kinetic energy of the same ion
(normalized as before) as a function of time.
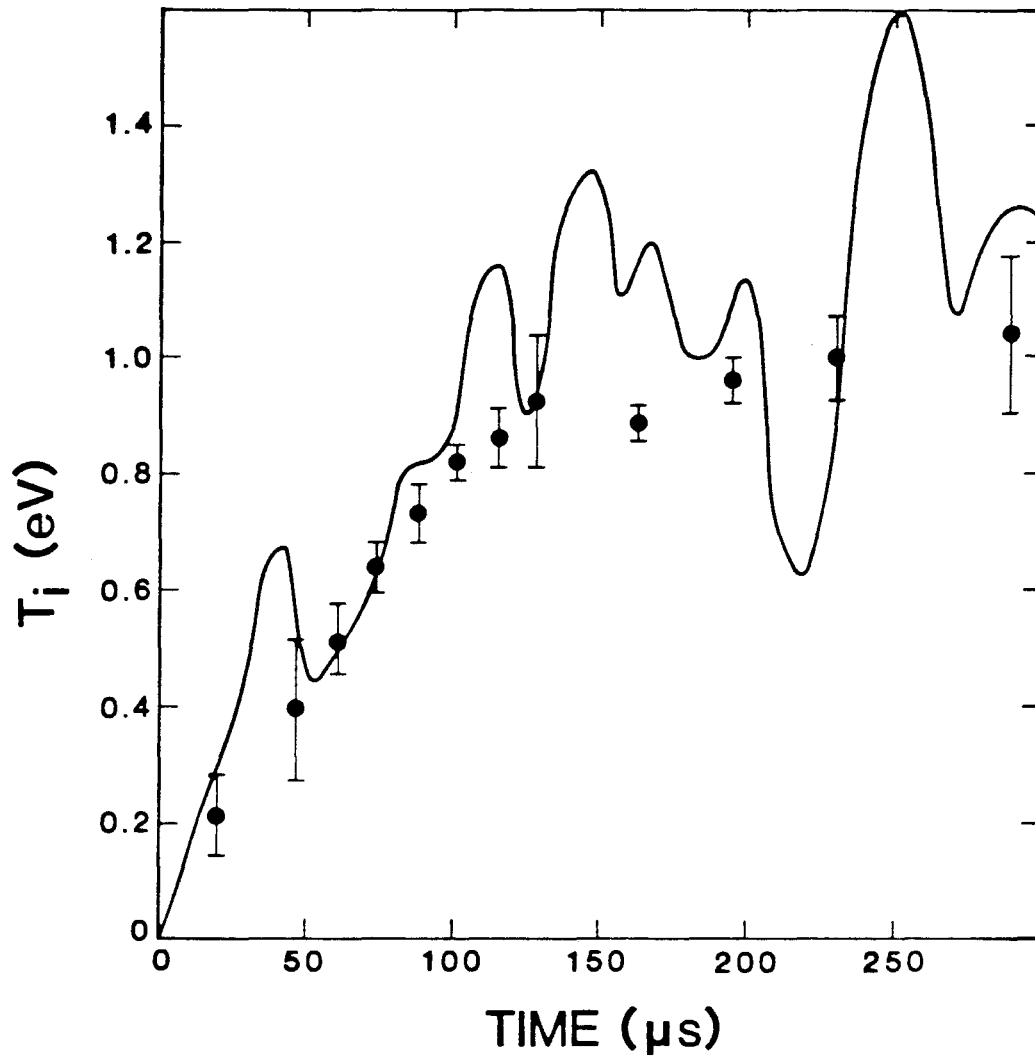
FIG. 5.12 Simulation of ion heating in the field of a drift wave. The solid line represents the results of the simulation, while the individual data points represent actual ion temperature measurements.

were then used in the numerical calculation. The parameters used were; $B_0 =$ 400G, $k = 0.317\text{cm}^{-1}$, $\nu = 5\text{kHz}$ and $\phi=2\text{V}$ p-p. The actual measured potential was 3.5V p-p, a value much higher than that used in the calculation. Using a value of 3.5V in the calculation resulted in such strong heating that all the particles in the simulation were lost within 50-100$\mu$s, and the calculation broke down. Using this low value for $\phi$ the heating rate and final ion temperature predicted from the simulation are in good agreement with the experimental results. The above discrepancy could probably be removed if ion cooling mechanisms such as charge exchange were taken into account. The model assumed above was not fully self-consistent since the collective interactions of the ions were not considered. Such models are still valid since the electric fields used in the calculations were measured experimentally and the ions must move in accordance with the Lorentz equation. Collisions, field inhomogeneities, etc., will alter the orbits calculated above but cannot alter the essential results of the calculations.

## 5.7 CAN ION SLOSHING ACCOUNT FOR OBSERVED TEMPERATURES?

The suspicion may exist, that the ion temperatures determined above, are merely a manifestation of the averaging technique used in the present work. Is it not possible, that the average of a large number of coherent motions, could yield a fairly broad velocity distribution? We can refute this argument on simple theoretical and experimental grounds. If ions were simply sloshing in the potential well, the maximum kinetic energy that an individual ion could attain, is determined by the height of the well. In order to obtain a velocity distribution that looked Gaussian, the mean ion energy would necessarily be far less than this maximum. At the very most, the mean velocity must be one third or less of the maximum velocity. This

implies a mean kinetic energy of one tenth of the maximum potential in the well. A typical drift-Alfvén potential amplitude was 2V peak-to-peak implying $T_i \sim 0.2\text{eV}$. As we have seen, ion temperatures far greater than this value were observed. In fact, ion kinetic energies exceeding the well potential were observed. Such sloshing would also imply that the ions were undergoing completely reversible motion, in other words, that at some point they would return to their initial rest positions, and the apparent ion temperature would return to zero. This has certainly not been observed experimentally. It is also apparent that there should be very large shot-to-shot variations in the fluorescence signal, as the laser beam hit the wave at different phases. This was never observed experimentally. Finally, a velocity spread due to such sloshing motion would be non-Gaussian. The observed velocity distributions were always very close to Gaussian.

# CHAPTER 6

## OTHER THOUGHTS AND CONCLUSIONS

The techniques of laser induced fluorescence (LIF) and optical tagging (OT) have been successfully applied to Q-machine and discharge plasmas for several years. In the present work we have undertaken a series of LIF experiments in the Encore tokamak, the initial purpose of which was to extend this powerful technique into the realm of more complex plasma devices. To demonstrate the effectiveness of LIF and the related OT technique, two experiments were performed. The first experiment examined ion heating by lower hybrid waves. Ion distribution functions and hence ion temperatures were obtained as a function of applied RF power, and ion temperatures nearly doubled when RF power levels were increased from zero power to 16kW. Next, the OT technique was successfully used to display ion gyro-rotation and in particular to show that the direction of rotation was reversed when the magnetic field direction was reversed.

LIF was then used to demonstrate that ion heating in the Encore tokamak was anomalously fast. This fast heating was shown to be due to large amplitude, low-frequency drift-Alfvén waves. These waves were often coherent in Encore and were of sufficient amplitude that ion motion became stochastic in their presence. Calculations using a slab model to describe the geometry showed that the wave amplitude had to be of sufficiently high amplitude in order to cause heating. This condition could be written as $\alpha = m_i k^2 \phi_0 / q B_0^2 \sim 1$. Physically, this condition was shown to correspond to the ion excursion that was due to the polarization drift becoming comparable to the wavelength of the mode. At this point the guiding

center approximation breaks down and the ion motion becomes non-adiabatic. Our calculations showed that the condition $\alpha \sim 1$ held regardless of the wave frequency, as long as $\omega < \omega_{ci}$. For the case $\omega \gg \omega_{ci}$, the wave amplitude had to be much higher (Karney, 1978). When heating takes place, ions may traverse a large region of phase space, and be heated to very high energies. It was also shown that stochastic ion heating for these conditions was due to a trapping/detrapping process.

These drift modes were current-driven and it was possible to increase the saturated mode amplitude by carefully raising the plasma current. In this manner it became possible to observe the transition from adiabatic to stochastic motion. As expected from the numerical results of Chap. 4, this transition was quite abrupt.

As a check on the LIF temperature measurements Landau damping of ion acoustic waves was measured as a function of $T_e/T_i$. The observed damping was in fairly good accord with the calculated damping. At high $T_e/T_i$, the observed damping was somewhat stronger than expected and the reason for this stronger damping has not yet been clarified. Damping by neutrals was far too small to account for the extra damping. Quite apart from the intrinsic interest in studying ion acoustic waves in a tokamak device, these measurements proved conclusively that the LIF determined ion temperatures were valid and not merely an artifact of the averaging procedure.

It was shown that the ion motion was non-adiabatic, i.e., that truly stochastic behavior was taking place, by showing that significant numbers of ions possessed kinetic energies that were far in excess of their maximum possible potential energies in the field of the drift wave. The existence of these very energetic ions was predicted from the Poincaré surface of section plots presented in Chap. 4. From these plots

it was also evident that ions could not be accelerated to arbitrarily high energies, and the peak ion energy was given by the approximate relation

$$\frac{H_{stochastic}}{H_{non-stochastic}} \simeq \frac{(\alpha + 2)^2}{4\alpha}, \tag{4.18}$$

where $H_{non-stochastic}$ was the maximum energy attainable in the potential well of the wave. It was not possible to demonstrate this maximum definitively because of the small number of ions in the wings of the ion distribution function. It was clear that the numbers of ions exceeding this limit was below the limits of detection of the system.

A particle simulation of ion heating that was due to a low-frequency electrostatic mode was able to reproduce the observed heating rate and peak ion temperature. The trajectories of 2000 particles were followed in a realistic representation of the drift wave field. These results were used to produce a series of velocity distributions at the center of the device. Because of the relatively low number of test ions used, it was difficult to determine with certainty how Maxwellian the resulting distribution functions were. However, no gross deviations from Maxwellian behavior could be discerned. Therefore, an essentially Maxwellian distribution was obtained without the mediation of ion-ion collisions. At low ion temperatures ($T_i$ <1eV), ion collision frequencies become quite high and any non-Maxwellian features will disappear.

Another interesting feature of these calculations was the very low heating rates obtained when the mode amplitude was below threshold. In addition, examination of the trajectories of individual ions shows remarkable differences above and below threshold. Below threshold the trajectories were regular, and kinetic energy showed

a periodic variation with time. The motion is termed to be superadiabatic. Above threshold the motion was quite different; the trajectories were very erratic and the kinetic energy fluctuated randomly. In other words, the motion was stochastic.

It is interesting to note that anomalously high ion temperatures and anomalously high rates of ion heating have been observed in all major, reversed-field pinch (RFP) experiments (Howell and Nagayama, 1985; Ogawa et al.,1985; Ortolani, 1985; Bodin and Evans, 1985). For instance, Howell and Nagayama (1985) show that in ZT-40, ion temperatures exceeded electron temperatures for sufficiently large plasma currents ($T_i \approx 600eV$, $T_e \approx 450eV$, $I > 300kA$). Also, these ion temperatures were reached in 1ms or less, i.e., faster than would be possible via collisional energy exchange with electrons. Several authors have proposed the existence of current-driven instabilities in RFP's (Gladd and Krall, 1986; Cayton, 1985; Mondt and Goedert, 1985). In particular, Gladd and Krall (1986) have shown drift waves to be destabilized strongly by the high currents found in RFP's. It is well known that the stability of drift waves is dependent upon the ratio of electron drift velocity to electron thermal velocity ($u/v_e$). Typical values of $u/v_e$ for both Encore and ZT-40 are about 0.11, contrasting with a value of about 0.01 for a typical large tokamak such as PLT. In RFP's, ion heating has been observed to scale strongly with the ratio of plasma current to line density (I/N) (see, e.g., Howell and Nagayama, 1985) and hence must depend strongly on electron drift velocity. For most tokamaks, ion heating is independent of $u/v_e$ and proceeds at a rate in accordance with Eq. 3.6. It is clear from the present work that the ratio of ion Larmor orbit size to scale size of the mode (or modes) present is crucial in determining whether or not the ion heating can take place. In RFP devices, the Larmor orbit size can

become very large, particularly in regions of field reversal, and it is possible that orbit sizes may be larger than the scale size of existing instabilities. Few $\tilde{\phi}$ measurements have been made on RFP's; however, double-probe measurements were made on Zeta (Robinson and Rushbridge, 1971). These measurements showed 50-100kHz electric field fluctuations of 1000-3000Vm$^{-1}$ and perpendicular correlation lengths $\lambda_\perp \sim 5$cm in deuterium discharges with $B \simeq 1000$G. These parameters give $\alpha \simeq 1$ and $\nu \simeq 0.1$, i.e., the same parameter regime responsible for stochastic heating in the present work, so it is possible that stochastic heating by drift or other electrostatic instabilities is responsible for the high ion temperatures observed in RFP's.

It is also worth noting that $\alpha$ depends linearly on $m_i/Z$, and so impurity ions will be stochastically heated at faster rates than hydrogen or deuterium majority ions but may then heat these majority ions via ion-ion collisions. Also, spuriously high ion temperatures may be inferred from spectroscopic measurements of linewidths of heavy impurity ions if they have not come into equilibrium with the bulk plasma.

Until recently, it has been implicitly assumed that there are only two categories of heating mechanisms at play in non-turbulent plasmas, viz., collisions and resonant wave-particle interactions. Thus, all proposed plasma heating schemes have been dependent on resonant interactions. It is clear from the present work that the wave causing the enhanced ion heating need not be near any plasma resonance. Similar results are predicted in the theoretical work of many authors (e.g. Smith and Kaufman (1975); Karney (1978); Hsu (1982); Drake and Lee (1981)). Also clear is the fact that the exact nature of the mode is not important. The theoretical

basis of the present work was very general. Any electrostatic mode propagating perpendicular or obliquely to a uniform magnetic field is potentially capable of causing stochastic particle motion and hence, heating. The only requirement on the mode is that it be of sufficient amplitude. In the present work and the work of Drake and Lee (1981), low-frequency waves ($\omega < \omega_{ci}$) were considered and the underlying physical mechanism causing stochastic behavior was particle trapping. In Karney's (1978) work, high-frequency waves were considered ($\omega \gg \omega_{ci}$). Here, ion motion becomes stochastic as a result of the non-linear interaction of the resonances between the cyclotron motion and the wave. If the interacting RF field is of sufficient amplitude, the ion "forgets its phase" relative to the wave during a cyclotron period. At some point in their orbits such ions will experience the wave-particle resonance condition $\omega = \vec{k} \cdot \vec{v}$. Since in Karney's work $\omega \gg \omega_{ci}$, the particles act as though in a zero magnetic field while in resonance with the wave and so exchange most energy with the wave at those points.

As is the norm, we conclude this work with suggestions for future investigations. It is clear that there is a distinct difference in the type of ion trajectory when the motion is adiabatic and when it is stochastic. The simple experiment to demonstrate ion gyrorotation using optical tagging discussed in Chap. 3 suggests an elegant method for measuring the circularity of the ion trajectories. If instead of using a broadband pump as was done in the present work, a narrowband pump is used, then obviously a much smaller class of ion will be tagged. Only that class of ions satifying the relation

$$v_y = v_\perp \sin\phi_0 \tag{6.1}$$

will be resonant with the exciting laser beam. In addition, as described in Chap. 3, only those ions satisfying Eq. 3.11 will enter the path of the search beam.

$$v_\perp = \frac{\omega_{ci}d}{\sin(\omega_{ci}t + \phi_0) - \sin\phi_0} \tag{3.11}$$

These two equations serve to fix $v_\perp$ and $\phi_0$ exactly, and so the narrowband search laser will yield a tagged signal only when tuned to

$$v_y' = v_\perp \sin(\omega_{ci}t + \phi_0). \tag{6.2}$$

Now this result presupposes that the ion trajectories are perfectly circular. Any deviation from non-circularity will break the condition set by Eq. 3.11 and will result in a larger class of ions that can interact with the search laser and hence broaden the lineshape of the tagged ions. Of course, this result depends not only on the pump laser's being narrow but also depends on the temporal and spatial widths of the two laser pulses' being small. These conditions may be difficult to obtain in Encore because the plasma volume is large, and so the background spontaneous emission tends to mask the fluorescence signal.

Another technique currently being implemented on Encore is the use of a fast imaging system using an array of miniature photomultiplier tubes. By using mutiple passes of the laser beam, it should be possible to image a 2-D plane of LIF signals simultaneously.

## APPENDIX A

## UNSTABLE RESONATOR OPTICS FOR COPPER VAPOR LASER

Unstable resonators are generally regarded as the best resonators for lasers with large volume, homogeneous active media emitting high intensity radiation (Hanna, 1970). The use of an unstable resonator ensures the emission of a single transverse mode.

In order to introduce the concept of an unstable resonator, it is convenient to construct the Fox and Li mode chart; see Fig. A.1(a). We first define two normalized curvature or g parameters (one for each mirror of the resonator); $g_i = 1 - l/R_i$ for $i = 1, 2$. Here, $l$ is the distance between the two mirrors and $R_i$ are the respective radii of curvature. Any resonator may be represented by a point on the chart. A resonator for which the point $(g_1, g_2)$ falls within the shaded region of the chart is stable or low loss. Such resonators satisfy the condition,

$$0 \leq g_1 g_2 \leq 1. \qquad (A.1)$$

For resonators well inside the stable region, the low-order, resonant electromagnetic modes are mainly confined along the axis of the resonator and have Gaussian amplitude dependences (Yariv, 1975). The diffraction losses (energy losses around the edges of the mirrors) are small for such resonators. Conversely, resonators for which the point $(g_1, g_2)$ falls outside the shaded regions are unstable or high loss. Unstable resonators have large diffraction losses but possess characteristics that make them practical for certain laser applications. In particular, unstable resonators exhibit pronounced transverse mode selection. In other words, they are

**(a)**

$$g_2 = 1 - \frac{\ell}{R_2}$$

Planer

Confocal

Concentric

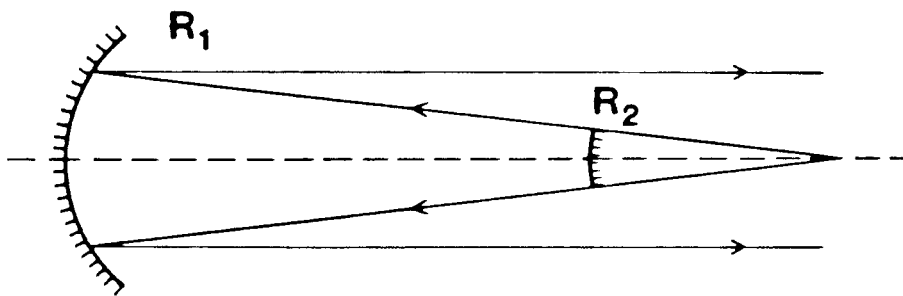$$g_1 = 1 - \frac{\ell}{R_1}$$
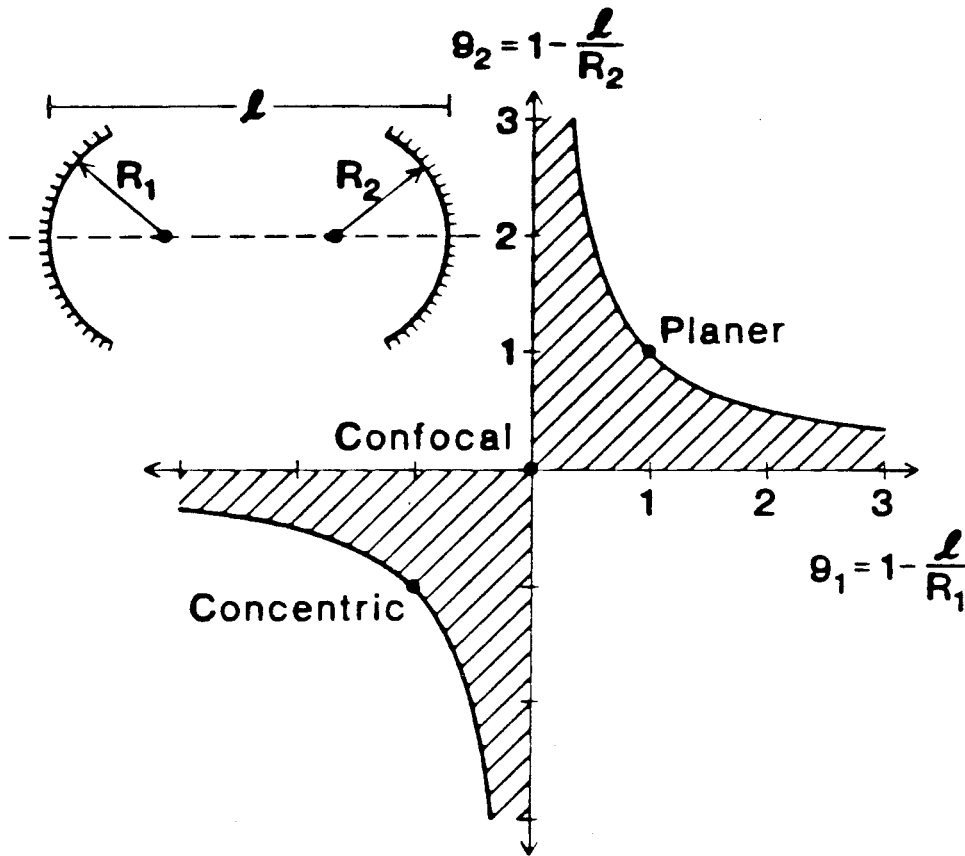
**(b)**

FIG. A.1 Unstable resonators. (a) Fox and Li chart. Stable resonators fall within the hatched region, while unstable resonators fall outside this region. (b) Telescopic resonator of the type used in the present work.

more lossy for higher-order modes than for lower-order modes. This mode selection results in a reduction of the angular divergence of the output beam.

In addition to transverse mode selection, unstable resonators also provide efficient output coupling via "diffraction coupling." In diffraction coupling the diffraction losses provide the means for output coupling. This method is particularly well suited to high-gain lasers requiring large output coupling. An example of such a resonator is shown in Fig. A.1(b). The smaller output mirror is totally reflecting and the near field output is annular. However, the far-field pattern is a spherical wave. This type of resonator was used in the present work and is known as a telescopic resonator. Such a resonator satisfies the following conditions:

(i) The mirror separation is given by $R_1 - R_2 = 2l$, where $R_1$ and $R_2$ are the radii of curvature for the back and front mirrors respectively.

(ii) The diameter of the output mirror is given by the expression

mirror diam.=beam diam./magnification.

The output mirror is generally a highly reflecting dot deposited on a convex substrate. This substrate will clearly act as a converging lens and must be followed by a diverging lens if the output beam is to be parallel. An elegant solution to this problem is to deposit the dot on a zero power menicus lens. To establish the criterion for a zero power lens, consider the thick-lens formula,

$$\frac{1}{f} = (n - 1)\left(\frac{1}{R_2} - \frac{1}{R_3} + \frac{t(n - 1)}{nR_2R_3}\right), \qquad (A.2)$$

where $R_2$ and $R_3$ refer to the radii of curvature of the output lens. Note that the front mirror of the resonator is formed on the surface of the lens; hence, $R_2$ is the same for both the mirror and the lens. When $f = \infty$,

$$t = \frac{n}{n-1}(R_2 - R_3). \qquad (A.3)$$

The back mirror of our resonator was coated with a broadband dielectric mirror that was at least 98% reflecting at 510nm and 578nm. The output mirror was an enhanced, aluminum dot coating (reflectivity 95%) on a substrate that was broadband, anti-reflection coated. The components selected had the following specifications: $R_1$ =5000mm, $R_2$ =523mm, $R_3$ =-512.5mm, dot diam.=5.7mm. The use of this resonator resulted in greatly improved beam quality when compared with normal flat resonators supplied with the CVL, and beam divergence was reduced from $\sim$10mrad to $\sim$1mrad. The average output power was reduced by about 10% when the unstable resonators were used; however, this reduction was more than offset by greater pumping efficiency.

118

## APPENDIX B

## DERIVATION OF DRIFT-ALFVÉN DISPERSION RELATION

The following derivation of the dispersion relation for drift-Alfvén waves follows
Bellan (private communication), who in turn based his derivation on the work of
Kadomtsev (1965). When the parallel phase of a drift wave becomes comparable to
the Alfvén speed ($\omega/k_z \sim v_A$), the electric field can no longer be considered curl-
free. In this case the magnetic field lines are no longer completely rigid and they
become slightly bent. The electric potential can then be thought of as consisting of
two parts, $\psi$ and $\phi$, such that

$$E_z = -\frac{\partial \psi}{\partial z}, \quad E_\perp = -\nabla_\perp \phi. \qquad (B.1)$$

In a dense plasma where the Debye length is small, quasi-neutrality can be
assumed; i.e., $\tilde{n}_e \simeq \tilde{n}_i$. The ion density perturbation is obtained from the ion
equation of motion and the ion continuity equation.

$$m_i \frac{d\vec{v}_i}{dt} = q_i \left( \vec{E} + \frac{\vec{v}_i \times \vec{B}}{c} \right) \qquad (B.2)$$

$$\frac{\partial \tilde{n}_i}{\partial t} + \nabla \cdot n\tilde{\vec{v}}_i = 0 \qquad (B.3)$$

The ion equation of motion may be solved to give

$$\tilde{\vec{v}}_i = \frac{c\vec{E} \times \vec{B}}{B^2} - \frac{m_i c^2}{eB^2} \dot{\vec{E}}. \qquad (B.4)$$

Substituting the expression for $\tilde{\vec{v}}_i$ into the continuity equation gives the ion density
perturbation

$$\frac{\tilde{n}_i}{n} = \left(\frac{\omega^*}{\omega} + k_\perp^2 \rho_s^2\right)\frac{e\phi}{T_e}. \tag{B.5}$$

The divergence of the parallel ion flux is negligible and has been ignored in Eq. B.5.

The electron equation of motion is now used to obtain the electron density perturbation.

$$m_e\frac{d\vec{v}_e}{dt} = q_e\left(\vec{E} + \frac{\vec{v}_e \times \vec{B}}{c} - \nu m_e\vec{v}_e - \frac{\nabla(nT_e)}{n}\right) \tag{B.6}$$

Assuming $m_e \sim 0$, the zeroth order solution to this equation is

$$\vec{v}_e = -\hat{y}\frac{cT_e}{eBn}\frac{dn}{dx}. \tag{B.7}$$

Substituting for $\vec{v}_e$, the $z$ component of the linearized electron equation of motion is

$$ik_\perp\psi - \frac{cT_e}{eBn}\frac{dn}{dx}\tilde{B}_x - \frac{ik_z T_e}{en}\tilde{n}_e = 0. \tag{B.8}$$

Using the $x$ component of the linearized Faraday's law ($\tilde{B}_x = -ick_\perp k_z(\psi - \phi)/\omega$), $\tilde{B}_x$ can be removed from Eq. B.8, giving

$$\frac{\tilde{n}_e}{n} = \frac{e\phi}{T_e} + \frac{e(\psi - \phi)}{T_e}\left(1 - \frac{\omega^*}{\omega}\right), \tag{B.9}$$

where $\omega^*$ is the diamagnetic drift frequency. It is now necessary to find another equation for $\psi - \phi$. This is done by considering the current conservation equation,

$$\nabla \cdot \vec{j} = 0. \tag{B.10}$$

The $z$ component of the current density perturbation is

$$\tilde{j}_z = \frac{i}{k_z} \nabla \cdot (n_i e \vec{\tilde{v}}_{i\perp} - n_e e \vec{\tilde{v}}_{e\perp}). \qquad (B.11)$$

But

$$\nabla \times \vec{E} = -\frac{1}{c} \frac{\partial \vec{B}}{\partial t}, \qquad (B.12)$$

and

$$\nabla \times \nabla \times \vec{E} = -\frac{1}{c} \frac{\partial (\nabla \times \vec{B})}{\partial t} = -\frac{4\pi}{c^2} \frac{\partial \vec{j}}{\partial t}, \qquad (B.13)$$

Linearizing Eq. B.13 gives the following expression for $\tilde{j}_z$,

$$\tilde{j}_z = \frac{c^2}{4\pi} \frac{k_\perp^2 k_z}{\omega} (\phi - \psi). \qquad (B.14)$$

Combining Eqs. B.11 and B.14 yields the desired relation for $\psi - \phi$; however, the fluxes $n\vec{\tilde{v}}_{i,e\perp}$ must first be calculated. This is done by considering the perpendicular components of the linearized ion and electron equations of motion.

$$\vec{\tilde{v}}_{i\perp} = \frac{c\vec{E} \times \vec{B}}{B^2} + \frac{m_i c^2}{eB^2} \dot{\vec{E}} \qquad (B.15)$$

$$\vec{\tilde{v}}_{e\perp} = \frac{c\vec{E} \times \vec{B}}{B^2} + \frac{c(\nabla_\perp \tilde{n} T_e) \times \vec{B}}{neB^2} \qquad (B.16)$$

Thus,

$$n\vec{\tilde{v}}_{i\perp} - n\vec{\tilde{v}}_{e\perp} = \frac{i\omega n m_i c^2}{eB^2} \nabla \phi + \frac{c\nabla_\perp (\tilde{n} T_e) \times \vec{B}}{eB^2}, \qquad (B.17)$$

and

$$\nabla_\perp \cdot \left(ne\tilde{v}_{i\perp} - ne\tilde{v}_{e\perp}\right) = -\frac{i\omega nm_i c^2}{B^2}k_\perp^2 \phi. \qquad (B.18)$$

Combining Eqs. B.11, B.14 and B.18,

$$(\psi - \phi) = -\frac{\omega^2}{k_z^2 v_A^2}\phi. \qquad (B.19)$$

Finally, the electron density perturbation can be found by removing $\psi - \phi$ from Eq. B.9.

$$\frac{\tilde{n}_e}{n} = \frac{e\phi}{T_e}\left(1 - \frac{\omega^2}{k_z^2 v_A^2}\left(1 - \frac{\omega^*}{\omega}\right)\right) \qquad (B.20)$$

Equating ion and electron density perturbations, we obtain the dispersion relation,

$$(\omega - \omega^*)\left(1 - \frac{\omega^2}{k_z^2 v_A^2}\right) = \omega k_\perp^2 \rho_s^2. \qquad (B.21)$$

Letting $b = k_\perp^2 \rho_s^2$ and $\omega_A^2 = k_z^2 v_A^2$, the dispersion relation can be rewritten.

$$\omega = \frac{\omega^*}{1+b}\left(1 - \frac{\omega^{*2}}{\omega_A^2}\frac{b}{(1+b)^3}\right) \qquad (B.22)$$

## APPENDIX C

## HETERODYNE DETECTION OF ION ACOUSTIC WAVES

The real and imaginary parts of the ion acoustic wavenumber are given by the following relations (see Chap. 5):

$$k_r = \frac{\omega}{c_s}, \tag{5.1}$$

$$k_i = -k_r \sqrt{\frac{\pi}{8}} \left[ \left( \frac{T_e}{T_i} \right)^{3/2} \exp\left( -\frac{T_e}{T_i} + \sqrt{\frac{m_e}{m_i}} \right) \right], \tag{5.2}$$

where $c_s = \sqrt{\kappa T_e/m_i}$ is the ion sound speed. The ion acoustic waveform was traced out using an interferometer system. Ion waves were excited by means of a flat rectangular tungsten plate (2cm× 1.5cm) and received by a simple, L-shaped tungsten probe. The receiver probe was fixed, while the exciter probe could be translated by means of a computer controlled, stepper motor. The probe position was transduced and fed to to the X input of an X-Y recorder, and the interferometer output was fed to the Y input. The wavelength and damping length of the ion acoustic waves could then be determined from these plots for different plasma conditions. Examples of such plots are shown in Fig. 5.3.

The interferometer system used is shown in Fig. C.1. Heterodyne detection was used to maximize the signal to noise. The R.F. oscillator (WaveTek model 182A) frequency was selected to be 500kHz, since this gave convenient wavelengths of about 1cm. A Mini-Circuits ZDC 10-1 directional coupler was used to split the oscillator output power in the ratio of 10:1. The high-power output was fed to the exciter probe and then to the plasma, while the low-power output was fed to the
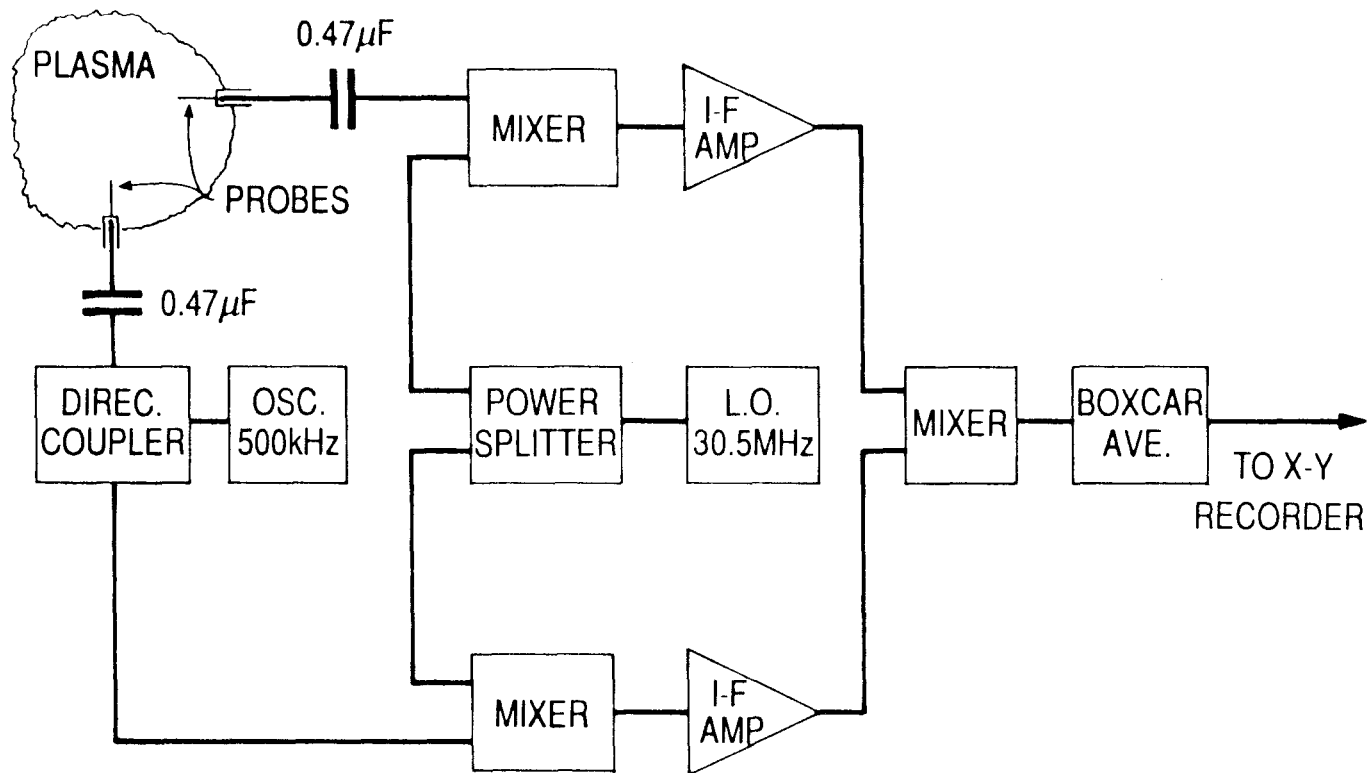
FIG. C.1 Schematic of the heterodyne interferometer used to detect ion acoustic waves in the Encore tokamak.

reference arm of the interferometer. The output of the receiver probe and the low-power output of the directional coupler were mixed with output of the 30.5MHz local oscillator (Tektronix model 191). A Mini-Circuits model ZFSC-2-6 power splitter was used to divide the L.O. output. Mini-Circuits model ZAD 1-1 mixers were used to perform the signal mixing. The mixers yielded "sum" and "difference" signals oscillating at 61MHz and 30MHz, respectively. The mixer outputs were then fed into 30MHz I-F amplifiers (General Radio model 1236). The I-F amplifiers, which are tunable amplifiers, were used to filter off and selectively amplify the difference frequency signal of 30MHz. Finally, the outputs of the I-F amplifiers were mixed to give the interferometer output ($\sim \cos(kx)$) and an oscillatory term of frequency 60MHz. This was finally fed into a Princeton Applied Research model 160 boxcar averager to remove the oscillatory term and to improve the signal-to-noise ratio of the spatially varying term.

# BIBLIOGRAPHY

Anan'ev, Yu. A., "Unstable resonators and their applications (review)," *Sov. J. Quant. Electron.* **1**, 565-586 (1972).

Artsimovich, L. A., "Tokamak devices," *Nucl. Fusion* **12**, 215-252 (1972).

Book, D. L., "NRL Plasma Formulary," unpublished (1983).

Bodin, H. A. B., and Evans, D. E., "Reversed-field pinch research in the United Kingdom," *Nucl. Fusion* **25**, 1305-1311 (1985).

Burakov, V. S., Misyakov, P. Ya., Naumenko, P. A., Nechaev, S. V., Razdobarin, G. T., Semenov, V. V., Sokolova, L. V., and Folomkin, I. P., "Use of the method of resonance fluorescence with a dye laser for plasma diagnostics in the FT-1 tokamak installation," *JETP Lett.* **26**, 403-406 (1977).

Cayton, Thomas E., "Current-driven instabilities in the fluid limit: Parallel kinetic effects in reversed field pinches," *Phys. Fluids* **28**, 598-610 (1985).

Chen, F. F., "Electric probes," in *Plasma Diagnostic Techniques*, R. H. Huddlestone and S. L. Leonard, Eds., (Academic Press, New York, 1965).

Chen, F. F., *Introduction to Plasma Physics* (Plenum Press, New York, 1974).

Cheng, C. Z., and Okuda, H., "Theory and numerical simulations on collisionless drift instabilities in three dimensions," *Nucl. Fusion* **18**, 587-607 (1978).

Chernikov, A. A., Sagdeev, R. Z., Usikov, D. A., Zakharov, M. Yu., and Zaslavsky, G. M., "Minimal chaos and stochastic webs," *Nature* **326**, 559-563 (1987).

Dakin, D. R., Tajima, T., Benford, G., and Rynn, N., "Ion heating by the electrostatic ion cyclotron instability: theory and experiment," *J. Plasma Phys.* **15**, 175-195 (1976).

Dimock, D., Hinnov, E., and Johnson, L. C., "Plasma diagnostics with ionized barium and tunable dye lasers," *Phys. Fluids* **12**, 1730-1732 (1969).

Doveil, F., "Stochastic plasma heating by a large amplitude standing wave," *Phys. Rev. Lett.* **46**, 532-534 (1981).

Drake, J. F., and Lee, T. T., "Irreversibility and transport in the lower hybrid drift instability," *Phys. Fluids* **24**, 1115-1125 (1981).

Fredrickson, E. D., and Bellan, P. M., "Investigation of finite beta modified drift wave in a tokamak plasma," *Phys. Fluids* **28**, 1866-1876 (1985).

Fukuyama, A., Momoto, H., Itantani, R., and Takizuka, T., "Stochastic acceleration by an electrostatic wave near ion cyclotron harmonics," *Phys. Rev. Lett.* **38**, 701-704 (1977).

Furth, H. P., "The tokamak," in *Fusion*, E. Teller, Ed., (Academic Press, New York, 1981).

Gekelman, W., and Stenzel, R. L., "Large, quiescent, magnetized plasma for wave studies," *Rev. Sci. Instrum.*, **46**, 1386-1393 (1975).

Gladd, N. T., and Krall, N. A., "Current-driven drift waves in reversed field pinches," *Phys. Fluids* **29**, 1640-1650 (1986).

Goeckner, M. J., and Goree, J., "Laser-induced fluorescence measurement of plasma ion temperatures: corrections for power saturation," Report 88-13, Department of

Physics and Astronomy, The University of Iowa, Iowa City, Iowa (1988).

Griem, H. R., *Plasma Spectroscopy* (McGraw-Hill, New York, 1964).

Hanna, D. C., *Optics Laser Technol.*, **2**, 122, 175 (1970).

Hatakeyama, R., Oertl, M., Märk, E., and Schrittwieser, R., "Collisionless drift instability and ion heating in a current-carrying inhomogeneous plasma," *Phys. Fluids* **23**, 1774-1781 (1980).

Hecht, E., and Zajac, A., *Optics* (Addison-Wesley, New York, 1974).

Howell, R. B., and Nagayama, Y., "Ion energy measurements on a reversed-field pinch experiment using Doppler broadening," *Phys. Fluids* **28**, 743-748 (1985).

Hsu, J. Y., "Frequency mismatch and stochastic heating in the cyclotron frequency range," *Phys. Fluids* **25**, 159-163 (1982).

Kadomtsev, B. B., *Plasma Turbulence* (Academic Press, London, New York, 1965).

Karney, C. F. F., "Stochastic ion heating by a lower hybrid wave," *Phys. Fluids* **21**, 1584-1599 (1978).

Koslover, R., and McWilliams, R., "Measurement of multidimensional ion velocity distribution functions by optical tomography," *Rev. Sci. Instrum.*, **57**, 2421-2448 (1986).

Lichtenberg, A. J., and Lieberman, M. A., *Regular and Stochastic Motion* (Springer-Verlag, New York, 1983).

Lotz, W., "Electron -impact ionization cross-sections and ionization rate coefficients for atoms and ions from hydrogen to calcium," *Z. Physik* **216**, 241-247 (1968).

128

McWhirter, R. W. P., "Spectral Intensities," in *Plasma Diagnostic Techniques*, R. H. Huddlestone and S. L. Leonard, Eds. (Academic Press, New York, 1965).

Mah, S. Q., et al., "Current-induced ion heating in a toroidal plasma," *Phys. Rev. Lett.* **25**, 1409-1413 (1970).

Measures, R. M., "Selective excitation spectroscopy and some possible applications," *J. Appl. Phys.* **39**, 5232-5245 (1968).

Mikhailovskii, A. B. and Rudakov, L. I., "The stability of a spatially inhomogeneous plasma in a magnetic field," *JETP* **17**, 621-625 (1963).

Mitchell, A. C. G. and M. W. Zemansky, *Resonance Radiation and Excited Atoms* (MacMillan, London, 1934).

Mondt, J. P. and Goedert J., "Dissipative instabilities at the edge of reversed-field pinches driven by a combination of plasma gradients and a parallel current," *Phys. Fluids* **28**, 1816-1825 (1985).

Moore, C. A., Davis, G. P., and Gottscho R. A., "Sensitive, nonintrusive *in-situ* measurement of temporally and spatially resolved plasma elecric fields," *Phys. Rev. Lett.* **52**, 538-541 (1984).

Müller, A., Salzborn, E., Frodl, R., Becker, R., Klein, H., and Winter, H., "Absolute ionization cross sections for electrons incident on $O^+$, $Ne^+$, $Xe^+$ and $Ar^{i+}$ ($i$=1,....,5)," *J. Phys. B: Atom. Molec. Phys.* **13**, 1877-1899 (1980).

Muller III, C. H. and Burrell K. H., "Time-dependent measurements of metal impurity densities in a tokamak discharge by use of laser-induced fluorescence," *Phys. Rev. Lett.* **47**, 330-333 (1981).

Ortolani, S., "Reversed-field pinch research at Padua," *Nucl. Fusion* **25**, 1291-1294 (1985).

Robinson, D. C., and Rusbridge, M. G., "Structure of turbulence in the Zeta plasma," *Phys. Fluids* **14**, 2499-2511 (1971).

Skiff, F., Anderegg, F., and Tran, M. Q., "Stochastic particle acceleration in an electrostatic wave," *Phys. Rev. Lett.* **58**, 1430-1433 (1987).

Smith, Gary R., and Kaufman, Allan N., "Stochastic acceleration by a single wave in a magnetic field," *Phys. Rev. Lett.* **34**, 1613-1616 (1975).

Stern, R. A., and Johnson III, J. A., Plasma ion diagnostics using resonant fluorescence," *Phys. Rev. Lett.* **34**, 1548-1551 (1975).

Stern, R. A., Correll, D. L., Böhmer H., and Rynn, N., "Nonlocal effects in the electrostatic ion-cyclotron instability," *Phys. Rev. Lett.* **37**, 833-836 (1976).

Stern, R. A., Hill, D. N., and Rynn, N., "Direct ion transport measurement by optical tagging," *Phys. Lett.* **93A**, 127-130 (1983).

Summers, H. P., and McWhirter, R. W. P., "Radiative power loss from laboratory and atrophysical plasmas I. Power loss from plasmas in steady-state ionization balance," *J. Phys. B: Atom. Mol. Phys.* **12**, 2387-2412 (1979).

Tang, J. T., and Luhmann Jr., N. C., "Destabilization of hydromagnetic drift-Alfvén waves in a finite pressure, collisional plasma," *Phys. Fluids* **19**, 1935-1946 (1976).

Trubnikov, B. A., "Particle interactions in a fully ionized plasma," *Rev. Plasma Phys.* **1**, 105-204 (1965).

West, W. P., Thomas, D. M., Ensberg, E. S., DeGrassie, J. S., and Baur, J. F., "Diagnostic instrument for the measurement of poloidal magnetic fields in tokamaks," *Rev. Sci. Instrum.*, **57**, 1552-1556 (1986).

Wiese, W. L., Smith, M. W., Miles, B. M., *Atomic Transition Probabilities, Vol. II* (U. S. Government Printing Office, Washington D. C., 1969).

Yariv, A., *Quantum Electronics* (John Wiley & Sons, New York, 1975).